Developing and Testing a Novel De-centralized Cycle-free Game Theoretic Traffic Signal Controller: A Traffic Efficiency and Environmental Perspective

Hossam M. Abdelghaffar

Dissertation submitted to the Faculty of the
Virginia Polytechnic Institute and State University
in partial fulfillment of the requirements for the degree of

Doctor of Philosophy
in
Electrical Engineering

Hesham A. Rakha, Chair
Craig A. Woolsey
Hao Yang
Amos L. Abbott
Haibo Zeng

April 25, 2018
Blacksburg, Virginia

Keywords: Aerosol detection, source localization, traffic signal controller, game theory

Developing and Testing a Novel De-centralized Cycle-free Game Theoretic Traffic Signal Controller: A Traffic Efficiency and Environmental Perspective

Hossam M. Abdelghaffar

(ABSTRACT)

Traffic congestion negatively affects traveler mobility and air quality. Stop and go vehicular movements associated with traffic jams typically result in higher fuel consumption levels compared to cruising at a constant speed. The first objective in the dissertation is to investigate the spatial relationship between air quality and traffic flow patterns. We developed and applied a recursive Bayesian estimation algorithm to estimate the source location (associated with traffic jam) of an airborne contaminant (aerosol) in a simulation environment. This algorithm was compared to the gradient descent algorithm and an extended Kalman filter algorithm. Results suggest that Bayesian estimation is less sensitive to the choice of the initial state and to the plume dispersion model. Consequently, Bayesian estimation was implemented to identify the location (correlated with traffic flows) of the aerosol (soot) that can be attributed to traffic in the vicinity of the Old Dominion University campus, using data collected from a remote sensing system. Results show that the source location of soot pollution is located at congested intersections, which demonstrate that air quality is correlated with traffic flows and congestion caused by signalized intersections.

Sustainable mobility can help reduce traffic congestion and vehicle emissions, and thus, optimizing the performance of available infrastructure via advanced traffic signal controllers has become increasingly appealing. The second objective in the dissertation is to develop a novel de-centralized traffic signal controller, achieved using a Nash bargaining game-theoretic framework, that operates a flexible phasing sequence and free cycle length to adapt to dynamic changes in traffic demand levels.

The developed controller was implemented and tested in the INTEGRATION microscopic traffic assignment and simulation software. The proposed controller was compared to the

operation of an optimum fixed-time coordinated plan, an actuated controller, a centralized adaptive phase split controller, a decentralized phase split and cycle length controller, and a fully coordinated adaptive phase split, cycle length, and offset optimization controller to evaluate its performance.

Testing was initially conducted on an isolated intersection, showing a 77% reduction in queue length, a 17% reduction in vehicle emission levels, and a 64% reduction in total delay. In addition, the developed controller was tested on an arterial network producing statistically significant reductions in total delay ranging between 36% and 67% and vehicle emissions reductions ranging between 6% and 13%. Analysis of variance, Tukey, and pairwise comparison tests were conducted to establish the significance of the proposed controller. Moreover, the controller was tested on a network of 38 intersections producing significant reduction in the travel time by 23.6%, a reduction in the queue length by 37.6%, and a reduction in CO_2 emissions by 10.4%. Finally, the controller was tested on the Los Angeles downtown network composed of 457 signalized intersections, producing a 35.1% reduction in travel time, a 54.7% reduction in queue length, and a 10% reduction in the CO_2 emissions.

The results demonstrate that the proposed decentralized controller produces major improvements over other state-of-the-art centralized and de-centralized controllers.

Developing and Testing a Novel De-centralized Cycle-free Game Theoretic Traffic Signal Controller: A Traffic Efficiency and Environmental Perspective

Hossam M. Abdelghaffar

(GENERAL AUDIENCE ABSTRACT)

Traffic congestion affects traveler mobility and also has an impact on air quality, and consequently, on public health. Stop-and-go driving, which is typically associated with traffic jams, results in increased fuel consumption when compared to cruising at a constant speed. This in turn contributes to the amount of vehicle emissions that create air pollution, which contributes to global warming. Consequently, studying the spatial relationships between air quality and traffic flow patterns is directly related to enhancing air quality, as improving these patterns can reduce traffic congestion.

The first objective in this dissertation is to investigate the spatial relationship between air quality and traffic flow patterns. We developed and applied a recursive Bayesian estimation algorithm to estimate the source location of an airborne contaminant (aerosol) in a simulation environment. This algorithm was compared to the gradient descent algorithm and the extended Kalman filter. Results suggest that Bayesian estimation is less sensitive to the choice of the initial state and to the plume dispersion model when compared to the other two approaches. Consequently, an experimental investigation using Bayesian estimation was conducted to identify the location (correlated with traffic flows) of the aerosol (soot) that can be attributed to traffic in the vicinity of the Old Dominion University campus, using data collected from a remote sensing system (a compact light detection and ranging [LiDAR] system). The results show that the location of soot pollution in the study area is located at congested intersections, which demonstrates that air quality is correlated with traffic flows and congestion caused by signalized intersections.

Sustainable mobility could enhance air quality and alleviate congestion. Accordingly, optimizing the utilization of the available infrastructure using advanced traffic signal controllers

has become necessary to mitigate traffic congestion in a world with growing pressure on financial and physical resources. The second objective in the dissertation is to develop a novel de-centralized traffic signal controller that is achieved using a Nash bargaining game-theoretic framework. This framework has a flexible phasing sequence and free cycle length, and thus can adapt to dynamic changes in traffic demand. The controller was implemented and evaluated using the INTEGRATION microscopic traffic assignment and simulation software.

The proposed controller was tested and compared to state-of-the-art isolated and coordinated traffic signal controllers. The proposed controller was tested on an isolated intersection, producing a reduction in the queue length ranging from 58% to 77%, and a reduction in vehicle emission levels ranging from 6% to 17%. In the case of the arterial testing, the controller was compared to an optimum fixed-time coordinated plan, an actuated controller, a centralized adaptive phase split controller, a decentralized phase split and cycle length controller, and a fully coordinated adaptive phase split, cycle length, and offset optimization controller to evaluate its performance. On the arterial network, the proposed controller produced reductions in the total delay ranging from 36% to 67%, and a reduction in vehicle emissions ranging from 6% to 13%. Statistical tests show that the proposed controller produces major improvements over other state-of-the-art centralized and de-centralized controllers.

In the domain of large scale networks, simulations were conducted on the town of Blacksburg, Virginia composed of 38 signalized intersections. The results show significant reductions on the intersection approaches with travel time savings of 23.6%, a reduction in the average queue length of 37.6%, a reduction in the average number of vehicle stops of 23.6%, a reduction in CO_2 emissions of 10.4%, a reduction in the fuel consumption of 9.8%, and a reduction in NO_X emissions of 5.4%.

In addition, the proposed controller was tested on downtown Los Angles, California, including the most congested downtown area, which has 457 signalized intersections, and compared to the performance of a decentralized phase split and cycle length controller. The results

show significant reductions on the intersections links in the average travel time of 35.1%, a reduction in the average queue length of 54.7%, a reduction in the average number of stops of 44%, a reduction in CO_2 emissions of 10%, a reduction in the fuel consumption of 10%, and a reduction in NO_X emissions of 11.7%.

Furthermore, simulations were conducted at lower traffic flow levels and showed significant reductions on the network performance producing reductions in vehicle average total delay of 36.7%, a reduction in the stopped delay by 90.2%, and a reduction in the average number of stops by 35%, over a decentralized phase split and cycle length controller.

The results demonstrate that the proposed decentralized controller reduces traffic congestion, fuel consumption and vehicle emission levels, and produces major improvements over other state-of-the-art centralized and de-centralized controllers.

Acknowledgments

First of all, I sincerely thank God, the most Gracious, most Merciful, Thee do we worship, and Thine aid we seek, for enabling me to finish my PhD dissertation.

I would like to express my deepest gratitude to my adviser Prof. Hesham Rakha. This dissertation was completed thanks to his rich technical support, inspiration, guidance, fruitful discussions, continuous encouragement, and support. His continuous support and high expectations drove me to challenge myself to do better throughout my journey.

I would like to thank the committee for their effort. I would also like to express my gratefulness to Prof. Craig Woolsey for his tremendous help and guidance; I have really learned a lot from him. Also, I am grateful to Prof. Hao Yang for his help and cooperation and to Prof. Amos Abbott and Prof. Haibo Zeng for their continuous valuable suggestions and recommendations. Thank you all for spending your valuable time on this dissertation.

In addition, my heartfelt thanks to my beloved parents for their encouragement. Special thanks go to my wife Nesreen for her continuous support. I don't know how I would have progressed without her. And thanks to my lovely children. God bless you all.

I would also like to thank my colleagues in the Center for Sustainable Mobility and Nonlinear Systems Laboratory for their support. Thanks to Prof. Sedki Riad and Prof. Hesham Arafat for their support and sincere advices. Finally, thanks to the Cultural Affairs and Mission Sector (Egyptian Ministry of Higher Education) for supporting me with a scholarship during my first two years.

Contents

List of Figures xiii

List of Tables xvii

1 Introduction 1

1.1 Problem Statement 1

1.2 Research Objective 5

1.3 Methodology 6

1.4 Contribution 9

1.5 Dissertation Roadmap 13

2 Literature Review 15

2.1 Background 15

2.2 Related Work 19

2.2.1 Fixed-time plan 19

2.2.2 Actuated Control 20

2.2.3 Adaptive Controllers 20

2.2.3.1 State-of the-Practice: . . . 21
2.2.3.2 State-of the-art: . . . 23
2.3 Summary . . . 30

3 Source Localization **32**

3.1 Introduction . . . 32
3.2 Contaminant Simulation . . . 36
3.2.1 Wind Field . . . 36
3.2.2 Contaminant Plume Model . . . 37
3.3 Estimation Algorithms . . . 38
3.3.1 Bayesian Estimation Algorithm . . . 39
3.3.2 Gradient Descent Algorithm . . . 42
3.3.3 Extended Kalman Filter Algorithm . . . 44
3.4 Simulation Results . . . 46
3.4.1 Bayesian Estimation Simulation Results . . . 46
3.4.2 Gradient Descent Simulation Results . . . 49
3.4.3 Extended Kalman Filter Simulation Results . . . 52
3.5 Aerosol Localization: Field Experiment 1 . . . 55
3.5.1 Experimental Setup . . . 55
3.5.2 Experimental Results . . . 57
3.5.2.1 LR Measurements . . . 57
3.5.2.2 BCR Measurements . . . 57

3.5.2.3 Estimation Results 60
3.6 Aerosol Localization: Field Experiment 2 62
3.6.1 Experimental Setup 62
3.6.2 Experimental Results 63
3.6.2.1 LR Measurements 64
3.6.2.2 BCR Measurements 66
3.6.2.3 Estimation Results 68
3.7 Summary 70

4 Proposed Traffic Signal Controller **73**

4.1 Traffic Signal Controller using game-theoretic framework 74
4.1.1 NB Solution for Two Players Considering a Cooperative Game . . . 74
4.1.2 Traffic Signal NB Solution for Multi-players 79
4.1.3 Convexity of the Utility Space 82
4.2 Experimental Results: Isolated Intersection 87
4.2.1 Testbed Intersection 87
4.2.2 Demand Modeling 87
4.2.3 Phasing Scheme 88
4.2.4 Experimental Setup 88
4.2.4.1 Traffic Simulation Models 88
4.2.4.2 Measures of Effectiveness (MOEs) 89
4.2.4.3 Simulation Parameters 90

4.2.5 Experimental Results . . . 90
4.2.5.1 Original Demand (O-D) . . . 90
4.2.5.2 Lower And Higher Demand . . . 94
4.3 Summary . . . 95

5 Experimental Results: Arterial Network 98

5.1 De-Centralized NB controller for Multi-intersections . . . 99
5.2 Experimental results: Arterial Network . . . 101
5.2.1 Testbed Arterial Network . . . 101
5.2.2 Demand Modeling . . . 101
5.2.3 Phasing Scheme . . . 103
5.2.4 Experimental Setup . . . 104
5.2.4.1 Benchmarks . . . 104
5.2.4.2 Simulation Parameters . . . 104
5.2.5 Experimental Results . . . 105
5.3 Statistical Analysis . . . 108
5.4 Summary . . . 109

6 Experimental Results: Large Scale Networks 111

6.1 Blacksburg Town Experiments . . . 112
6.1.1 Blacksburg Experimental Setup . . . 112
6.1.2 BB Experimental Results: 1 . . . 113

6.1.3 BB Experimental Results: 2 114
6.1.4 BB Experimental Results: 3 115
6.2 Downtown Los Angles Experiments 119
6.2.1 Los Angles Experimental Setup 119
6.2.2 LA Experimental Results: 1 120
6.2.3 LA Experimental Results: 2 122
6.3 Summary 123

7 Summary, Conclusions, and Future Research **125**
7.1 Summary & Conclusions 125
7.2 Recommendations For Future Research 131

Bibliography **132**

List of Figures

1.1 Research methodology 9

3.1 Three-dimensional filament locations and 5-min time-averaged concentration (in particles/cm^3) at a 40 m altitude. 39

3.2 Flow chart for implementing the three estimation algorithms. 41

3.3 Coordinate system used to present the plume (Adapted from [1]). 43

3.4 Estimation results using 40m x 40m grid cells. 47

3.5 Probability distribution after the first detection. 48

3.6 Probability distribution after the fifth detection. 48

3.7 Final probability distribution. 48

3.8 Estimation results using 70m x 70m grid cells. 49

3.9 Sampling path. 50

3.10 Result of off-line GD estimation of the contaminant source location. 50

3.11 True and estimated contaminant concentration (in particles/m^3) at 40 m altitude. 51

3.12 Off-line result of estimating the contaminant source location using the GD method. 52
3.13 On-line result of estimating the contaminant source location using EKF. . . 53
3.14 Contaminant plume distribution at 40 m altitude. 53
3.15 On-line result of estimating the contaminant source location using EKF. . . 54
3.16 Lidar in vision lab at Old Dominion University. 56
3.17 Measurements locations, Google maps. 56
3.18 Soot locations based on LR values. 58
3.19 Normalized frequency of detection for soot. 58
3.20 LR soot concentration. 59
3.21 Soot locations based on BCR values. 59
3.22 Normalized frequency of detection for soot. 60
3.23 BCR soot concentration. 60
3.24 Estimation results. 61
3.25 Probability distribution after the first detection. 62
3.26 Final Probability distribution. 62
3.27 Measurements Locations, Google maps. 63
3.28 Lidar ratios of expected particular matters of interest (soot). 64
3.29 LR Normalized frequency measurements of soot. 65
3.30 LR soot concentration. 65
3.31 Color ratios of expected particular matters of interest (Soot). 66
3.32 BCR Normalized frequency measurements of soot. 67

3.33 Interpolated BCR soot concentration. 67

3.34 Estimation results. 69

3.35 Intersections Locations, Google maps. 69

3.36 Final Probability distribution. 70

4.1 Utility region. 75

4.2 Phasing scheme. 80

4.3 NB controller block diagram. 82

4.4 Traffic signal delay for under-saturated traffic conditions. 83

4.5 Traffic signal delay for an over-saturated traffic conditions. 85

4.6 Roadmap for implementing the developed NB controller 86

4.7 Testbed Intersection. 87

4.8 Phasing scheme. 88

4.9 Average queue length. 92

4.10 Measure of effectiveness. 93

4.11 Measure of effectiveness vs. flow ratio. 96

4.12 Average queue length vs. flow ratio. 96

5.1 Blacksburg testbed arterial network. 102

5.2 Phasing scheme. 103

5.3 Average MOEs of 30 simulations at random seeds. 106

5.4 Average queue length of the intersections. 107

5.5 Assumptions of ANOVA test. 108

6.1 Blacksburg network. 112

6.2 Four phasing scheme. 114

6.3 Sensitivity analysis. 116

6.4 Downtown Los Angles, Google maps. 119

6.5 INTEGRATION, Los Angles network. 120

6.6 LA Sensitivity Analysis. 121

List of Tables

4.1 Two players matrix game 75

4.2 Origin Destination Demand Matrix 88

4.3 Overall Intersection Performance Measure For Different Control Systems . . 91

4.4 Intersection Performance Measure For Different Control Systems at Different Demand Profiles 94

5.1 Multi-players matrix game 99

5.2 All possible Network Actions (Permutations) 100

5.3 Average MOEs and the percent improvement using NB controller over other controllers 107

5.4 Analysis of Variance 108

5.5 Tukey Test 109

5.6 Pair Wise Comparison 109

6.1 Average MOEs and (%) improvement using NB over PSC and PSCO controllers 114

6.2 MOEs using two different phasing schemes 115

6.3 Average MOEs and (%) improvement using NB over PSC & PSCO controllers 117

6.4 Intersections (%) improvement of MOEs using NB over PSC controller . . . 118

6.5 Average MOEs and the (%) improvement using NB controller over PSC controller (100% Demand) 121

6.6 Average (%) improvements of MOEs using NB controller over PSC controller (100% Demand), over the links that are directly associated with intersections 122

6.7 Average MOEs and the (%) improvement using NB over PSC controller (0.1% Demand) 122

6.8 Average (%) improvements of MOEs using NB over PSC controller (0.1% Demand) over the links directly associated with intersections 123

Chapter 1

Introduction

1.1 Problem Statement

Traffic growth constrained by available capacity in urban areas affects traveler mobility, air quality, and public health. Reducing traffic congestion can improve these conditions while simultaneously decreasing transportation-related energy use. Traffic congestion in 2013 cost Americans $124.2 billion in direct and indirect losses. This number will rise to $186.2 billion in 2030 [2], which is a 50% increase in the cost of congestion. In 2013, $78 billion in losses resulted from time and fuel wasted in traffic (direct costs) and $45 billion was the sum of indirect costs. The estimated annual cost of traffic in the U.S. and Europe will soar to $293 billion by 2030, a rise of nearly 50% from 2013.

Stop-and-go vehicular movement associated with traffic jams typically results in higher fuel consumption rates compared to cruising at a constant speed. This in turn contributes to the amount of vehicle emissions that create air pollution and contributes to global warming. Consequently, studying the spatial relationships between air quality and traffic flow patterns as the potential enhance the air quality by reducing traffic congestion.

To investigate the spatial relationship between air quality and traffic flow patterns, a strat-

egy for identifying the source location (typically associated with traffic jam location) was formulated; this strategy simulates a turbulent atmospheric flow, models the concentration of a contaminant (vehicle emissions) released into that flow, and finally estimates the source location of the contaminant.

The source localization problem is especially difficult in a turbulent flow environment, such as the planetary boundary layer. In a turbulent wind, plume effluent spreads in a random motion, meandering to create patches of high and low concentrations.

The plume width and the concentration within the plume do not vary predictably in time and space. The uncertain relationship between the location of detection and the actual location of the source in a turbulent flow makes source localization challenging. Various algorithms have been proposed for the source localization problem, including gradient ascent, biologically inspired algorithms, and probabilistic algorithms. Gradient ascent is an iterative optimization technique [3], that is capable of finding a local optimum within some scalar field (e.g., the maximum concentration); however, the algorithm is not guaranteed to find a global optimum. Biologically inspired source localization algorithms emulate the behavior of creatures, which solve similar problems [4]. The simple, biomimetic decision strategy of moving upwind with every positive detection and moving across-wind with every non-detection can be quite effective, especially in a completely random environment; the approach relies only on instantaneous measurements, ignoring all of the prior information that has been collected. Probabilistic algorithms can be considered a compromise between the gradient ascent approach and the biomimetic approach described above, where one constructs a probabilistic estimate of the concentration field (perhaps a time- and space-averaged estimate) enabling one to assess the likelihood that a given point is the source location [5].

Sustainable mobility can help reduce traffic congestion and vehicle emissions. Accordingly, optimizing the utilization of the available infrastructure using advanced traffic signal controllers has become increasingly necessary to mitigate traffic congestion in a world with growing pressure on financial and physical resources. A signalized intersection is designed

(controlled) to allow traffic flow to proceed efficiently and safely by separating conflicting movements in time rather than in space. Traffic signal control controllers attempt to minimize various traffic parameters (e.g., delay, queue length, and energy and emission levels) by optimizing traffic signal control variables that include the cycle length, phase scheme and sequence, phase split and offset. Consequently, traffic signal optimization algorithms attempt to identify the optimal values of one or more traffic signal control variables for specific traffic conditions. Most of the currently implemented traffic signal systems can be categorized into one of the following categories: fixed-time plan (FP), actuated (ACT), responsive, or adaptive [6].

An FP is developed off-line using historical traffic data to compute traffic signal timings; real-time traffic data is not considered. Thereafter, the order and duration of all phases remain fixed and do not adapt to fluctuations in traffic demand. As a result, FPs are known to age with time; they are suitable for relatively stable and regular traffic flows. However, given that traffic is dynamic, one particular predefined traffic signal plan cannot efficiently fit all real-time traffic conditions [7]. What is really needed is dynamic data so that the traffic signals can change dynamically in terms of intervals to better move traffic around a network. In other words, instead of relying on what has happened in the past, it is possible to dynamically change the traffic environment using data collected in real-time. Examples of software that compute fixed-time signal timing include TRANSYT-7F and PASSER. TRANSYT-7F is a macroscopic deterministic optimization and simulation model that considers platoons of vehicles instead of individual vehicles. The model attempts to minimize a disutility index based on delay, stops, and queue lengths [8]. This approach has been found to only be appropriate for under-saturated conditions [9]. PASSER is an arterial-based, bandwidth optimizer (i.e., it maximizes the green band to move the anticipated platoon of vehicles through the arterial signal system without stopping) that computes phase sequences, cycle lengths, and offsets for a maximum of 20 intersections in a single run [9]. PASSER works within a given cycle length and split to find offsets that maximize an arterial green band.

Actuated traffic signal controls, on the other hand, respond to changes in traffic demand

patterns using local actuations. This type of control requires that vehicle detectors be installed at intersection approach stop lines. The actuated timing plan responds to traffic demand by placing a call to the controller based on the presence or absence of vehicles approaching or leaving the intersection, respectively. Once a call is received, the controller decides whether to extend or terminate the green phase in response to the actuation source. Note, however, that while actuated signal control was proven to perform better than fixed-time traffic signal control, in most cases, actuated traffic signal control does not offer any real-time optimization to properly adapt to traffic fluctuations. Consequently, actuated signal control is less sensitive to the traffic demand (i.e., number of vehicles) calling for the actuation and might result in very long queues in grid-like networks [10].

Adaptive systems use detector inputs, historical trends, and predictive models to predict traffic arrivals at intersections. Using these predictions, they determine the best gradual changes in cycle length, splits, and offsets to optimize an objective function, such as minimizing the delay or the queue length, for intersections within a predetermined sub-area of a network [11]. Examples in this category are the SCOOT and SCATS systems. The SCOOT system minimizes a performance index that is a function of delay and number of vehicle stops at all approaches in the network [12]. SCOOT performs effectively in under-saturated traffic conditions, and it is a macroscopic model that does not capture microscopic behavior such as gap acceptance and lane changing behavior. SCATS monitors the traffic flows and headways at the stop bars [13], based on the volumes and headways gathered in one-minute intervals; as a result, green times (splits) are reallocated to the phases of greatest need. Other examples of adaptive systems are RHODES [14] and OPAC [15], which optimize an objective function for a specified rolling horizon (using traffic prediction models) and have pre-defined sub-areas (limited flexibility) in which the signals can be coordinated. RHODES and OPAC are based on dynamic programming that require a state transition probability model for the traffic environment, which is difficult to obtain.

One of the main disadvantages of actuated and adaptive traffic control approaches is that their operation is constrained by maximum and minimum values for cycle lengths, splits, and

offsets. They also have to go through a pre-defined sequence of phases. In addition, some of today's most sophisticated traffic control systems use hierarchies that either partially or completely centralize the decisions, making the systems more vulnerable to failures in one of the master controllers. In such events, the entire area of influence of the master traffic signal, which may include several intersections, will be compromised by a single failure. Hierarchies also make systems more difficult to scale up, as centralized computers will need to interconnect all intersections within pre-defined subareas, creating limitations and requirements as the network is expanded [16]. Traffic flow is highly dependent on factors such as time-of-day, day-of-the-week, weather, and unpredictable events such as incidents, special events, work zones, etc. Consequently, improvements to traffic control strategies could be made if the control system is able to not only respond to the actual conditions found in the field, but also to adapt their actions to transient conditions.

1.2 Research Objective

The objective of this research is to:

- Investigate the spatial relationship between air quality and traffic flow patterns, by developing a source localization algorithm that is capable of identifying the source location (traffic jam location), using real field measurements (soot) collected in an urban environment.
- Develop a novel adaptive traffic signal controller with the following features to reduce traffic congestion and vehicle emissions by addressing the limitations of existing state-of-the practice and state-of-the-art adaptive traffic signal controllers:
  - Has the ability to adapt the signal timing based on observed traffic state without using historical data.
  - Is decentralized, which will increase both the scalability and robustness of the

system, and control a large urban traffic network through a number of control agents to avoid the issue of a single point failure in the centralized systems.

- Is model free − doesn't need an explicit model of the environment.
- Has a free cycle length with flexible phasing sequence.
- Is designed and evaluated on traffic scenarios that closely represent those found in the real-world, which will ensure that the algorithm is not only capable of solving simple traffic problems, but is also applicable to real situations.

1.3 Methodology

To investigate the spatial relationship between air quality and traffic flow patterns, a source localization strategy to identify the source location (correlated with traffic flow) of an airborne contaminant (soot) in a turbulent wind field was developed. Simulation studies were conducted to demonstrate relative strengths and weaknesses of source localization strategies. These simulations were preliminary steps toward the planned experiment.

In simulations, the turbulent wind field was generated using a stochastic, full-field turbulent wind simulator called TurbSim [17]. TurbSim generates a time series of three-component wind vectors at points in a two-dimensional vertical rectangular grid. Subsequently, the advection/diffusion model of Farrell et al. [18] was used to generate a time-evolving concentration field using the flow velocity generated by TurbSim. Once the plume matured, we froze the scalar field and implemented three source localization strategies; a recursive Bayesian estimation, a gradient descent algorithm, and an extended Kalman filter. The simulation results showed that estimating the source location using the Bayesian estimation algorithm requires minimal model assumptions, and demonstrated that the Bayesian estimation algorithm is an effective strategy for estimating the source location.

Subsequently, an experimental investigation based on real flow conditions was conducted to estimate the source location of the aerosol (soot), that can be attributed to traffic, using a

Bayesian estimation algorithm. In the experiment, a light detection and ranging (LiDAR) system was deployed to measure aerosol vertical profiles. This system offers a measurement for every 30 meters vertically from ground level to 12km, to create a profile, or distribution of aerosols. Measurements were collected over an urban city at different locations, to analyze the distribution of aerosols (pollution levels) with variations in traffic levels, which then allowed investigation of the spatial relationships between air quality and traffic flow patterns. The results show that the source of the soot over the area of study was located at intersections, where diesel trucks most likely stop frequently.

To enhance the air quality, optimizing the utilization of the available infrastructure using advanced traffic signal controllers is necessary to mitigate traffic congestion and emissions. Due to the stochastic nature of the traffic flows, an adaptive control strategy that can adapt to the stochastic fluctuations in the traffic flow is needed. Cycle-free strategies could offer a new, less restrictive perspective to accommodate changes in traffic conditions. Game theory is considered a suitable approach that has the potential to adapt to traffic fluctuations and randomness of traffic systems, and therefore alleviate traffic congestion more effectively than the more commonly used FP and ACT systems [19].

Game theory studies the interactive cooperation between intelligent rational decision makers, and has been widely used in economic, military, and communication applications. Game theory has also been applied to model traveler route choice behavior [20], control connected vehicle movements [21], and in route guidance [22]. Bargaining theory is related to cooperative games through the concept of Nash bargaining (NB). A bargaining situation is defined as a situation in which multiple players with specific objectives cooperate and benefit by reaching a mutually agreeable outcome. The bargaining process is the procedure that bargainers follow to reach an agreement (outcome), and the bargaining outcome is the result of the bargaining process [23], [24]. The NB solution has been applied in a number of applications, including multimedia resource management [25], allocating multi-user channels to networks [26], a wireless cooperative relaying network [27], investment, wages and employment [28], [29], and for downlink beamforming in an interference channel [30].

To mitigate traffic congestion at signalized intersections, we developed a novel de-centralized traffic signal optimization controller considering a flexible phasing sequence and free cycle length using a NB game-theoretic framework. While it is desirable to compare the developed NB controller to the state-of-the-practice systems, it is difficult to identify a benchmark with available operational details due to intellectual property restrictions given that the algorithmic details are proprietary. However, it is possible to compare the performance of the NB approach to the operation of an optimum fixed-time coordinated plan (FP), actuated (ACT) controller, a centralized adaptive phase split controller (PS), a decentralized phase split and cycle length controller (PSC) [10], and a fully coordinated adaptive phase split-cycle length and offset optimization controller (PSCO) [31],[32] to evaluate the performance of the proposed decentralized controller.

To evaluate the performance of the NB approach, each of the following was calculated per movement for a signalized intersection: average travel time, average stopped delay, average queue length, average vehicle speed, average vehicle throughput, average fuel consumption and average emission levels. The proposed approach was implemented and evaluated in the INTEGRATION microscopic traffic assignment and simulation software [33, 34]. Then, the proposed approach was compared to an FP and ACT controllers to evaluate its performance at different traffic demand levels. In addition, the NB approach was implemented and evaluated on an arterial network, with six intersections, and was compared to an FP, PS, PSC, PSCO controllers to evaluate its performance. Analysis of Variance (ANOVA), Tukey, and pairwise comparison tests were conducted to examine the statistically significant difference of the proposed controller. Moreover, the proposed approach was implemented and evaluated on large scale networks with 38 and 457 intersections. The research methodology is shown in Figure 1.1.

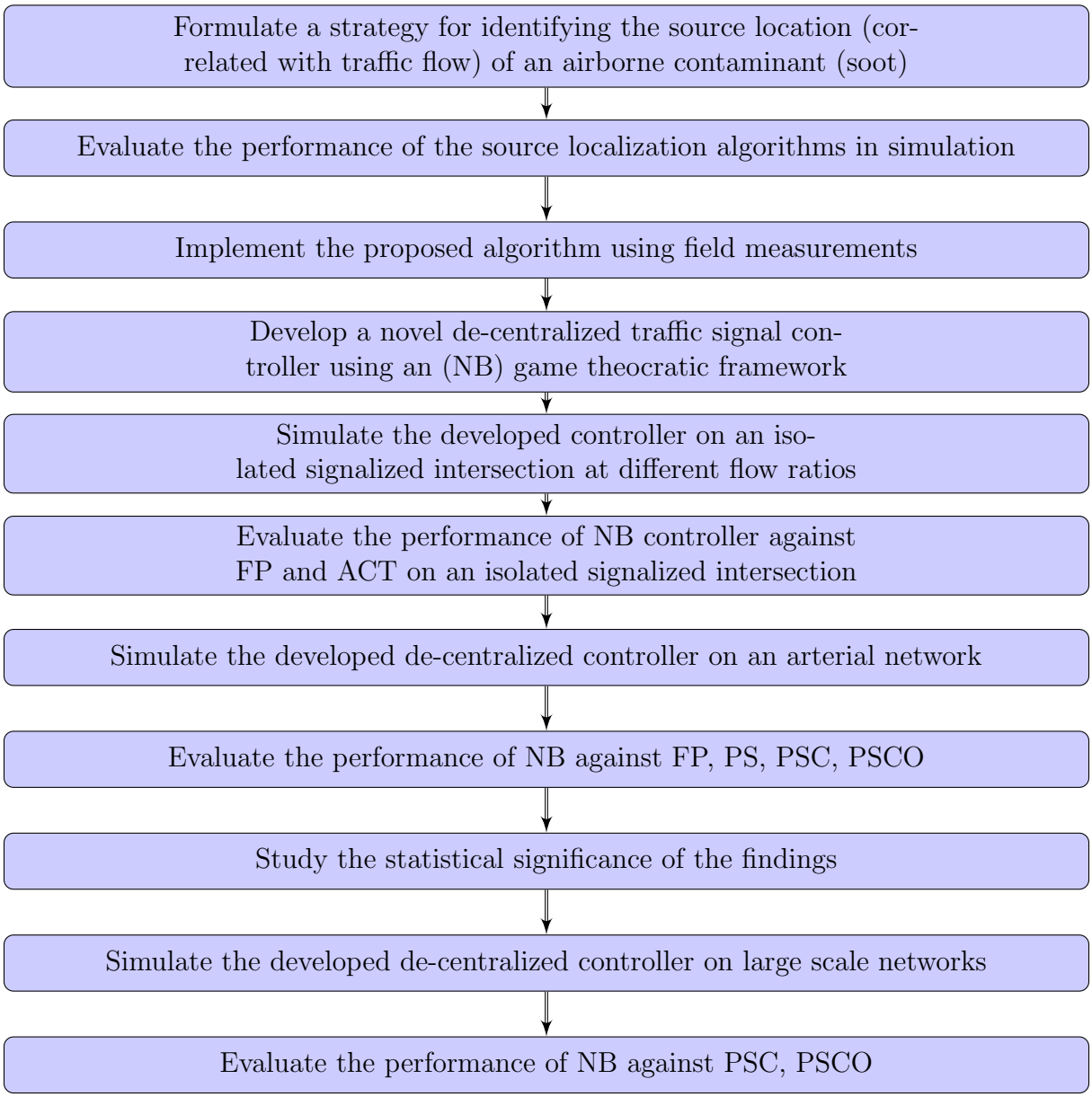

Figure 1.1: Research methodology

1.4 Contribution

A source localization strategy to identify the source location (correlated with traffic flow) of an airborne contaminant (soot) in a turbulent wind field was developed. First, the problem was formulated and addressed in a simulation environment, using three estimation al-

gorithms: a recursive Bayesian estimation algorithm, a gradient descent algorithm, and an extended Kalman filter algorithm to demonstrate relative strengths and weaknesses of source localization strategies. The simulation results show that estimating the source location using the Bayesian estimation algorithm requires minimal modeling assumptions. Moreover, the source strength and the wind statistics were not needed for this algorithm. In contrast, the estimation results using the gradient descent algorithm or the extended Kalman filter were affected by the choice of the initial conditions and by the contaminant plume dispersion model. Simulation results suggest that the Bayesian estimation algorithm is an effective strategy for estimating the source location.

Subsequently, field experiments based on real flow conditions were conducted to identify the possible source location of the aerosol (soot), that can be attributed to traffic, using a Bayesian estimation algorithm, in the vicinity of the Old Dominion University campus. The results show that the source of harmful soot aerosol over the area of study was mainly located at signalized bottlenecks demonstrating the need to improve traffic signal operations.

To enhance air quality and mitigate congestion, a novel de-centralized traffic signal controller was developed using an NB game-theoretic optimization framework to adjust to changes in traffic conditions. The developed NB controller has the following features:

- Adapts signal timing based to observed real-time traffic conditions without using historical data.
- Decentralized − increases the scalability and robustness of the system.
- Model free − doesn't need an explicit model of the environment.
- Has a free cycle length with a flexible phasing sequence.
- Designed and evaluated on traffic scenarios that represent those found in the real-world, which will ensure that the controller is applicable to real situations.

The developed controller was tested on a signalized intersection considering different traffic demand levels and using observed traffic data. Results were then compared with the results

obtained using FP and ACT controllers. The simulation results for the isolated intersection show a reduction in the average travel time ranging from 37% to 65%, a reduction in the total delay ranging from 41% to 64%, a reduction in the queue length ranging from 58% to 77% and a reduction in the emission levels ranging from 6% to 17%. In addition, the performance of NB controller was tested on an arterial network, and compared to the performance of FP, PS, PSC, and PSCO controllers. The results show considerable reductions in the average travel time ranging from 7% to 21%, a reduction in the total delay ranging from 36% to 67%, and a reduction in the emission levels ranging from 6% to 13%. Results show that NB controller exhibits major improvements over other controllers, and is statistically significant. Results demonstrated a significant potential for the NB controller over other state-of-the-art and state-of-the-practice centralized and de-centralized controllers.

Several simulations were conducted on 38 intersections in the town of Blacksburg, Virginia. The results showed considerable reductions on the network in the average total delay of 19.3% and 22.6%, a reduction in the stopped delay of 51% and 61%, over PSC and PSCO controllers, respectively. To further investigate the achieved improvements using the NB controller, it was taken into consideration that the network has 459 stop signs and 30 yield signs, which might conceal the full degree of improvement achieved using the NB controller on the signalized intersection. Accordingly, we investigated the percent improvement in MOEs using the NB controller over the PSC controller over only the links that were directly associated with intersections. The results showed considerable reductions on the intersections links in the average travel time of 23.6%, a reduction in the average queue length of 37.6%, a reduction in the average number of stops of 23.6%, a reduction in the Co_2 emitted of 10.4%, a reduction in the fuel consumption of 9.8%, and a reduction in nitrous oxide (NO_X) emitted of 5.4%. The results reveal that the NB controller performs significantly better than the PSC and PSCO controllers.

Furthermore, the NB controller's performance was tested and compared to the performance of a PSC controller on an area of downtown Los Angles, California, which included the most congested downtown area with 457 signalized intersections. The results show considerable

reductions on the network in the average total delay of 14.5%, a reduction in the stopped delay of 25.1%, over the PSC controller. Moreover, the results show significant reductions on the intersections links in the average travel time of 35.1%, a reduction in the average queue length of 54.7%, a reduction in the average number of stops of 44%, a reduction in the Co_2 emitted of 10%, a reduction in the fuel consumption of 10%, and a reduction in NO_X emitted of 11.7%. The results reveal that the NB controller has significantly better performance potential than the PSC controller.

The results demonstrate that the proposed decentralized controller produces major improvements over other state-of-the-art centralized and de-centralized traffic signal controllers. The proposed controller is capable of alleviating congestion as well as reducing emissions and enhancing air quality.

1.5 Dissertation Roadmap

The dissertation is organized as follows:

Chapter 2: This chapter presents the necessary definitions and provides an overview and synthesis of the literature on traffic signal controllers.

Chapter 3: This chapter describes the formulation of the source localization problem, and presents the results for estimating the aerosol location in simulations and using in-field measurements.

Chapter 4: This chapter develops a de-centralized traffic signal controller using a game theoretic frame work, demonstrates the experimental setup, and the simulation results of applying the proposed approach on an isolated intersection.

Chapter 5: This chapter demonstrates the de-centralized mechanism of the proposed controller, and demonstrates the experimental setup and the simulation results of applying the proposed controller on an arterial network in downtown Blacksburg,VA composed of six intersections.

Chapter 6: This chapter presents how the de-centralized cycle-free NB controller with a flexible phasing sequence could be applied on large scale networks. It presents the experimental setup and the results of large scale studies on 38 signalized intersections on the town of Blacksburg, and the experimental setup and results of large scale studies on Los Angles downtown, including the most congested downtown area, with 457 signalized intersections.

Chapter 7: This chapter presents the summary and the conclusion of the work presented in this dissertation. In addition, it presents the recommendations for future work.

Publications:

- Hossam M. Abdelghaffar, Craig A. Woolsey, and Hesham A. Rakha, "Comparison of Three Approaches to Atmospheric Source Localization", in Journal of Aerospace Information Systems, 2017: p. 40-52.

- Hossam M. Abdelghaffar, Hao Yang, and Hesham A. Rakha, "Isolated traffic signal control using a game theoretic framework", in IEEE 19th International Conference on Intelligent Transportation Systems (ITSC), pages 1496-1501, Nov 2016.

- Hossam M. Abdelghaffar, Hao Yang, and Hesham A. Rakha, "Isolated traffic signal control using Nash bargaining optimization", in Global Journal of Researches in Engineering:B Automotive Engineering, 16:27-36, 2016.

- Hossam M. Abdelghaffar, Craig A. Woolsey, and Hesham A. Ali, "Source Localization For A Turbulent Plume Model Using Bayesian Occupancy Grid Mapping", in AIAA Guidance, Navigation, and Control Conference. 2015, American Institute of Aeronautics and Astronautics.

- Hossam M. Abdelghaffar, Hao Yang, and Hesham A. Rakha, "Developing a De-centralized Cycle-free Nash Bargaining Arterial Traffic Signal Controller", in the 5^{th} IEEE International Conference on Models and Technologies for Intelligent Transportation Systems, IEEE MT-ITS 2017.

- Mohamed I. Elbakary, Hossam M. Abdelghaffar, Kwasi Afrifa, Hesham A. Rakha, Mecit Cetin, and Khan M. Iftekharuddin, "Aerosol Detection Using Lidar-Based Atmospheric Profiling", SPIE Optics & Photonics, San Diego, August 2017.

- Hossam M. Abdelghaffar, Hao Yang, and Hesham A. Rakha, A Novel Game Theoretic De-centralized Traffic Signal Controller: Model Development and Testing, 97th Transportation Research Board Annual Meeting, Washington DC, January 2018.

Chapter 2

Literature Review

2.1 Background

Traffic growth and limited available capacity in the roadway system produces problems and challenges for transportation agencies. Traffic congestion affects traveler mobility and has an impact on air quality, and consequently on public health. The stopping and starting in traffic jams burns fuel at a higher rate than the smooth rate of travel, and contributes to the amount of emissions released by vehicles that create air pollution and are related to global warming. Reduction in traffic congestion improves traveler mobility and accessibility, while also reducing vehicle fuel consumption and emissions. Traffic congestion in 2013 cost Americans $124.2 billion and will rise to $186.2 billion in 2030 [2], a 50% increase in the cost of congestion. Accordingly, optimizing the utilization of the available infrastructure using advanced traffic signal controllers has become increasingly necessary to mitigate traffic congestion in a world with growing pressure on financial and physical resources. Traffic signals are one of the most effective and flexible active controls of traffic, where the conflicts arising from the movement of traffic in different directions are addressed by time sharing principle.

A signalized intersection is designed (controlled) to allow traffic flow to proceed efficiently and safely by separating conflicting movements in time rather than in space. Traffic signal control approaches attempt to minimize various traffic parameters (e.g., delay, queue length, and energy and emission levels), by optimizing traffic signal parameters, including the cycle length, phase scheme, phase split, and offset. Consequently, traffic signal optimization algorithms attempt to identify the optimal values of one or more traffic signal parameters for specific traffic conditions. A signal phase is the green interval plus the change and clearance intervals that follow it, where certain vehicles may travel through the controlled intersection, while others may not. Thus, during the green interval, non conflicting movements are assigned to each phase. The split is the fraction of the cycle time that is allocated to each phase for a set of traffic movements. Splits are typically provided in percentage form, in which case the sum of all the splits at an intersection must equal 100%. A signal cycle is one complete rotation through all phases. The time it takes to complete one cycle is known as the cycle length. It indicates the time interval between the starting of green for one approach until the next time the green starts. Offset is the time difference between the beginning of green phases for a continuous traffic movement at successive intersections that may give rise to a green wave along an arterial. Each intersection in the system has an offset. The offsets need not be the same from intersection to intersection; however, they need not necessarily be different either.

Traffic signal timing parameters could be identified as being in one of two categories: local intersection timing parameters and coordinated operation timing parameters [35]. The phase minimum or yellow change times are examples of local intersection timing parameters. The intersection cycle length, offset, and split are examples of coordination timing parameters. Having a common cycle length is fundamental to coordinated signal operation. The cycle length must be evaluated from two different perspectives: individual intersection and the group cycle length. For the individual intersection, the recommended approach is to focus on the one or two major intersections in the group. These are typically the intersections with the highest demand, as they will set the minimum cycle length limits. In general, for

a given demand condition, there is a cycle length that will provide the optimum two-way progression. This cycle length is a function of the speed of the traffic on the links between intersections and the link distance between intersections, called the resonant cycle. The important point to recognize when testing various resonant cycle lengths is that the speed of traffic is set based on what the average driver considers reasonable, not on an arbitrary speed that provides the maximum bandwidth. It is a common error to put a timing plan in the field that looks great on paper, but does not work in the field because the vehicles are traveling faster (or slower) than the assumptions. Another related issue is that the average speed is not necessarily consistent throughout the day. It may be lower during the peak periods or at night. Small errors in speed estimates can result in very poor signal timing (large offset errors), especially on suburban arterials where the distances between intersections are large. For example, estimating a speed of 30 mph when in fact the true speed is 35 mph will result in an offset error of 13 seconds on a $4,000$ foot link [36].

The offset is the heart of coordination signal timing. It is the difference in time from a reference point in the cycle at the upstream intersection to the same point in the cycle at the downstream intersection. This reference point is usually taken to be the beginning of the main street green, and the simplest offset to consider is the one-way offset when the light turns green as the upstream intersection and the platoon travels down the link, it is desirable for the downstream controller to change to green when the platoon approaches. This offset is appropriate for one-way streets and for situations when heavy demand in one direction justifies ignoring counter-flowing traffic. Notice that this explanation deals with one link between intersections. Except at the ends of an arterial, the intersections on an arterial have one intersection upstream and another intersection downstream. It is important to recognize that changing the offset timing at one intersection affects the relative offset on four links. Timing traffic signals in corridors is a multi-objective problem, in which optimizing the solution to one variable can often work to the detriment of another. For example, optimizing the timings relative to the arterial green band can cause excessive delay on the side streets. Conversely, optimizing solely on the basis of network delay does not

ensure an adequate green band on the arterial.

The traffic signal controller can be categorized as centralized or decentralized, where decentralized systems offer many advantages over centralized control systems [37]. Decentralized systems are computationally less demanding as they only require and maintain the relevant information from the surrounding intersections/controllers. Robustness is guaranteed in a decentralized control system, because if one or more controllers fail, the remaining controllers can take over some of their tasks. Decentralized systems are scalable and easy to expand by inserting new controllers into the system. Decentralized systems are often inexpensive to establish and operate, as there is no essential need for a reliable and direct communication network between a central computer and the local controllers in the field.

Traffic simulation, is the modeling of vehicle traffic systems for the purpose of investigating or planning transportation systems. These simulations offer a safe and convenient environment to investigate possible modifications to transportation systems. Traffic simulation models as a whole can be divided into two broad approaches (microscopic and macroscopic), with another approach (mesoscopic) being a hybrid of the two. Microscopic simulation relies on individual driver behavior. Each vehicle within the simulation environment is updated discretely using a car-following behavior to model the interaction of a vehicle and the preceding vehicle while traveling, considering behaviors such as gap acceptance and lane changing behavior. Instead of modeling individual vehicle behavior, macroscopic traffic simulation models rely on traffic flows, densities, and speed to model transportation systems. While macroscopic traffic flow models describe the behavior of a stream of vehicles along a roadway stretch, microscopic car-following models describe the behavior of a pair of vehicles within a traffic stream. Mesoscopic traffic simulation models combine elements of both macroscopic and microscopic traffic simulation. They typically model individual vehicles (a microscopic approach); however, the actions of these vehicles are based on overall averages (a macroscopic approach).

2.2 Related Work

Most of the currently implemented traffic signal systems could be categorized as one of the following: fixed-time plan controllers, actuated controllers, or adaptive controllers.

2.2.1 Fixed-time plan

A fixed-time plan controller is developed off-line using historical traffic data to compute traffic signal timings, where real-time traffic data is not considered. Thereafter, the order and duration of all phases remain fixed and do not adapt to fluctuations in traffic demand. As a result, these plans are known to age with time. As such, they are suitable for relatively stable and regular traffic flows. The traffic system is a dynamic system, one particular predefined traffic signal plan cannot efficiently fit all real-time traffic conditions [7]. What is really needed is dynamic data so that the traffic signals can change dynamically in terms of intervals to better move traffic around a network. In other words, instead of relying on what has happened in the past, it should be possible to dynamically change the traffic environment by using the information collected in real time. Two examples of software in this category are TRANSYT-7F, and PASSER.

TRANSYT-7F (TRAffic Network StudY) is a macroscopic deterministic optimization and simulation model that considers platoons of vehicles instead of individual vehicles. The model attempts to minimize a disutility index based on delay, stops, and queue lengths [8]. This approach has been found to only be appropriate for under-saturated conditions [9]. PASSER (Progression Analysis and Signal System Evaluation Routine) is an arterial-based, bandwidth optimizer (i.e., it maximizes the green band to move the anticipated platoon of vehicles through the arterial signal system without stopping) that computes phase sequences, cycle lengths, and offsets for a maximum of 20 intersections in a single run [9]. PASSER works within a given cycle length and split to find offsets that maximize an arterial green

band.

2.2.2 Actuated Control

Actuated traffic signal control, on the other hand, responds to changes in traffic demand patterns by implementing a window of green time (minimum green to maximum green) as opposed to the fixed green time in a fixed-time plan. This type of control requires that vehicle detectors be installed at approach stop lines to the intersection. The actuated timing plan responds to traffic demand by placing a call to the controller regarding the presence or absence of vehicles approaching or leaving the intersection, respectively. Once a call is received, the controller decides whether to extend or terminate the green phase in response to the actuation source.

The actuated control schemes have maximum green times equal to the fixed-time control. When traffic flows are consistently high, actuated control operates as fixed-time control. Actuated controller can be operated as semi-actuated control, where detectors are only placed on minor streets, best suited for locations where local minor streets intersect with arterials. Note, however, that while actuated signal control was proven to perform better than fixed-time traffic signal control in most cases, actuated traffic signal control does not offer any real-time optimization to properly adapt to traffic fluctuations. Consequently, actuated signal control is less sensitive to the traffic demand (i.e., number of vehicles) calling for the actuation and might result in very long queues in grid-like networks [10].

2.2.3 Adaptive Controllers

Adaptive traffic signal systems use detector inputs, historical trends, and predictive models to predict traffic arrivals at intersections. Adaptive systems have the potential to efficiently alleviate traffic congestion by adjusting the signal timing parameters in response to traffic fluctuations [6]. Using these predictions, they determine the best gradual changes in cycle

length, splits, and offsets to optimize an objective function, such as minimizing the delay or the queue length, for intersections within a predetermined sub-area of a network [11].

2.2.3.1 State-of the-Practice:

- **Centralized and off-line:** A library of pre-stored signal control plans are implemented. These plans are developed off-line on the basis of historical traffic data, e.g., morning peak, off-peak, afternoon peak, evening period, midnight period, and the day of week (e.g., weekday vs. weekend, Monday vs. Friday, etc.).

  Examples in this category include TR2 (Traffic Responsive Control Mode 2) [38], and UTCS-1 (Urban Traffic Control System-First Generation) [39]. Pre-timed plans age with time as traffic flows change. The optimization of the signal timings is conducted off-line, so it is incapable of handling stochastic variations in traffic patterns from day to day.

- **Centralized and on-line:** Controllers in this category are implemented using on-line optimization methods, to dynamically adjust the signal timings (offsets, cycle time and splits) by utilizing on-line surveillance information systems. Examples in this category include the SCOOT and SCATS systems.

  SCOOT (Split, Cycle, and Offset Optimization Technique) was developed in the UK in 1982. It minimize a performance index that is a function of delay and number of vehicle stops at all approaches in the network [12]. SCOOT performs effectively in under-saturated traffic conditions, and is a macroscopic model that does not capture microscopic behavior such as gap acceptance and lane changing behavior.

  SCATS (Sydney Coordinated Adaptive Traffic System) was developed in Australia in 1963, It monitors the traffic flows and headways at the stop bars [13], based on the volumes and headways gathered in one-minute intervals. Green times (splits) are reallocated to the phases of greatest need (i.e., in a hierarchical system). Traffic progression

along corridors is achieved in a centralized fashion that relies on communication often not scalable to expand the size of the network, that is relatively complex to operate with many parameters to be adjusted by a human operator, and is expensive.

- **De-centralized and on-line:**

  Controllers in this category are decentralized, computationally less demanding, robust, scalable, inexpensive, and use dynamic programming that captures the stochastic nature and dynamics of the traffic system. Examples in this category are RHODES (Real-Time, Hierarchical, Optimized, Distributed, and Effective System) [14] and OPAC (Optimized Policies for Adaptive Control) [15].

  OPAC was the first to recognize the need to migrate from parametric models, which optimize parameters such as cycle time, splits, and offsets, to non-parametric models, in which the decision to switch between phases is based on actual arrival data at the intersection. OPAC uses two levels of control in a decentralized fashion: a local level and a network level. At the local control level, OPAC determines the next phase at the intersection. At the network control level, OPAC provides progression. RHODES optimizes an objective function for a specified rolling horizon (using traffic prediction models) and has pre-defined sub-areas (limited flexibility) in which the signals can be coordinated.

  RHODES and OPAC are based on dynamic programming that require a state transition probability model for the traffic environment, which is difficult to obtain. The number of states that could represent wide traffic conditions is typically massive. Therefore, dynamic programming algorithms are computationally intractable [40].

Although existing adaptive traffic systems offer improvements in performance over fixed-time plans and actuated controllers, they still suffer from combinations of the following limitations:

- Operation is constrained by maximum and minimum values for cycle lengths, splits,

and offsets.

- Centralization limits the scalability and robustness of the overall system in cases of communication failure.
- They are expensive to install and maintain–SCOOT installation costs between $\$20,000$ and $\$90,000$ per intersection, and OPAC costs between $\$20,000$ and $\$128,600$ per intersection [41].
- Complexity of the system increases exponentially with the number of intersections when the network is expanded [16].
- They require an accurate traffic modeling framework.
- Most sophisticated traffic control systems use hierarchies that either partially or completely centralize the decisions, making the systems more vulnerable to failures in one of the master controllers. Hierarchies also make systems more difficult to scale up, as centralized computers must interconnect all intersections.

2.2.3.2 State-of the-art:

A number of different intelligent techniques have been investigated in the domain of traffic signal optimization domain, and are still under continuous research and development.

- **Genetic Algorithm:**

  The genetic algorithm is known to be an algorithm for locating the best optimal solution throughout the evolutionary process of the possible solutions [42]. The problem is modeled as an imitated biological environment, where all the possible solutions are treated as individual chromosomes in a population [43]. The concept of a genetic algorithm allows the population of solutions to compete and survive through the evolution, and only the fit and strong solutions will be left surviving at the end of the

evolution [44]. In genetic-algorithm-based optimization traffic signal timing management, a chromosome contains intersection's signal timing parameters, such as cycle length, green split, phase sequence, and offset, as these are the parameters which tend to be optimized [45], [46].

Chin et al. [47], proposed a fitness function to evaluate the individual chromosome based on traffic delay and fluency on two intersections with a single lane on each link. They used a selection algorithm that is a combination of a ranking and elitist selection method. Vogel et al. [48], applied an approach that evolved three chromosomes (phase, phase order, green), to encode the various parameters necessary to define the traffic signal plan for an isolated intersection. Phase chromosome encodes which flow directions belong to each phase, where the number of chromosomes used depends on the number of phases, which can range from 2 to the number of flow directions. Phase order chromosome encodes the order in which the phases of the signal plan occur. Green time chromosome contains the amount of green time that should be allocated for each phase.

Genetic algorithms can solve simple networks, and deal with static traffic volumes. However, as the networks increase in size, the search space involved in finding effective signal plans will increase significantly, and a large amount of centralized computing power is required. Genetic algorithms are a biomimetic method for global optimization, and are not apt to be trapped in local optima because of their characteristics of random search and implicit parallel computing. However, encountering a large-scale problem, this method will spend an inordinate amount of time to converge to the optima. It is disadvantageous for on-line optimization of area traffic coordinated control. Moreover, the convergence rate is sensitive to parameters selected, which depend on practical problems to be solved. And so, applying the genetic algorithm to area traffic coordinated control is limited [49]. In addition it is not certain that the local solution obtained is also the global optimum [50].

- **Fuzzy Logic:**

  The idea of fuzzy logic was first proposed by Zadeh [51], where truth values of variables can take on a continuous value in the range of $]0;1[$, as opposed to the traditional binary truth values of 0 or 1. For example, is the traffic volume in a traffic network currently low or high? Fuzzy logic allows truth values such as 0.7 = low and 0.3 = high. Decisions in fuzzy logic are usually made using a rule base, which can be developed using expert knowledge, trial-and-error, or an automatic method such as a genetic algorithm. A fuzzy traffic signal controller uses linguistic rules in the following form: if variable1 is value1 then output (e.g., if the approaching traffic volume is large and the queuing traffic volume is small, then the green signal is long). The performance of the controller greatly relies on the effectiveness of the rules developed and it can be difficult to determine if the rules being used are efficient.

  The first application of fuzzy logic in the traffic signal control domain was proposed by Pappis [52] for an isolated intersection. This approach consisted of 3 input variables: time (very short, short, medium, long, and very long), recent arrivals at the green phase (none, few, medium, many, too many) and queue length at the red phase (very small, small, small plus, long, very long). The rule base, which was developed by trial-and-error in this case, produces a single output from these inputs, which is the extension time for the current phase. As opposed to using the extension principle, Chiu and Chand [53], designed a controller which adjusts phase split, offset, and cycle length, where the rule base remains static and does not adapt along with changing traffic parameters, which can lead to degraded performance over time as the system does not generate a predictive model of traffic.

  Ella [54], proposed a neurofuzzy controller, where the parameters of the fuzzy membership functions were adjusted using a neural network. The neural learning algorithm in this work was reinforcement learning. The learning algorithm was found successful at constant traffic volumes, and fails when the traffic volume changes rapidly.

Membership functions are the building blocks of fuzzy set theory (i.e., fuzziness in a fuzzy set is determined by its membership function). Accordingly, the shapes of membership functions are important for a particular problem since they have an effect on a fuzzy inference system. The concepts large, small and long are fuzzy sets. That is, they are not precise, and elements belonging to one set may partially belong to some other set too. For example, a measurement of 5 vehicles is small to some degree and also large to some other degree. Most of the fuzzy traffic signal controllers are not adjustable. In other words, the parameters of the fuzzy controller remain the same in changing traffic situations. Most researchers work at control at an isolated intersection. A traffic coordinated control system is a complex large-scale system with many factors interacting with each other, and it is more appropriate to use fuzzy control methods for traffic signal control of the isolated intersection [49].

- **Neural Networks:**

  The neural network based control signal depends on a set of weighted coefficients, which must be estimated. Once these weights are properly specified, the control signal takes state information on traffic conditions at any given time and produces optimal instantaneous signal light timings.

  Spall et al. [55], presented an approach for optimal light timing based on a neural network serving as the basis for the control law, with the weight estimation occurring in closed loop mode via the simultaneous perturbation stochastic approximation (SPSA) algorithm, by which the neural network controller weights are estimated (trained) at least once a day. This approach was illustrated by simulation on a six-intersection network with moderate congestion. This model, had two shortcomings. First, the approach involved the use of heuristics to manually identify the general traffic patterns (morning and evening peaks) and the assignment of time periods for each pattern. The robustness of the system may come into question if the fluctuations of the traffic volume in the traffic network are not periodic. Second, a neural network is assigned

to each time period, and the weights of the neural network are updated only during the duration of the time period. This implies that the weight update is done only on a daily basis whenever the same traffic pattern and time period arises. As such, the traffic controllers may not be able to respond well to changes in the traffic network within the same time period. The neural network has to be re-updated time and again to take into consideration changes in the long-term dynamics of the traffic network even after the convergence. Srinivasan et al. [56], strives to avoid the limitations of [55], by developing a distributed unsupervised traffic responsive signal controller using a neurofuzzy algorithm.

Various approaches have been proposed for designing real-time traffic signal controllers using neural networks. Most of these works are based on the distributed approach, where an agent is assigned to update the traffic signals of a single intersection based on the traffic flow in all the approaches of that intersection. The effectiveness of the proposed neural controller for controlling a large-scale traffic network with multiple intersections cannot be established. Neural networks adapt very slowly to changing traffic parameters, where online learning has to take place continuously once the agent-based traffic signal controllers are implemented into the traffic network. Some works require multiple models to be maintained for various times within a day. The inner-workings of neural networks are often hard for humans to understand.

- **Reinforcement Learning:**

Reinforcement learning (RL) is inspired by behavioral psychology. It is a machine learning approach which allows agents to interact with the environment, attempting to learn the optimal behavior based on the feedback received from interactions. The feedback may be available right after the action, or several time steps later, which makes the learning more challenging [57]. This typically involves breaking the environment into states, from which each agent can select a possible action. The reward gained from taking an action within a state determines the level of reinforcement, which in turn

affects the likelihood that the agent will select that action when it is next in that state. Reinforcement learning is based on the idea that if an action has good consequences, then the tendency to produce that action is strengthened. [58] .

Wiering [59], utilized model-based RL, with state transition models and state transition probabilities, to control traffic-light agents to minimize the waiting time of vehicles in a small grid network. In that study, agents correspond to the traffic signals but the learning task is designed such that the state representation is a function of the waiting time for individual vehicles (i.e. vehicle-based state representation), aggregated over all vehicles around the intersection. The network is discretized into a number of lanes and each lane is discretized into possible places for cars, called cells. As a result, the number of states grows with the number of lanes and the number of vehicles occupying each cell in a lane. Therefore, the number of states grows intractably with the network size and traffic volume which makes it impractical to implement in medium or large-scale traffic networks. Even for relatively small networks, the number of states will increase exponentially with the increase in the number of vehicles, resulting in slow convergence speed.

Abdulhai et al.[60], applied a model-free Q-learning technique to a simple two-phase isolated traffic signal in a two-dimensional road network. According to the state information that includes the queue lengths on the four approaches, the agent chooses to either remain in the current phase or to change it, with the goal of minimizing the average number of waiting vehicles in all approaches. In the uniform and constant profile cases, Q-learning either slightly outperformed or was equal to the pre-timed control.

Salkham et al. [61], applied a Q-learning strategy that allowed an agent to exchange rewards with its neighbors on 64 signalized intersections. The state-action space was simple and very time coarse. Each agent decided the phase splits every two cycles, which did not capture of the rapid dynamics of congestion–coordination between the agents actions was missing.

Studies have considered the use of RL algorithms for traffic control, but they are very limited in terms of network complexity and traffic loadings, so that realistic scenarios, over saturated conditions, and transitions from under saturation to over saturation (and vice versa) have not been fully explored. Many questions remain open about the adequate management of RL agents when the traffic demands are not balanced (in terms of volume, number of lanes, and link length), when the demand changes over time, and when the volumes exceed the capacity of the network so that the signal control should prevent queue overflows. The advantage of reinforcement learning is that it is not necessary to establish a mathematic model for the external environment. However, there is also a disadvantage in that it converges slowly.

- **Feedback Control:**

  Ekbatani et al. [62], [63], developed a strategy that exploits the network fundamental diagram for urban networks to improve mobility in saturated traffic conditions via application of gating measures, based on simple feedback control structure (PI controller). The idea is to hold traffic back (via prolonged red phases at traffic signals) upstream of the links to be protected from over-saturation, whereby the level or duration of gating may depend on real-time measurements from the protected links, which may result in a long queue and delays at the gate. Gating at the border of the network may not be applicable if there are no proper links to store the gated vehicles (queuing), or if there are an insufficient number of signalized junctions.

  The linear quadratic controller (LQR) controller is a well-known controller for minimizing cost functions. The LQR controller has been tested and proven to be effective [64], [65]. Konstantinos et al. [66] addressed the problem of real-time traffic signal control using an LQR controller that minimized and balanced the relative occupancies of the network links using a simplified continuity equation. The proposed strategy didn't capture driver behavior or the car-following behavior that modeled the interaction of a vehicle and the preceding vehicle. This strategy did not evaluate the performance of

the system with the changing traffic volume.

- **Game Theory:**

  Game theory studies the interactive cooperation between intelligent rational decision makers, and has been widely used in economic, military, and communication applications. Game theory has also been applied to model traveler route choice behavior [20], control connected vehicle movements [21], and to in-route guidance [22]. The literature indicates that investigation of game-theoretic traffic signal control is very limited.

  Bargaining theory is related to cooperative games through the concept of Nash bargaining. A bargaining situation is defined as a situation in which multiple players with specific objectives cooperate and benefit by reaching a mutually agreeable outcome. The bargaining process is the procedure that bargainers follow to reach an agreement (outcome), and the bargaining outcome is the result of the bargaining process. [23], [24]. The Nash bargaining solution has been applied in a number of applications, including multimedia resource management [25], allocating multi-user channels to networks [26], a wireless cooperative relaying network [27], investment, wages and employment [28], [29], and for downlink beamforming in an interference channel [30].

2.3 Summary

Traffic flow is highly dependent on factors such as time-of-day, day-of-the-week, weather, and unpredictable events such as incidents, special events, work zones, etc. Consequently, improvements to traffic signal control strategies could be made if the control system is able to not only respond to the actual conditions found in the field, but also to adapt their actions to transient conditions.

This chapter outlines a number of approaches that have been applied to the domain of traffic signal control. The reviewed literature showed that many methodologies have been proposed to date. However, it also revealed that the field operations of traffic signals in congested net-

works and saturated traffic conditions are still under development and that there is still room for new developments. Various computational intelligence-based approaches have been proposed for designing real-time traffic signal controllers, such as fuzzy sets, genetic algorithm and reinforcement learning, and neural networks. Most of these approaches have implemented and tested the controller on an isolated intersection where the effectiveness of the proposed controllers for controlling a large-scale traffic network with multiple intersections cannot be established. Improved optimization approaches are constantly being developed. There are currently no commercially available off-the-shelf tools to address these problems, and even the literature offers little structured guidance to accomplish this task.

Accordingly, this dissertation attempts to develop a novel traffic signal controller that meets a number of requirements. First, the controller should be able to adapt signal plans based on observed traffic state without using historical data, which tends to be inaccurate, resulting in inefficient signal plans. Second, the developed control system should be de-centralized, which will increase both the scalability and robustness of the system, to avoid the problems inherent with complex centralized communication. Decentralized systems are often inexpensive to establish and operate, as there is no essential need for a reliable and direct communication network between a central computer and the local controllers in the field. Finally, the controller should be designed and evaluated on traffic scenarios that closely represent those found in the real-world, which will ensure that the controller is not only capable of solving simple traffic problems, but is also applicable to real situations. This controller should increase the traffic handling capacity of roads, and reduce unnecessary stop-and-go vehicular movement, which will reduce fuel consumption and, accordingly, air pollution.

Chapter 3

Source Localization

3.1 Introduction

The source localization problem is especially difficult in a turbulent flow environment, such as the planetary boundary layer. Plume effluent in a turbulent wind spreads in a random manner, meandering to create patches of high and low concentration [67]. The plume width and the concentration within the plume do not vary predictably in time or space [68]. The uncertain relationship between the location of a detection and the location of the source in a turbulent flow makes source localization challenging. Various algorithms have been proposed for the source localization problem, including gradient descent, biologically inspired approaches, and probabilistic methods.

Gradient descent is an iterative optimization technique capable of finding a local minimum within some scalar field. For example, Rozas et al. [69] proposed a mobile robot equipped with an electronic nose to follow a gas concentration gradient to its source. Russell [70] proposed a gradient based algorithm with a hex-path trajectory in which a burrowing robot followed an underground chemical concentration gradient to its source. Each of these methods demonstrated the concept of using concentration gradients to guide robot navigation.

Bachmayer et al. [71] implemented a gradient descent algorithm on a vehicle network, to find a single gradient source. Zhang et al. [72] proposed a gradient driven model to predict target locations, constructing a gradient distribution function to localize the source. Gradient descent method is not guaranteed to find a global optimum. Further, gradient descent algorithms are likely to be ineffective in turbulent flow environments unless the turbulent statistics are stationary and the measured data are averaged over a sufficiently long period of time.

Biologically inspired source localization algorithms emulate the behavior of living creatures that solve similar problems; these algorithms also feature sampling of a concentration gradient and elements of the hill climbing approach. For example, Lilienthal [4] described a source localization strategy based on the behavior of the male silkworm moth, which follows a pheromone signal emitted by a female moth. The simple, biomimetic decision strategy of moving upwind with every positive detection and moving across-wind with every non-detection can be quite effective, especially in a completely random environment; the approach relies only on instantaneous measurements, ignoring all previously collected information. Hayes et al. [73] derived an odor source localization strategy (spiral surge), to implement a distributed and cooperative search based on odor and wind measurements in an environment with background flow. Ferri et al. [74] applied a modified spiral algorithm in the absence of airflow by relying on communication between agents rather than wind measurements to localize the source. Cui et al. [75] developed a swarm based fuzzy logic algorithm to locate a single hazardous emission source in the presence of multiple local emission concentrations. Swarming algorithms have provided more robust solutions to the single source problem.

Probabilistic methods can be considered a compromise between the gradient descent approach and the biomimetic approach. In these methods, a probabilistic estimate of the concentration field (perhaps a time- and space-averaged estimate) is constructed, enabling assessment of the likelihood that a given point is the source location. Farrell [76] presented a plume mapping approach based on hidden Markov methods to estimate the likelihood that

a given point is the source location. Pang and Farrell [5] proposed the use of a Bayesian occupancy grid for estimating the source location of a chemical plume in water using an autonomous underwater vehicle, where the plume effluent was simulated using a random walk model. In this approach, a source likelihood map is propagated through time; the likelihood that each cell contains the source is updated in response to each detection and non-detection event. Li et al. [77] proposed a particle filter algorithm to estimate the location of a source in a time-varying flow environment using Bayesian filtering techniques. Kalman filters provide variations on the traditional Bayes filter to estimate the state of a dynamic system from noisy or uncertain measurements, used to locate and track moving sources. An extended Kalman filter is a modified formulation of the Kalman filter which applies a linear approximation of the nonlinear system about the state estimate. Skliar and Ramirez [78] presented Kalman filter algorithm to estimate unknown contaminant source location in closed environment, using molecular diffusion law (Ficks law) to model the contaminant dispersion. Niri et al. [79] presented nonlinear extended Kalman filter algorithm to estimate the location of acoustic emission sources in anisotropic panels. The algorithm were compared with a traditional least square method. The accuracy and the computational efficiency of the proposed framework demonstrated its potential application in real-time. However, more tests need to be conducted to verify the robustness of the approach to a variety of sources and changing environmental conditions. Sun et al. [80] presented Kalman filter algorithm based on outliers for sound source localization. However, the results showed that the localization accuracy will decline as the system model change, and the filter estimates will be completely wrong.

To investigate the spatial relationship between air quality and traffic flow patterns, a source localization strategy to identify the source location (correlated with traffic flow) of an airborne contaminant (soot) in a turbulent wind field was developed. Simulation studies were conducted to demonstrate relative strengths and weaknesses of source localization strategies, these simulations were preliminary steps toward the planned experiment. In simulations, a contaminant is released into the turbulent planetary boundary layer. The objective is to

detect and locate the source of the contaminant using a unmaned aircraft systems (UAS) flying at a constant altitude, that emulate the capability of sensing the contaminant in the atmosphere. In such an application, a UAS samples the atmosphere to determine whether a contaminant is present and is then directed by a decision-making algorithm to the next sample location. If the sensor is capable of measuring the contaminant's concentration, this information may also be used by the decision-making algorithm. It is assumed that there is a single source at a fixed location, emitting a contaminant at a constant rate. The contaminant distribution within the plume is non-Gaussian [81], so numerical validation of a given localization strategy requires a reasonably sophisticated environmental model. TurbSim [82] was used to generate a turbulent wind field along with advection/diffusion model [18] to generate a time-evolving concentration field. Once the plume has matured, we freeze the scalar field and implement one of the three source localization algorithms: a recursive Bayesian estimation algorithm, a gradient descent algorithm, and an extended Kalman filter algorithm. Then, an experimental investigation based on real flow conditions was conducted to estimate the source location of the aerosol (soot), that can be attributed to traffic, following the recommendations from the simulation results.

This chapter presents a formulation for localizing the source location of a contaminant being released into the atmosphere using three estimation algorithms. In addition, it shows an experimental investigation for estimating the aerosol location in real flow conditions, using collected field measurements. This chapter is organized as follows. Section 3.2 describes the method used to simulate a turbulent atmospheric flow and the model used to compute the concentration of a contaminant released into that flow. Section 3.3 describes the Bayesian estimation (BE) algorithm, the gradient descent (GD) algorithm, and the extended Kalman filter (EKF) algorithm used to estimate the location of the contaminant's source. Section 3.4 shows results of the source localization strategy using the atmospheric plume simulation. Sections 3.5 and 3.6 present the experimental setup and the results for estimating the aerosol location in real flow conditions using collected measurements. Section 3.7 summarizes the work.

3.2 Contaminant Simulation

This section describes the method used to simulate a turbulent atmospheric flow (Section 3.2.1) and the model used to compute the concentration of a contaminant released into that flow within a three-dimensional plume (Section 3.2.2). These simulations are preliminary steps toward planned experiments.

3.2.1 Wind Field

To create a representative plume, a wind field was first generated using a stochastic, full-field turbulent wind simulator called TurbSim [17]. TurbSim generates a time series of three-component wind vectors at points in a two-dimensional vertical rectangular grid. Developed to simulate the flow through a wind turbine under a variety of wind conditions [82], TurbSim is used to study the impact of wind fluctuations, wind shear, and tower shadow on the voltage and power generated by a wind power plant [83]. The turbulence model can be adjusted using various TurbSim parameters such as runtime options, meteorological boundary conditions, and coherent turbulence scaling. Although the tool was developed to study wind turbine performance, we adapted it to the problem of an atmospheric plume by allowing each rectangular flow field to "advect" downwind at the mean wind speed.

For the purpose of generating a turbulent wind field using TurbSim, we defined a right-handed reference frame in which the coordinate x represents downwind distance, y represents crosswind distance, and z represents height. The turbulent wind field was generated at points on a vertical grid 400 m wide (ranging from $y = -200$ m to $y = 200$ m) and 200 m high in time steps of 0.05 s. The mean wind speed was 5 m/s at a reference height of 50 m, with a horizontal mean flow (skew) angle of 5° and a vertical mean flow (uptilt) angle of 5° [84]. The Kaimal turbulence model was used to set the meteorological boundary conditions. TurbSim generates a sequence of wind field "snapshots" in a vertical, rectangular

grid within the y-z plane. To generate a three-dimensional flow field, each wind field snapshot was advected downwind at the mean horizontal wind speed [84]. This resulted in a three-dimensional turbulent wind field within a rectangular tube, which grew with time in the x direction. Although this approach was not the most accurate method for simulating a three-dimensional turbulent flow field, our aim was to compare source localization strategies using a plume model that balanced realism and efficiency. The numerical results described here are preliminary to planned field experiments, where turbulent flow characteristics will be measured directly.

3.2.2 Contaminant Plume Model

In simulating the evolution of a contaminant plume within the turbulent planetary boundary layer, the challenge is to represent the complex process of diffusion and advection in a computationally efficient way. The plume model presented by Farrell et al. [18] produces a realistic, short time-scale signature for sensed concentrations and accurately reproduces the long-term time-averaged plume behavior. In this approach, a simulated plume is generated as a sequence of puffs released from the source location at regular intervals. Each puff comprises a number of "filaments" and each filament is advected along some three-dimensional path defined by the flow velocity generated using TurbSim. To account for diffusion, each filament is assumed to contribute to the overall contaminant concentration, a scalar field. The contribution diminishes with distance from the filament and with the time elapsed since the filament's release.

Let $\boldsymbol{p}_i$ denote the three-dimensional position of the i^{th} filament in centimeters (cm). Also, let the time-varying parameter $R_i(t) > 0$ denote the "spread" of the filament in cm. Define a time-varying distance parameter $R_i(t) = (R_0^{2/3} + \gamma t)^{3/2}$, where the initial filament size R_0 and the growth rate parameter $\gamma > 0$ may be adjusted to match some observed turbulence statistics. We consider a source of strength Q particles per filament located 5 m above the origin of the reference frame defined in Section 3.2.1. Given these parameters, the

contribution of the i^{th} filament to the concentration at a point $\underline{\boldsymbol{x}}$ in three-dimensional space at time t is

$$C_i(\underline{\boldsymbol{x}}, t) = \frac{Q}{\sqrt{8\pi^3} R_i^3(t)} e^{\left(-\frac{r_i^2(t)}{R_i^2(t)}\right)} \frac{\text{particles/filament}}{\text{cm}^3} \tag{3.1}$$

where the distance between the filament and a given point

$$r_i(t) = \|\underline{\boldsymbol{x}} - \boldsymbol{p}_i(t)\|$$

is measured in cm for dimensional consistency. Given a total of N filaments, the instantaneous concentration at $\underline{\boldsymbol{x}}$ is

$$C(\underline{\boldsymbol{x}}, t) = \sum_{i=1}^{N} C_i(\underline{\boldsymbol{x}}, t) \frac{\text{particles}}{\text{cm}^3} \tag{3.2}$$

Filaments were released at one second intervals, and the plume evolved according to a flow field generated using TurbSim, as discussed in Section 3.2.1, with the following parameter values:

$$\gamma = 0.1 \text{ cm}^{2/3}/\text{s}, \qquad R = 40 \text{ cm}, \qquad \text{and} \qquad Q = 2 \text{ particles/filament}$$

The heat map in Figure 3.1 shows the 5-minute time-averaged contaminant concentration at a UAS operating altitude of 40 m over the range $x \in [0, 1400]$ m and $y \in [-250, 250]$ m. The locations of the filaments that contributed to the concentration field, according to equations (3.1) and (3.2), are denoted by red dots. Note that there are multiple local maxima; the concentration field is clearly non-Gaussian.

3.3 Estimation Algorithms

This section presents three algorithms for estimating the location of a contaminant source: a recursive Bayesian estimation (BE) method described in Section 3.3.1, a gradient descent

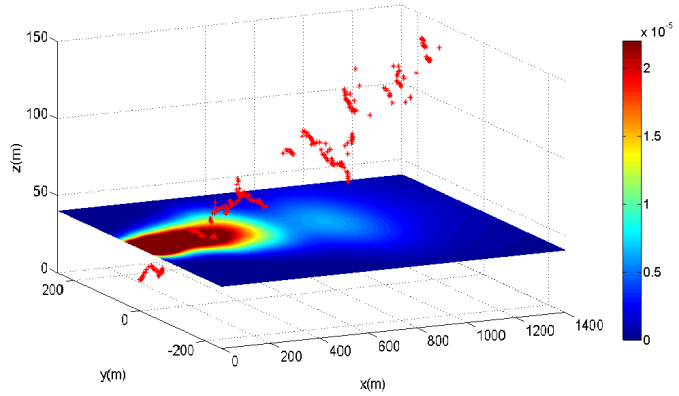

Figure 3.1: Three-dimensional filament locations and 5-min time-averaged concentration (in particles/cm^3) at a 40 m altitude.

(GD) method described in Section 3.3.2, and an extended Kalman filter (EKF) described in Section 3.3.3.

3.3.1 Bayesian Estimation Algorithm

The notion of an occupancy grid map (OGM) was developed in the 1980s as a means to represent uncertainty in a robot's environment. In an OGM, the environment is discretized into contiguous cells, each of which is assigned some likelihood of being occupied (e.g., by an obstacle). This likelihood is then updated based on measurements. The approach is often used for robot path planning, but it has also been applied to the problem of localizing a gas source in an indoor environment [85]. In this latter application, BE can be used to update the probabilities associated with each grid cell whenever a measurement is taken [86]. For simplicity, we consider a two-dimensional OGM, seeking only the x-y coordinates for the source location at the UAS operating altitude of 40 m.

Let $\boldsymbol{\xi}$ represent the (two-dimensional) coordinates for the center of a grid cell, which is a candidate location for the contaminant source, and let $p(\boldsymbol{\xi})$ represent the probability, prior to some measurement or observation, that the source is located at $\boldsymbol{\xi}$. Let ζ represent some observation that may support the hypothesis that the source is located at $\boldsymbol{\xi}$. The

posterior probability that the source is at location $\boldsymbol{\xi}$ given the observation ζ is denoted $p(\boldsymbol{\xi}|\zeta)$. Conversely, $p(\zeta|\boldsymbol{\xi})$ represents the likelihood of obtaining the measurement ζ given that the source is located at $\boldsymbol{\xi}$. Bayes' rule states that

$$p(\boldsymbol{\xi}|\zeta) = \frac{p(\zeta|\boldsymbol{\xi})p(\boldsymbol{\xi})}{p(\zeta)} \tag{3.3}$$

(The term $p(\zeta) = \sum_{\xi} p(\zeta|\boldsymbol{\xi})p(\boldsymbol{\xi})$ serves to normalize $p(\boldsymbol{\xi}|\zeta)$.) Bayes' rule enables iteratively updating the likelihoods associated with each cell in an OGM, incorporating new knowledge each time a measurement is made.

To apply BE to the given source localization problem, the probabilities associated with each cell in the OGM are initialized to some uniform, low value. A simulated UAS follows a predefined search pattern, visiting a sequence of sample points. Initially, sample points are selected by simply "mowing the lawn" in the cross-wind direction within a bounded search area. As Figure 3.4 shows, the search pattern for the simulations described here begins at the top right; the mean wind is from the left.

Conceptually, the UAS orbits a sample point until the sensor has collected enough air to process a sample and determine the contaminant concentration [87]. If the concentration does not exceed the sensor's minimum threshold value, the UAS continues to the next grid cell in the lawn mower pattern. If the concentration exceeds the threshold value, the measured concentration is used to update the posterior probability for all cells in the grid and the UAS is directed to the grid cell with the highest probability of containing the source. The strategy is outlined in the left branch of the flow chart in Figure 3.2.

In the Bayesian localization algorithm, the posterior probability distribution over the grid is updated recursively, given the set of measurements $z_{1:k}$:

$$p(\boldsymbol{x}_k|z_{1:k}) = \frac{l(\boldsymbol{x}_k|z_k)p(\boldsymbol{x}_k|z_{1:k-1})}{\sum l(\boldsymbol{x}_k|z_k)p(\boldsymbol{x}_k|z_{1:k-1})} \tag{3.4}$$

where $l(\cdot|\cdot)$ is a conditional likelihood function and where the summation in the denominator

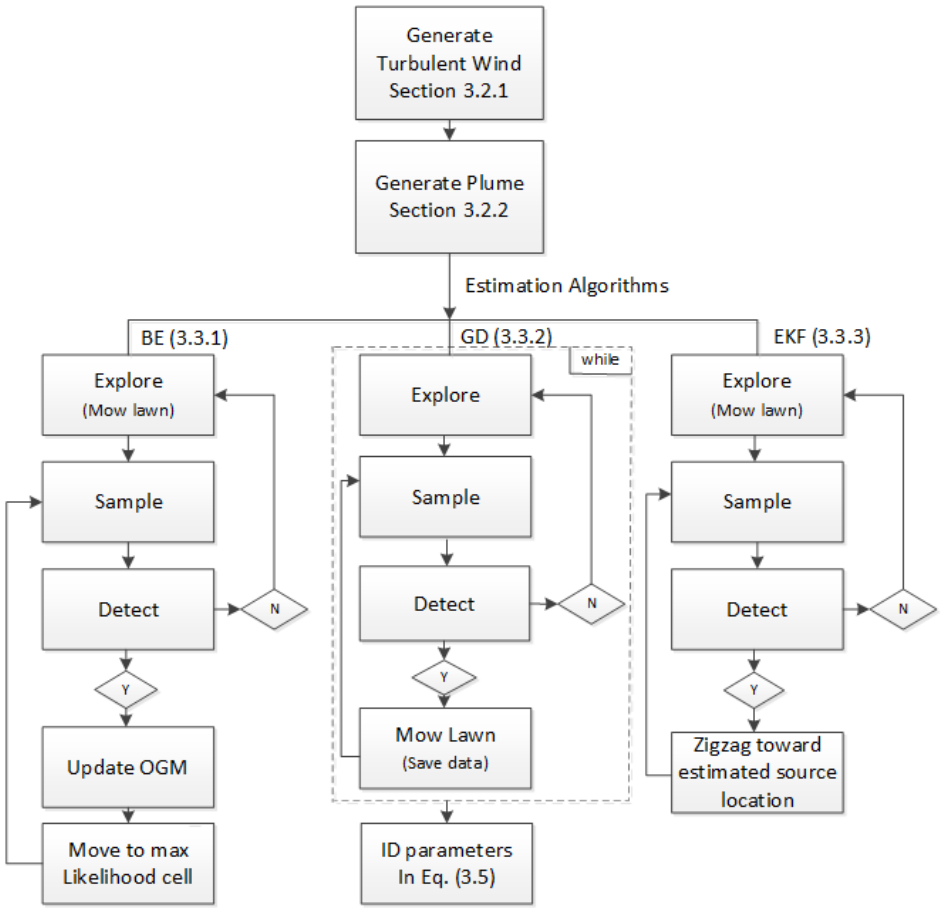

Figure 3.2: Flow chart for implementing the three estimation algorithms.

is taken over the entire grid. (Recall that here $\boldsymbol{x}$ represents the x-y coordinates of a candidate source location). The map is updated after each detection and the estimated source location is defined as the point at which $p(\boldsymbol{x}_k|z_{1:k})$ is maximum. Appealing to the central limit theorem, we adopt a Gaussian likelihood function. The mean value of the Gaussian likelihood function is the center point of the grid cell and the 2×2 covariance matrix is diagonal, with diagonal elements given by the maximum possible variance in x and y, respectively, for the given search area.

3.3.2 Gradient Descent Algorithm

We compared the localization strategy described in Section 3.3.1 with two alternatives: a GD approach and an EKF. These alternative algorithms use a low-dimensional parametric model for the concentration field.

In this section, we consider a GD method presented by Ishida et al. [1]. The method involves comparing the measured concentration with that predicted by the parametric model and updating the model's parameters based on this difference. Because the parameters include the source location, the GD method produces an estimate of this location. The UAS makes a sequence of measurements along a path, generating a time-history of measurements obtained using "true" data from Section 3.2. This measurement history is then compared with a sequence of measurement histories predicted by the parametric plume model, with the plume model parameters updated according to a GD algorithm that minimizes the (sum of squares) error between the measured and modeled time histories.

To obtain a time-history of concentration measurements, the UAS begins operation in a cross-wind lawn mower pattern until a detection occurs, i.e., until a sampled concentration exceeds the sensor's threshold. Upon obtaining a measurement, the UAS continues this cross-wind lawn mower pattern, turning upwind and reversing course at each new non-detection. If there are consistent non-detections, suggesting that the UAS is upwind of the source, the system retraces its earlier course in reverse until a specified time has elapsed. See the central branch of Figure 3.2.

The plume model presented by Ishida et al. [1] produces a time-averaged, two-dimensional contaminant distribution in a one-directional wind field with constant wind speed. A contaminant source is assumed to be located at (x_s, y_s) as shown in Figure 3.3. The contaminant concentration at a point (x, y) is

$$C_0(x, y) = \frac{p_1}{d_s} e^{-p_2(d_s - \triangle x)} \tag{3.5}$$

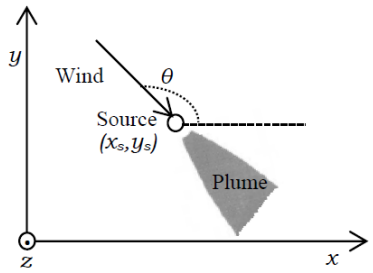

Figure 3.3: Coordinate system used to present the plume (Adapted from [1]).

where

$$p_1 = \frac{q}{2\pi K}$$

$$p_2 = \frac{U}{2K}$$

$$d_s = \sqrt{(x_s - x)^2 + (y_s - y)^2}$$

$$\triangle x = (x_s - x)\cos\theta + (y_s - y)\sin\theta$$

where q is the emission rate, K is the turbulent diffusion coefficient, U is the wind speed, and θ is the angle from the x-axis to the upwind direction. The hypothesized plume model is a function of the known measurement location (x, y) and five unknown parameters to be estimated (q, U, x_s, y_s, θ). The function relating the contaminant concentration $C_0(x, y)$ and the steady state sensor response r_0 is

$$r_0(x, y) = (1 + \alpha C_0(x, y))^{-\beta} \tag{3.6}$$

This static nonlinearity scales and amplifies the measured concentration so that the measurements can be effectively used in the GD method. The values of the parameters α and β depend on a particular sensor. We take $\alpha = 0.23$ and $\beta = 0.67$ to be consistent with [1].

The dynamic response of the sensor is approximated using a first order discrete-time system:

$$r_k = \gamma\ r_{k-1} + (1 - \gamma)\ r_0(x_{k-1}, y_{k-1}) \tag{3.7}$$

where r_{k-1} is the sensor response at time step $k-1$, (x_{k-1}, y_{k-1}) is the location of the UAS, and the parameter γ is set at 0.95, as in [1].

The location of the contaminant source is estimated by adjusting the parameters $(x_s, y_s, \theta, p_1, p_2)$ to fit the response from Equation (3.7) to the time series contaminant sensor response measured during the movement of the UAS. The model curve is fitted using the off-line GD algorithm to minimize the sum of the squared error between the measured response $\mathbf{r}_{\text{measured}}$ and the modeled sensor response $\mathbf{r}_{\text{model}}$, given by Equation (3.7). Let $\mathbf{x} = [x_s \;\; y_s \;\; \theta \;\; p_1 \;\; p_2]^T$ be the vector of parameters to be estimated. The model parameter estimates are updated as follows:

$$\mathbf{x}_n = \mathbf{x}_{n-1} - \gamma \nabla E(\mathbf{x}_{n-1}) \tag{3.8}$$

where n is the iteration number,

$$\mathbf{e} = \mathbf{r}_{\text{measured}} - \mathbf{r}_{\text{model}}$$

$$E(\mathbf{x}) = \|\mathbf{e}\|^2 = \mathbf{e}^T\mathbf{e}$$

$$\nabla E(\mathbf{x}_{n-1}) = \frac{\partial E}{\partial \mathbf{x}}\bigg|_{\mathbf{x}=\mathbf{x}_{n-1}} = \left[\frac{\partial E}{\partial x_s} \;\; \frac{\partial E}{\partial y_s} \;\; \frac{\partial E}{\partial \theta} \;\; \frac{\partial E}{\partial p_1} \;\; \frac{\partial E}{\partial p_2}\right]^T$$

3.3.3 Extended Kalman Filter Algorithm

It is also possible to formulate the source localization problem as a parameter adaptive filtering problem using an EKF. First, an augmented state vector is defined $\bar{\mathbf{x}} = [\mathbf{x}^T \; r]^T = [x_s \;\; y_s \;\; \theta \;\; p_1 \;\; p_2 \;\; r]^T$. The state equation is

$$\bar{\mathbf{x}}_k = f(\bar{\mathbf{x}}_{k-1}) \tag{3.9}$$

$$\bar{\mathbf{x}}_k = \begin{bmatrix} x_{\mathrm{s}k} \\ y_{\mathrm{s}k} \\ \theta_k \\ p_{1k} \\ p_{2k} \\ r_k \end{bmatrix} = \underbrace{\begin{bmatrix} x_{\mathrm{s}k-1} \\ y_{\mathrm{s}k-1} \\ \theta_{k-1} \\ p_{1k-1} \\ p_{2k-1} \\ 0.95r_{k-1} + 0.05r_0(x_{\mathrm{s}k-1}, y_{\mathrm{s}k-1}, \theta_{k-1}, p_{1k-1}, p_{2k-1}, x_{k-1}, y_{k-1}) \end{bmatrix}}_{f} \tag{3.10}$$

The measured output is the sensor response; the output equation is

$$z_k = h(\bar{\mathbf{x}}_k) = [0\ 0\ 0\ 0\ 0\ 1]\ \bar{\mathbf{x}}_k = r_k \tag{3.11}$$

As before, the UAS operates in a cross-wind lawn mower pattern until a detection occurs, i.e., until a sampled concentration exceeds the sensor's threshold. At this point, the EKF provides an estimate of the source location and the UAS flies toward this estimated location in a zigzag pattern, continuing to sample along the way. If the sampled concentration ever falls below the threshold, the UAS returns to the lawn mower pattern. See the right branch of Figure 3.2.

The discrete time equations for predicting and updating the states ($\bar{\mathbf{x}} \in \mathbb{R}^{6\times 1}$) using the EKF algorithm are shown in Equation (3.12-3.16).

Prediction: The prediction step is based on a prior (or initial) state estimate $\hat{\bar{\mathbf{x}}}_{k-1|k-1}$ and a prior (or initial) error covariance $\mathbf{P}_{k-1|k-1} \in \mathbb{R}^{6\times 6}$ according to the following equations:

$$\hat{\bar{\mathbf{x}}}_{k|k-1} = f(\hat{\bar{\mathbf{x}}}_{k-1|k-1}) \tag{3.12}$$

$$\mathbf{P}_{k|k-1} = \mathbf{F}_{k-1}\mathbf{P}_{k-1|k-1}\mathbf{F}^T{}_{k-1} \tag{3.13}$$

where

$$\mathbf{F}_{k-1} = \left.\frac{\partial f}{\partial \bar{\mathbf{x}}}\right|_{\hat{\bar{\mathbf{x}}}_{k-1|k-1}}$$

Correction: The correction step uses the prediction plus the new data ($z_k \in \mathbb{R}^{1\times 1}$) from the current time step. The Kalman gain $\mathbf{k}_k \in \mathbb{R}^{6\times 1}$ is

$$\mathbf{k}_k = \mathbf{P}_{k|k-1}\mathbf{h}_k^T(\mathbf{h}_k\mathbf{P}_{k|k-1}\mathbf{h}_k^T)^{-1} \tag{3.14}$$

where $\mathbf{h}_k \in \mathbb{R}^{1\times 6}$ is

$$\mathbf{h}_k = \left.\frac{\partial h}{\partial \bar{\mathbf{x}}}\right|_{\hat{\bar{\mathbf{x}}}_{k|k-1}}$$

The posterior state estimate $\hat{\bar{\mathbf{x}}}_{k|k}$ and the posterior error covariance estimate $\mathbf{P}_{k|k}$ are updated according to the following equations:

$$\hat{\bar{\mathbf{x}}}_{k|k} = \hat{\bar{\mathbf{x}}}_{k|k-1} + \mathbf{k}_k(z_k - h(\hat{\bar{\mathbf{x}}}_{k|k-1})) \tag{3.15}$$

$$\mathbf{P}_{k|k} = (\mathbf{I} - \mathbf{k}_k\mathbf{h}_k)\mathbf{P}_{k|k-1} \tag{3.16}$$

3.4 Simulation Results

This section presents simulation results for the three source localization algorithms described in Section 3.3. The simulations were implemented in MATLAB, using wind field data generated using TurbSim.

3.4.1 Bayesian Estimation Simulation Results

In order to estimate the source location using BE techniques, a search area is defined from $x = 0$ m to $x = 550$ m and from $y = -250$ m to $y = 250$ m. We assume the UAS flies at 40 m altitude, moving from grid cell to cell according to the procedure indicated in the left branch

of Figure 3.2. The UAS orbits the center of a given grid cell for sufficient time to process a sample, after which the sampling device either fails to detect the contaminant or produces a measurement of the contaminant concentration. Initially, the search area has a uniform prior probability distribution. With every detection and concentration measurement, the posterior probability is updated. The grid cell with the highest probability, at any instant, is the one most likely to contain the source.

In the simulation, the aircraft starts searching from the "northeast" (top right) corner of the search area in Figure 3.4, moving south (with the wind coming from the west) and following a lawn mower pattern until a measurement exceeds a threshold value. Once a measurement exceeds the threshold value, the posterior probability at each grid cell is updated. The UAS is then commanded to fly to the point with the highest posterior probability.

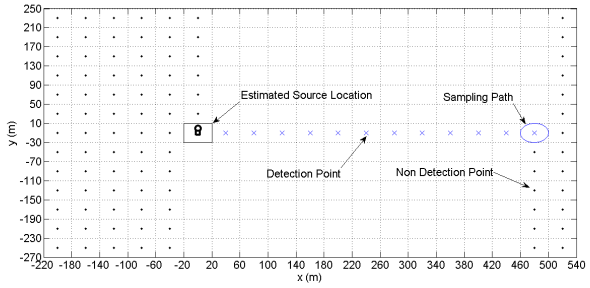

Figure 3.4: Estimation results using 40m x 40m grid cells.

Simulation results for the Bayesian source localization strategy are shown in Figures 3.4, 3.5, 3.6, and 3.7, using 40 m x 40 m grid cells with a threshold concentration of 10^{-5} particles/cm^3. Figure 3.4 shows the UAS's search path. The dots represent nondetections, and the x's represent detections. The thick open square is the center of the grid cell estimated to contain the source; the thick open circle marks the true source, which is always located at the origin. Figure 3.5(a) shows the initial probability distribution. With every detection the posterior probability is updated using Equation 3.4. Figure 3.5(c) shows the posterior probability after the first detection.

Figure 3.6 shows the prior, likelihood, and posterior probability distribution after the fifth

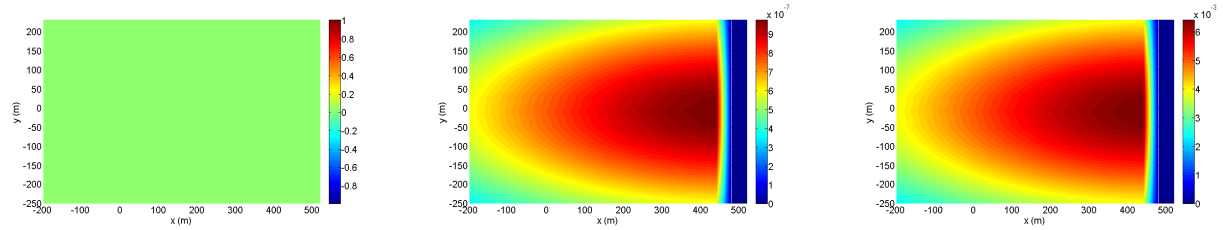

(a) Prior. (b) Likelihood. (c) Posterior.

Figure 3.5: Probability distribution after the first detection.

detection. With more detection points, certainty about the source location increases.

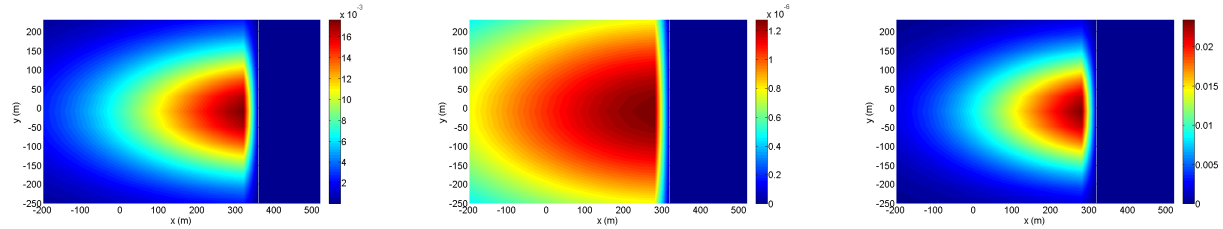

(a) Prior. (b) Likelihood. (c) Posterior.

Figure 3.6: Probability distribution after the fifth detection.

Figure 3.7 shows the prior, likelihood, and posterior probability distribution at the final detection point. The posterior probability is highest in a small region around the source and nearly zero elsewhere.

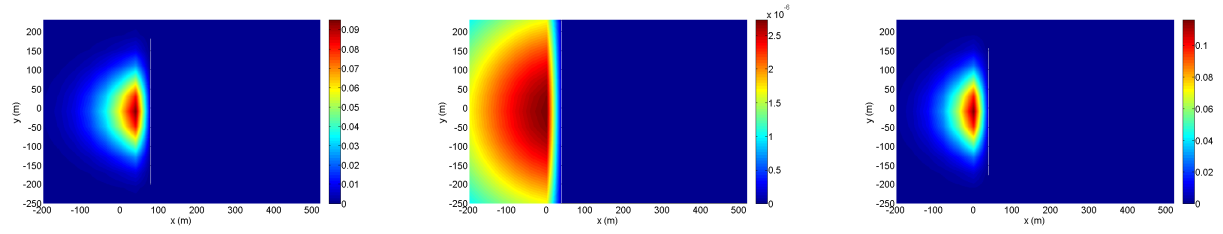

(a) Prior. (b) Likelihood. (c) Posterior.

Figure 3.7: Final probability distribution.

For comparison, Figure 3.8 shows the sequence of points at which the UAS obtains samples using a 70 m x 70 m grid and using a threshold value of $3\text{x}10^{-6}$ particles/cm^3. Figure 3.8(a) shows the UAS's path starting from the northeast corner of the search area, while Fig-

ure 3.8(b) shows the UAS's path starting from the southeast corner of the search area. The grid cell containing the source is located after having collected fewer samples, but the estimated source location is determined with less accuracy. This suggests that a variable grid size may be effective in balancing convergence rate with accuracy.

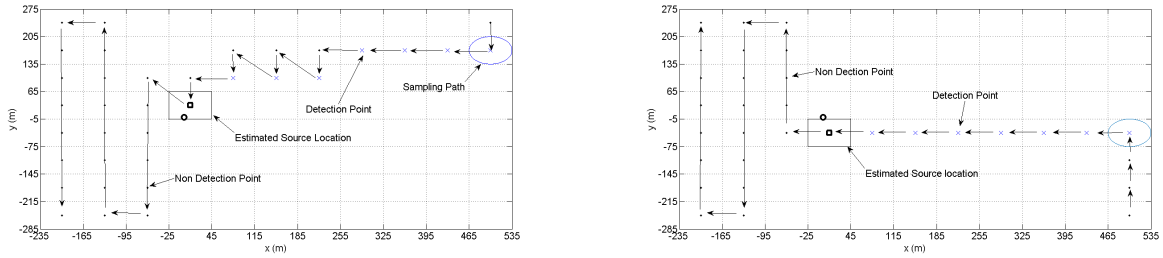

(a) Start searching from the northeast corner.

(b) Start searching from the southeast corner.

Figure 3.8: Estimation results using 70m x 70m grid cells.

3.4.2 Gradient Descent Simulation Results

This section shows the results of estimating the contaminant source location, applying the GD estimation algorithm described in Section 3.3.2. Concentration values generated using the method described in Section 3.2 are considered to be "true" measurements. (The simulated concentrations, in particles/m^3, are scaled by 10^{-2} to match the assumed sensitivity of the sensor and to provide sufficiently rich measurement data.) These measurements are then compared with predicted measurements based on the simplified plume model (3.5) using sensor models (3.6) and (3.7).

To estimate the source location using the GD method 3.8, the UAS was assumed to fly at a constant speed of 40 m/s in a lawn mower pattern along the course defined by the sequence of blue points, starting from the "northeast" (top right) point in Figure 3.9, retracing the pattern iteratively for 300 s and collecting one sample every second.

Two simulations were executed for different initial conditions. Figure 3.10 shows identification results for a hypothesized contaminant source with the following initial parameter

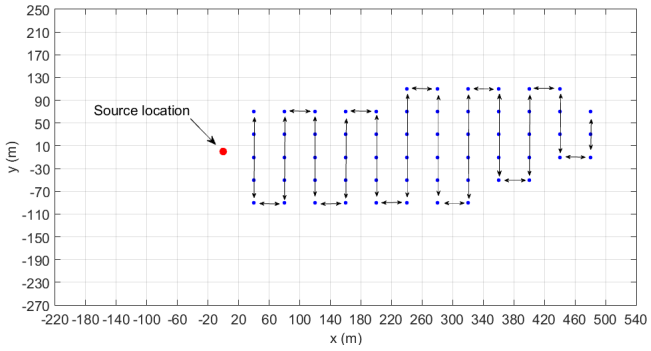

Figure 3.9: Sampling path.

values:

$$x_{s_i} = 30 \text{ m}, \quad y_{s_i} = 30 \text{ m}, \quad \theta_i = 185\ ^\circ, \quad p_{1_i} = 100 \text{ ml/m}^2, \quad p_{2_i} = 0.001 \text{ m}^{-1}, \quad \text{and} \quad \gamma = 0.01$$

The estimated sensor response roughly agrees with the measured sensor response as shown in Figure 3.10(a). The estimated source location converges to the actual source location, the estimation error in Figure 3.10(b) (i.e., the distance between the actual and estimated source location) is 37.8 m after 2×10^6 iterations. The estimated source location is at $x = 25.5$ m and $y = 27.9$ m, while the actual source location is at $x = 0$ m and $y = 0$ m. The final estimated parameter values are

$$x_{s_f} = 25.5 \text{ m}, \quad y_{s_f} = 27.9 \text{ m}, \quad \theta_f = 182\ ^\circ, \quad p_{1_f} = 98.2 \text{ ml/m}^2, \quad \text{and} \quad p_{2_f} = 0.03 \text{ m}^{-1}$$

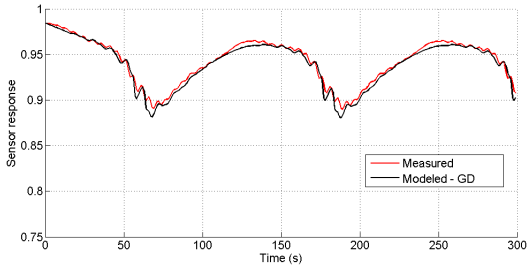

(a) Curve fit of the sensor response model.

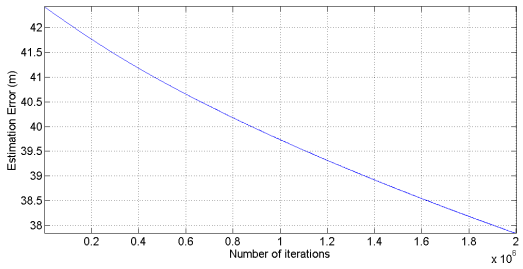

(b) Estimation error.

Figure 3.10: Result of off-line GD estimation of the contaminant source location.

Figure 3.11(a) shows the contaminant distribution, as simulated using the procedure described in Section 3.2.2, while Figure 3.11(b) shows the estimated contaminant distribution obtained using the GD method with the plume model in Equation 3.5. The difference between the "true" plume distribution and the estimated plume distribution is caused by the relative simplicity of the 5-parameter plume model, which cannot capture a complicated, three-dimensional advection and diffusion process.

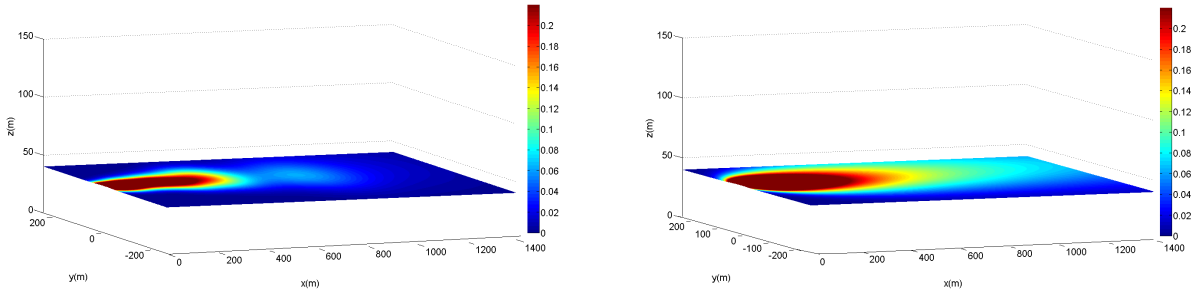

(a) Plume distribution.

(b) Estimated plume distribution using GD.

Figure 3.11: True and estimated contaminant concentration (in particles/m^3) at 40 m altitude.

Figure 3.12 shows results for a hypothesized contaminant source with the following initial parameter values:

$$x_{s_i} = 50 \text{ m}, \quad y_{s_i} = 50 \text{ m}, \quad \theta_i = 185\ ^\circ, \quad p_{1_i} = 100 \text{ ml/m}^2, \quad p_{2_i} = 0.1 \text{ m}^{-1}, \quad \text{and} \quad \gamma = 0.01$$

The estimated sensor response roughly agrees with the measured sensor response as shown in Figure 3.12(a). The estimation error in Figure 3.12(b), is 95.5 m after 2×10^6 iterations. The estimated source location is at $(x, y) = (76.8, 66.6)$ m, while the actual source location is $(x, y) = (0, 0)$ m, indicating that the GD algorithm is unable to accurately estimate the source location. The final estimated parameter values are

$$x_{s_f} = 76.8 \text{ m}, \quad y_{s_f} = 66.6 \text{ m}, \quad \theta_f = 167\ ^\circ, \quad p_{1_f} = 105.9 \text{ ml/m}^2, \quad \text{and} \quad p_{2_f} = 0.05 \text{ m}^{-1}$$

In conclusion, estimating the contaminant source location using the GD algorithm depends

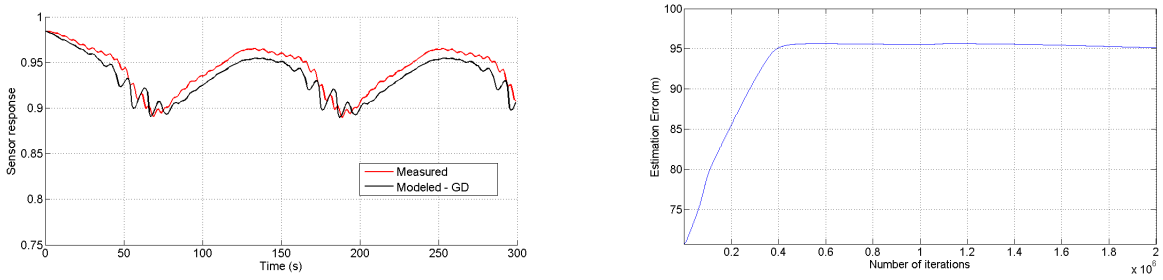

(a) Curve fitting of the sensor response model.

(b) Estimation error.

Figure 3.12: Off-line result of estimating the contaminant source location using the GD method.

on the choice of the initial parameter values, on the step size, and on the accuracy of the plume dispersion model used to model the contaminant concentration. The algorithm may settle into a locally optimal solution that is far from the true source location.

3.4.3 Extended Kalman Filter Simulation Results

To estimate the source location using the EKF algorithm (Equation (3.12-3.16)), the UAS is assumed to fly at a constant speed of 40 m/s, following a lawn mower pattern until the plume is detected (when the concentration exceeds 0.1 particles/m^3). Estimation of the source location starts after the plume is detected. Specifically, the UAS flies toward the estimated source in a zigzag pattern (EKF phase), at angles that are alternately $\pm 60°$ from the direction to the estimated source location, as in [1]. The sampling interval is 1 s and the estimated direction to the source is updated every 8 s.

Two simulations were executed for different initial conditions. Figure 3.13 shows the results obtained using the following initial parameters:

$$x_{s_i} = 300\text{m}, y_{s_i} = 60\text{m}, \theta_i = 185°, p_{1_i} = 300\text{ml/m}^2, p_{2_i} = 0.03\text{m}^{-1}, r_i = 0.98\text{m}^{-1}, \text{and}\, \mathbf{P}_i = 5\mathbf{I}$$

Figure 3.13(a) shows the UAS's path toward the estimated source location. The thick open square indicates the estimated source location, the thick open circle indicates the actual

source location (at the origin), and the large points represent the UASs location at 1 s intervals. The estimation error (i.e., the distance between the actual and estimated source locations) is 32 m as shown in Figure 3.13(b). Figure 3.14 shows the contaminant distribution generated as described in Section 3.2.2 and the distribution indicated by the final parameter values from the EKF algorithm. Note the disparity between the distribution generated by the EKF algorithm and that generated using the GD method discussed in Section 3.3.2. The relatively uniform concentration field in the neighborhood of the actual source suggests that accurate source localization using the EKF approach may be challenging.

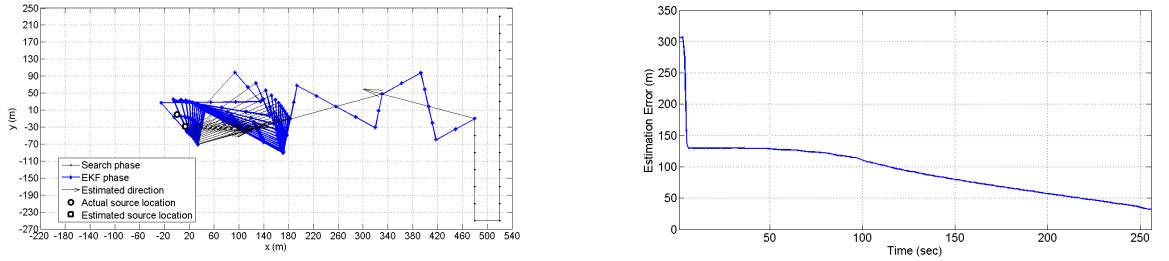

(a) UAS path.

(b) Estimation error after the contaminant detection.

Figure 3.13: On-line result of estimating the contaminant source location using EKF.

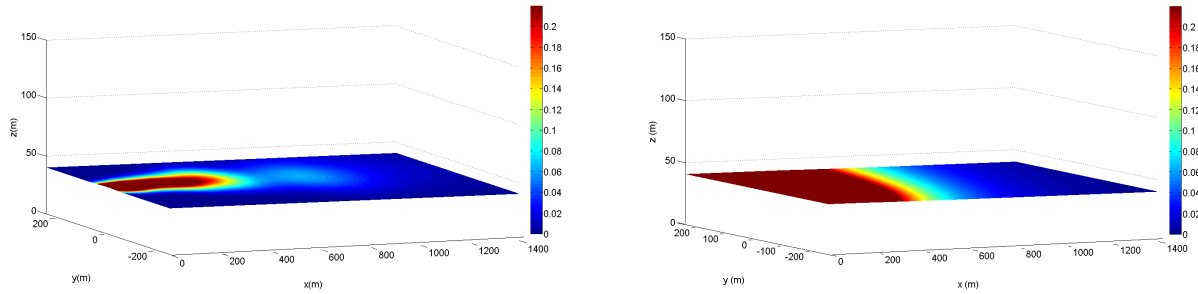

(a) Simulated plume distribution in particles/m^3.

(b) Estimated plume distribution in particles/m^3 using EKF.

Figure 3.14: Contaminant plume distribution at 40 m altitude.

Figure 3.15 shows the results of the EKF localization algorithm using the following initial parameter values:

$$x_{s_i} = 10 \text{ m}, y_{s_i} = 10\text{m}, \theta_i = 185^\circ, p_{1_i} = 70\text{ml/m}^2, p_{2_i} = 0.20\text{m}^{-1}, r_i = 0.98\text{m}^{-1}, \text{and}\, \mathbf{P}_i = 10\mathbf{I}$$

Figure 3.15(a) shows the UAS's path toward the estimated source location. The thick open square indicates the estimated source location, and the thick open circle indicates the actual source location. The estimation error for this case is 177 m, as shown in Figure 3.15(b). Here, the EKF algorithm fails to accurately estimate the source location.

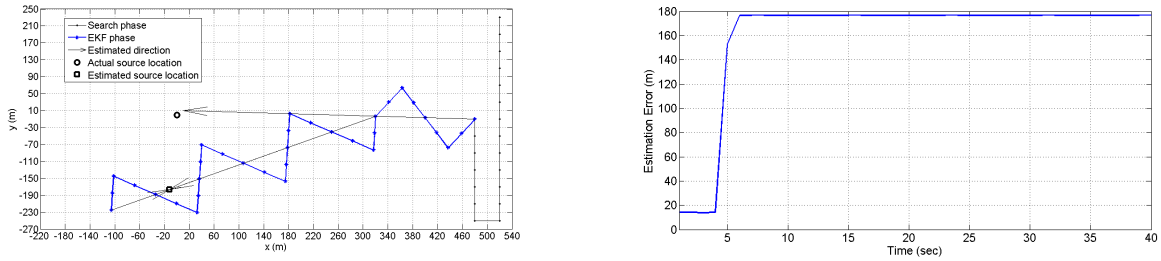

(a) UAS path. (b) Estimation error after the contaminant detection.

Figure 3.15: On-line result of estimating the contaminant source location using EKF.

Estimation of the source location using the extended Kalman filter algorithm is affected by the choice of the initial conditions, i.e., the initial states and the initial covariance matrix. An EKF can be difficult to tune and unreliable for nonlinear systems, as in this parameter adaptive filtering application [88].

In conclusion, estimates of the contaminant source location using the GD algorithm or the EKF are affected by the choice of the initial conditions and by the contaminant plume dispersion model. Alternatively, the BE algorithm requires minimal modeling assumptions, and simulation results suggest that the BE algorithm is an effective strategy for estimating the source location.

Consequently, an experimental investigation based on real flow conditions was conducted to estimate the source location of the aerosol (soot), that can be attributed to traffic, using a Bayesian estimation algorithm. Section 3.5 presents the field experimental setup and the results for estimating the source location (correlated with traffic flow) of an airborne contaminant (soot).

3.5 Aerosol Localization: Field Experiment 1

Aerosols play a crucial role in determining the radiation amount to the earth's atmosphere. To investigate the spatial relationship between air quality and traffic flow patterns, an experimental investigation based on real flow conditions was conducted to identify the source location (correlated with traffic flow) of an airborne contaminant (soot, i.e., attributed to traffic), using a Bayesian estimation algorithm. The experimental setup is shown in Section 3.5.1, and the estimation results is shown in Section 3.5.2.

3.5.1 Experimental Setup

A compact light detection and ranging (LiDAR), shown in Figure 3.16, is a system that provides aerosols vertical profile [89]. LiDAR system consists of a laser transmitter, a receiver, and a data acquisition system. The laser transmitter emits a pulse of light to the atmosphere. The light pulses encounter aerosols or particulate matter, that may absorb or scatter and reflect the light back to the ground. A telescope focused at the same atmospheric volume as the transmitted laser pulse collects the backscattered light and then sends it back to the receiver. The received signals are processed and averaged before storing as aerosol profile resolutions. Once the data is stored, the signal retrieval is achieved to obtain the optical parameters of the aerosol [90]. Different ratio parameters including lidar ratio and color ratio are retrieved from collected data. The aerosol ratio parameters are known to vary with aerosol type, size, and shape [91].

In the experiment, measurements were collected in the vicinity of the Old Dominion University (ODU) campus at different locations, to analyze the distribution of aerosols (soot) with variations in traffic levels, which will allow the investigation of the spatial relationships between air quality and traffic flow patterns. LiDAR was employed to collect aerosol data in the atmosphere at four sites shown in Figure 3.17, and marked with stars. Data were col-

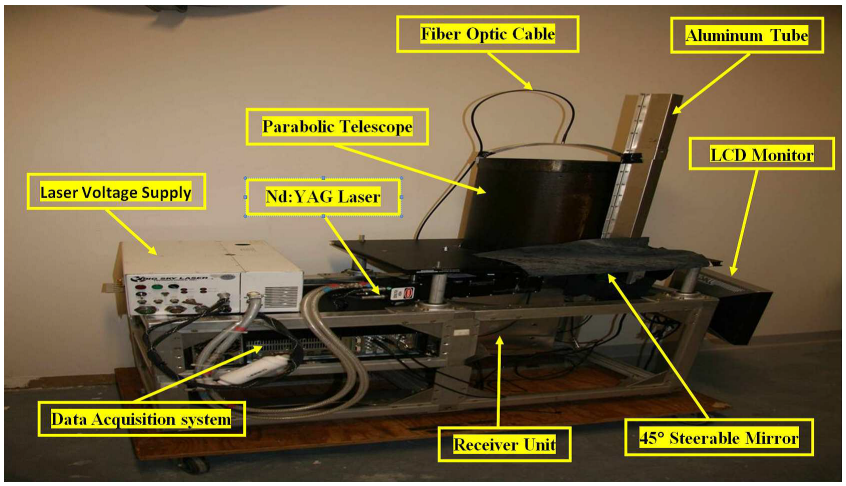

Figure 3.16: Lidar in vision lab at Old Dominion University.

lected at Hampton garage at 9 am for 70 minutes, at 43 st. garage at 11 am for 73 minutes, at 49 st. garage at 1 pm for 89 minutes, and at the management building at 3 pm for 90 minutes, on August 2016.

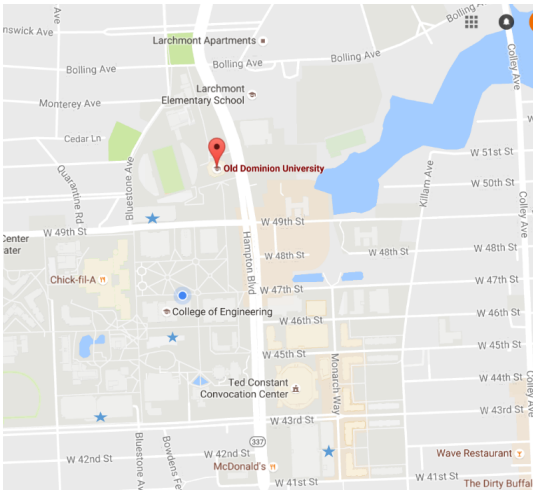

Figure 3.17: Measurements locations, Google maps.

Backscattering color ratio (BCR) and lidar ratio (LR) were retrieved as the optical parameters that encode the optical characteristics of the aerosols, through inversion solutions for lidar signals [92]. BCR is inversely related to aerosol particle sizes, where lower value implies large particles and higher value implies small particles [93]. LR depends on the size distri-

bution, shape and composition of the aerosols, where low LR value implies coarse particles and high LR value implies small mode particles [94].

3.5.2 Experimental Results

This section presents the measurements at the four sites and the results for estimating the soot source location, based on LR and BCR values. Existence of soot at certain point is claimed, if the BCR value is between $1.26 - 1.54$ and the LR value is between $60 - 65$, simultaneously [89], these values indicate the existence (i.e., exist (1) or not (0)) of soot, not the actual concentration.

3.5.2.1 LR Measurements

Figure 3.18 shows the locations where soot was detected at the four sites, LR value between $60 - 65$ means existence [92].

To generate a concentration field over the search area, first we calculated the normalized frequencies of detections (vertically, over height) at the four sites as shown in Figure 3.19. Then, we calculated the average values at the four sites, the average values are $0.0111, 0.0078, 0.0123, 0.0113$, respectively. A concentration field over the search area was generated by interpolating these average values, as shown in Figure 3.20.

3.5.2.2 BCR Measurements

Figure 3.21 shows the locations where soot was detected at the four sites, BCR value ranges between $1.26 - 1.54$ means existence.

To generate a concentration field over the search area, first we calculated the normalized frequencies of detection (vertically, over height) at the four sites as shown in Figure 3.22. Then, we calculated the average values at the four sites, the average values are

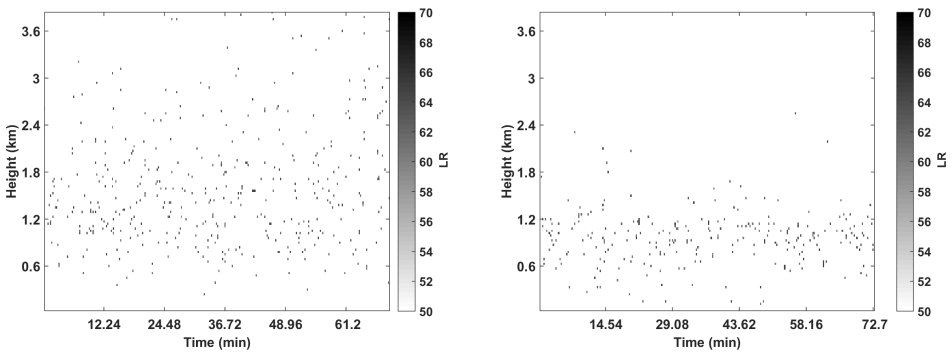

(a) Hampton garage. (b) 43 street garage.

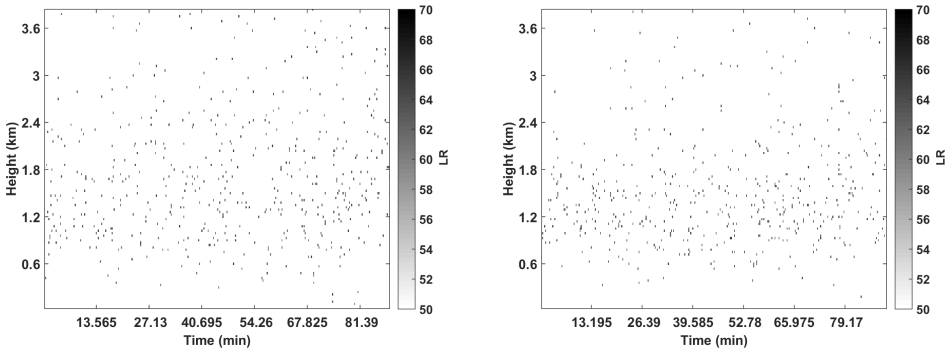

(c) 49 street garage. (d) Management.

Figure 3.18: Soot locations based on LR values.

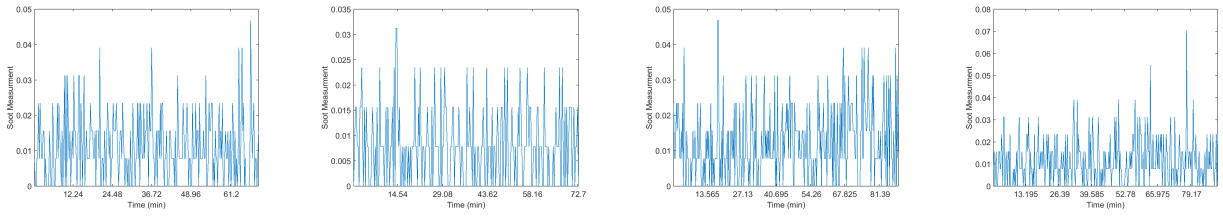

(a) Hampton garage. (b) 43 street garage. (c) 49 street garage. (d) Management.

Figure 3.19: Normalized frequency of detection for soot.

$0.0109, 0.0133, 0.0114, 0.0112$, respectively. A concentration field over the search area was generated by interpolating these average values, as shown in Figure 3.23.

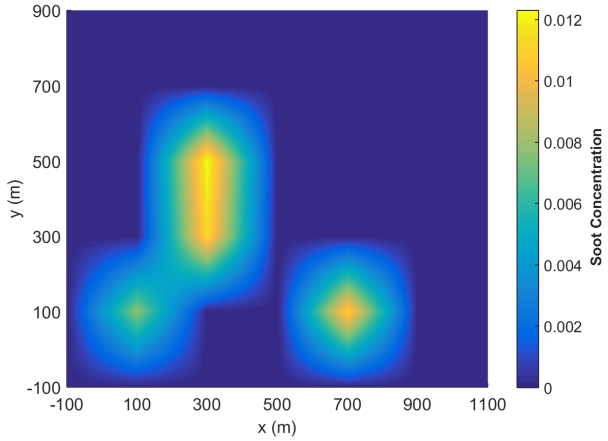

Figure 3.20: LR soot concentration.

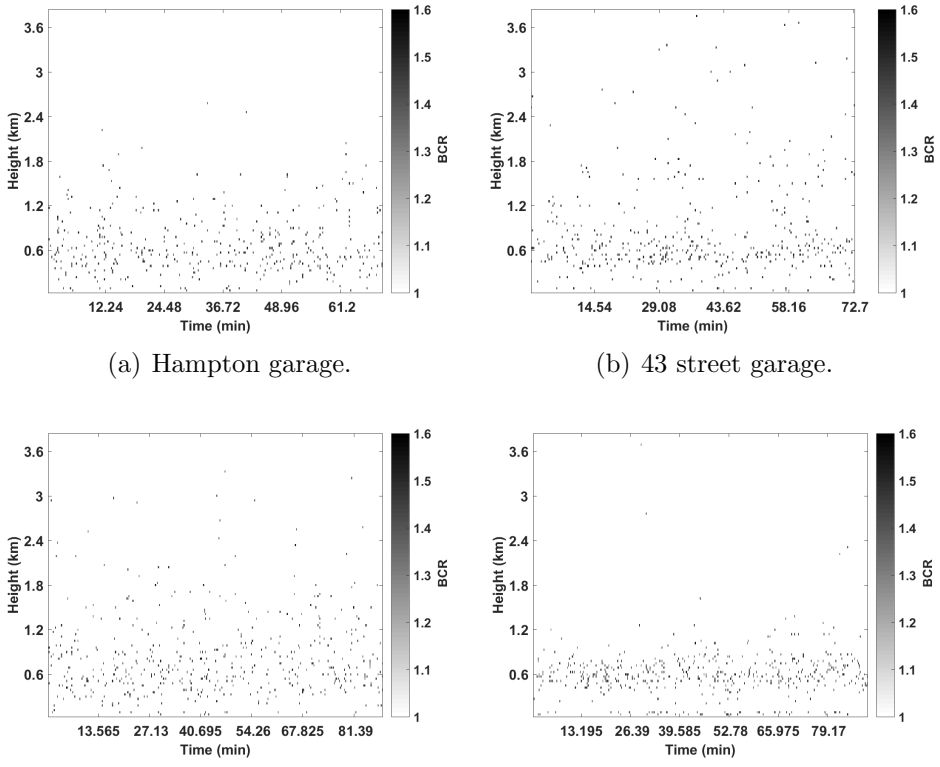

(a) Hampton garage.

(b) 43 street garage.

(c) 49 street garage.

(d) Management.

Figure 3.21: Soot locations based on BCR values.

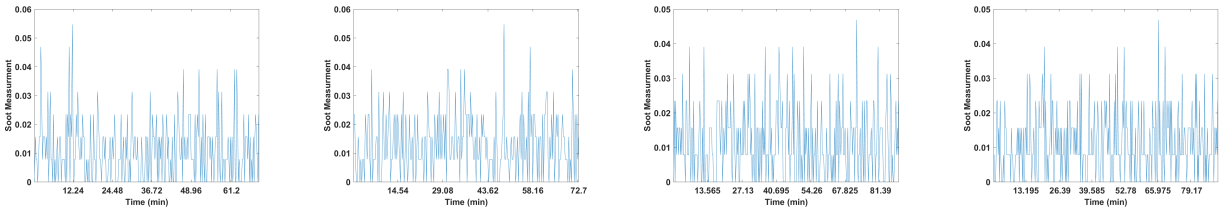

(a) Hampton garage. (b) 43 street garage. (c) 49 street garage. (d) Management.

Figure 3.22: Normalized frequency of detection for soot.

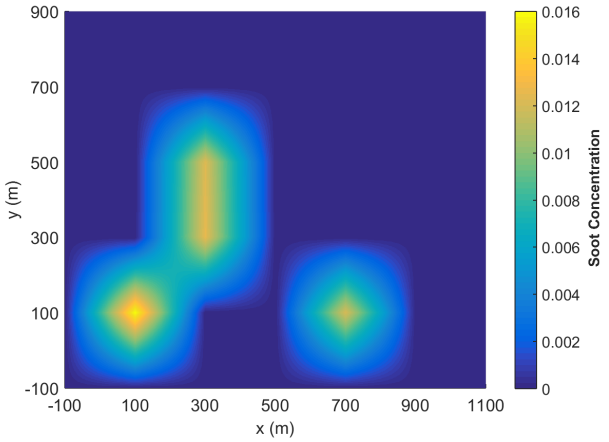

Figure 3.23: BCR soot concentration.

3.5.2.3 Estimation Results

The Bayesian estimation algorithm was employed to estimate the source location of the soot in the study area. Existence of soot at certain location is claimed, if the BCR concentration is $\geqslant 0.01$ and the LR concentration is $\geqslant 0.007$, simultaneously. The threshold values were chosen to be the minimum average concentration at the four locations. Simulation results for estimating the soot location using the Bayesian source localization strategy are shown in Figures [3.24-3.26], using 200 m x 200 m grid cells.

Initially, sample points are selected by simply "mowing the lawn" in the cross-wind direction within a bounded search area as shown in Figure 3.24, where the mean wind is from the north during the data collections. The search pattern for the simulations described here begins at the bottom left. If the concentration does not exceed the two threshold values simultaneously,

continues to the next grid cell in the lawn mower pattern. If the concentration exceeds the threshold values, update the posterior probability for all cells in the grid and then directed to the grid cell with the highest posterior probability.

Figure 3.24 shows the results for estimating soot location, following a predefined search pattern, and visiting a sequence of sample points. The cross points represent detections, black small circles represent non-detections, the four bigger red circles mark the measurements locations, diamond marker is the center of the grid cell estimated to contain the source. The open square represents the actual intersection location (Hampton Blvd with W49th St, Figure 3.17.

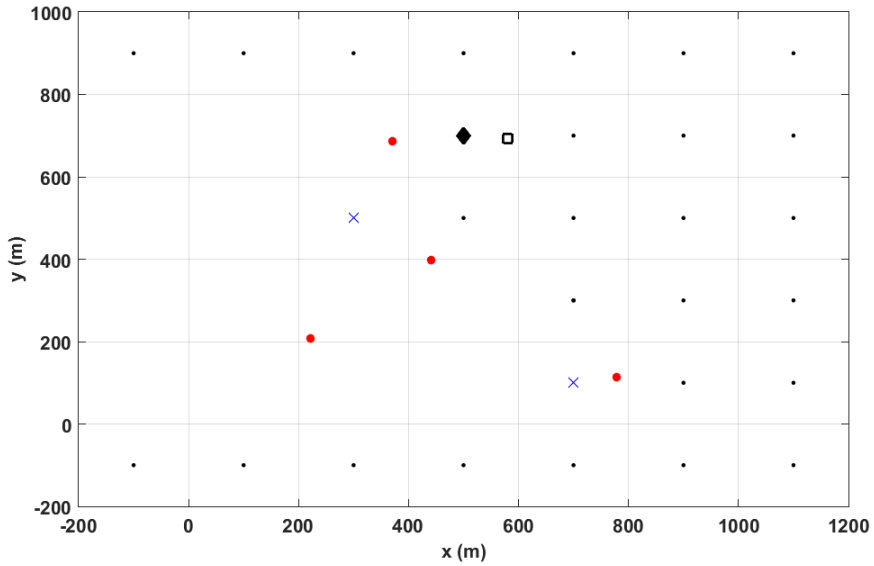

Figure 3.24: Estimation results.

Figure 3.25 shows the probability distribution after the first detection, with every detection the probability distributions are updated.

Figure 3.26 shows the prior, likelihood, and posterior probability distribution at the final detection point. The posterior probability is highest in the region around the estimated source location.

The simulation shows that the source of the soot over the grid of study is located near

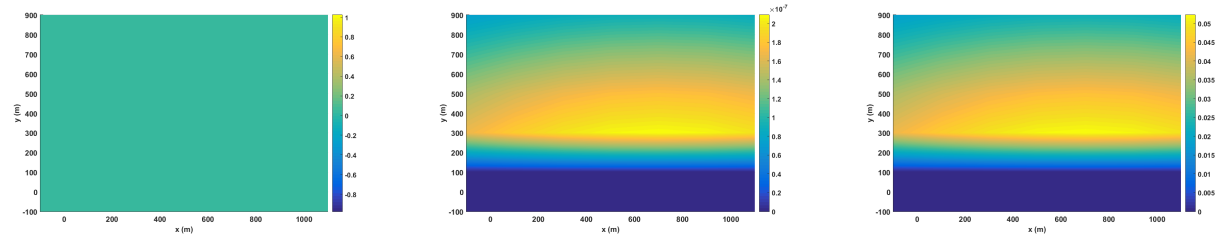

(a) Prior. (b) Likelihood. (c) Posterior.

Figure 3.25: Probability distribution after the first detection.

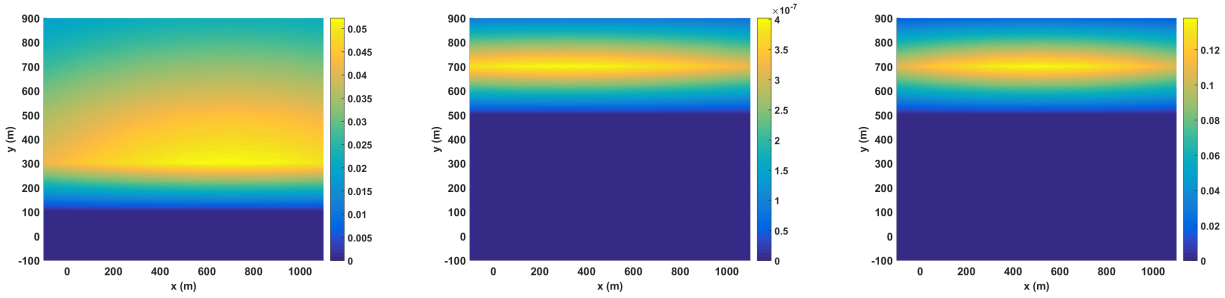

(a) Prior. (b) Likelihood. (c) Posterior.

Figure 3.26: Final Probability distribution.

the point of intersection of Hampton Blvd and 49th street, the estimated source location is indicated by the diamond marker in Figure 3.24. A close observation of traffic pattern in the search area suggests that the source of soot at this point make sense because it is the main traffic light in the vicinity of ODU campus, and the diesel trucks most likely stop by it more than other parts of the study area, which demonstrates that air quality is correlated with traffic flows and congestion caused by signalized intersections.

3.6 Aerosol Localization: Field Experiment 2

3.6.1 Experimental Setup

In this experiment, measurements were collected in the vicinity of the Old Dominion University (ODU) campus at six different locations as shown in Figure 3.27. The LiDAR was

mounted on a truck and the data were collected on July, 2017, to analyze the distribution of aerosols (soot) with variations in traffic levels.

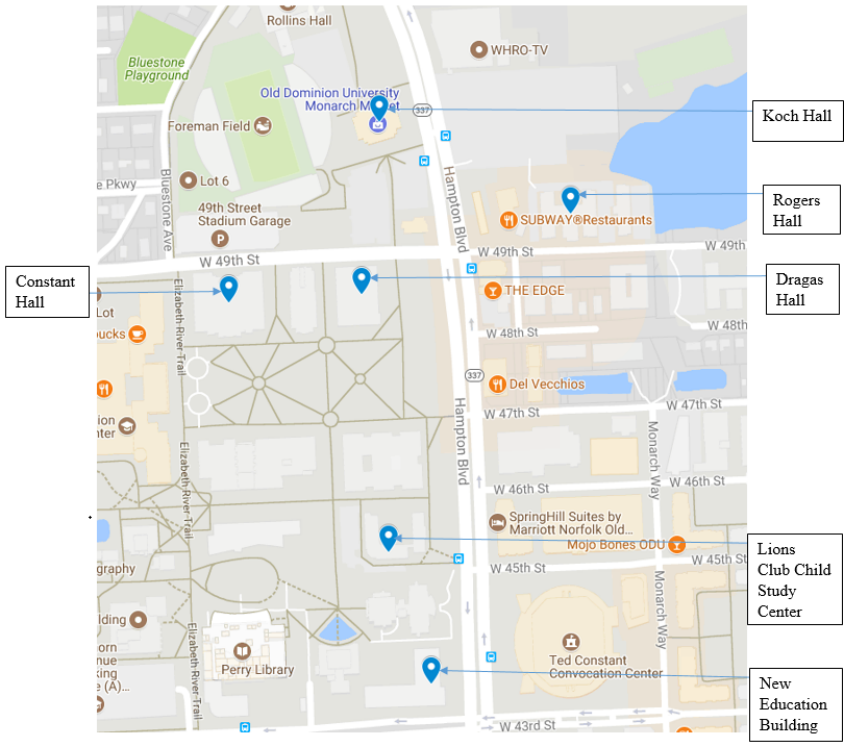

Figure 3.27: Measurements Locations, Google maps.

3.6.2 Experimental Results

This section presents the measurements at the six sites and the results for estimating the soot source location, based on LR and BCR values. Existence of soot at certain point is claimed, if the BCR value is between $1.26 - 1.54$ and the LR value is between $60 - 65$, simultaneously [89], these values indicate the existence (i.e., exist (1) or not (0)) of soot, not the actual concentration.

3.6.2.1 LR Measurements

Figure 3.28 shows the locations where soot was detected at the six measurements locations, where LR values for soot ranges between $60 - 65$.

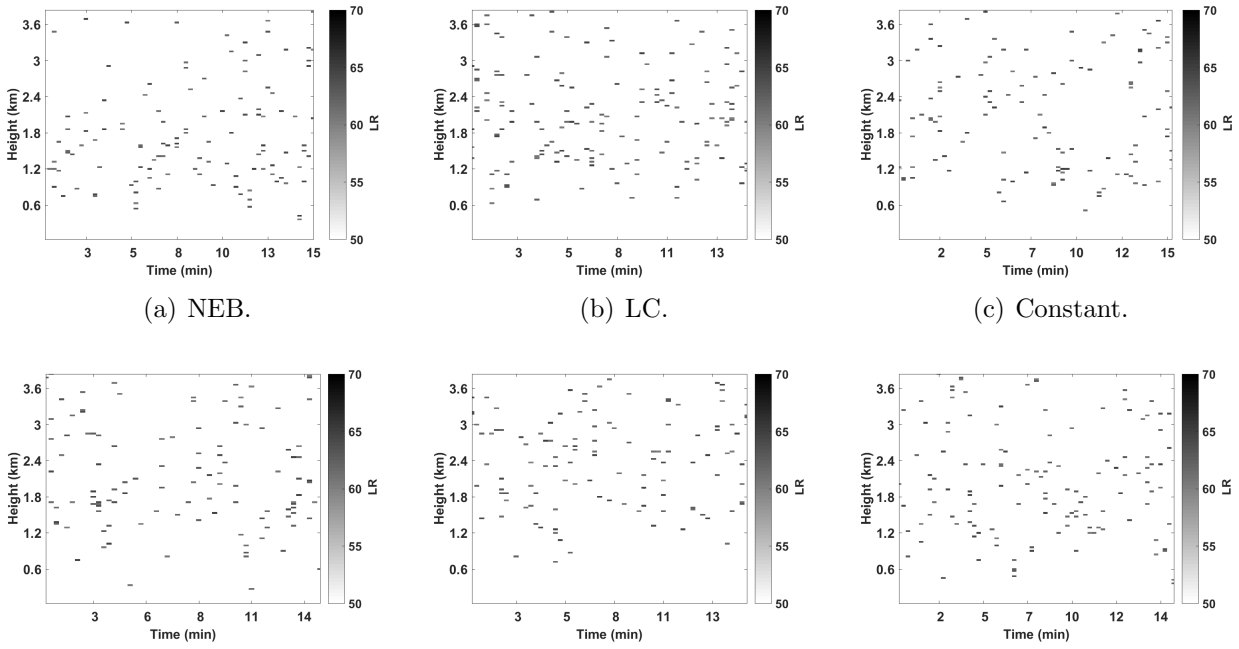

(a) NEB. (b) LC. (c) Constant.

(d) Dragras. (e) Koch. (f) Rogers.

Figure 3.28: Lidar ratios of expected particular matters of interest (soot).

To generate a concentration field over the search area, first we calculated the normalized frequencies of detections (vertically, over height) at the six sites as shown in Figure 3.29 Then, we calculated the average values at the six sites, the average values are $0.0152, 0.0208, 0.0145, 0.0164, 0.0158, 0.0159$, respectively. A concentration field over the search area was generated by interpolating these average values, as shown in Figure 3.30, using 200 m x 200 m grid cells..

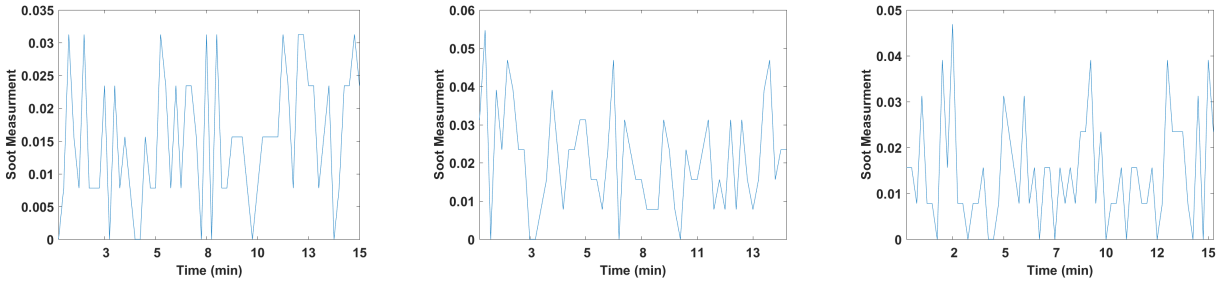

(a) NEB. (b) LC. (c) Constant.

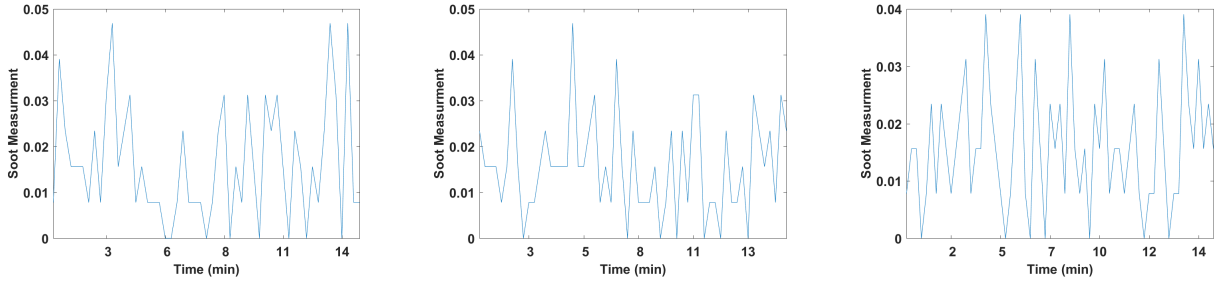

(d) Dragras. (e) Koch. (f) Rogers.

Figure 3.29: LR Normalized frequency measurements of soot.

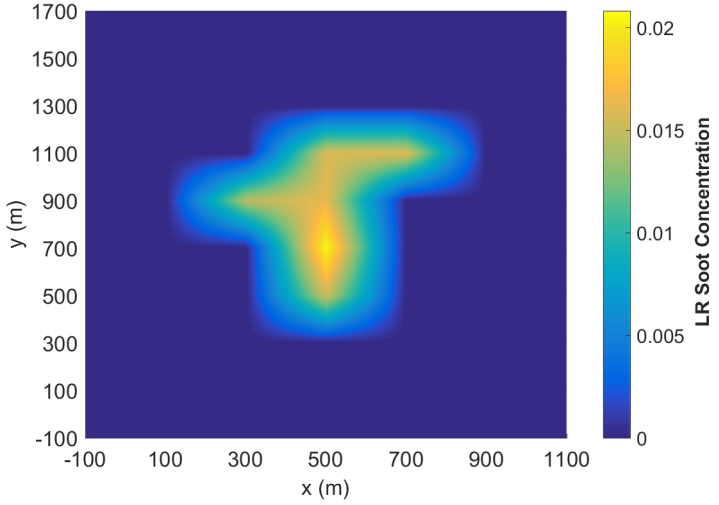

Figure 3.30: LR soot concentration.

3.6.2.2 BCR Measurements

Figure 3.31 shows the locations where soot was detected at the six measurements locations, where BCR values for Soot ranges between $1.26 - 1.54$ means existence.

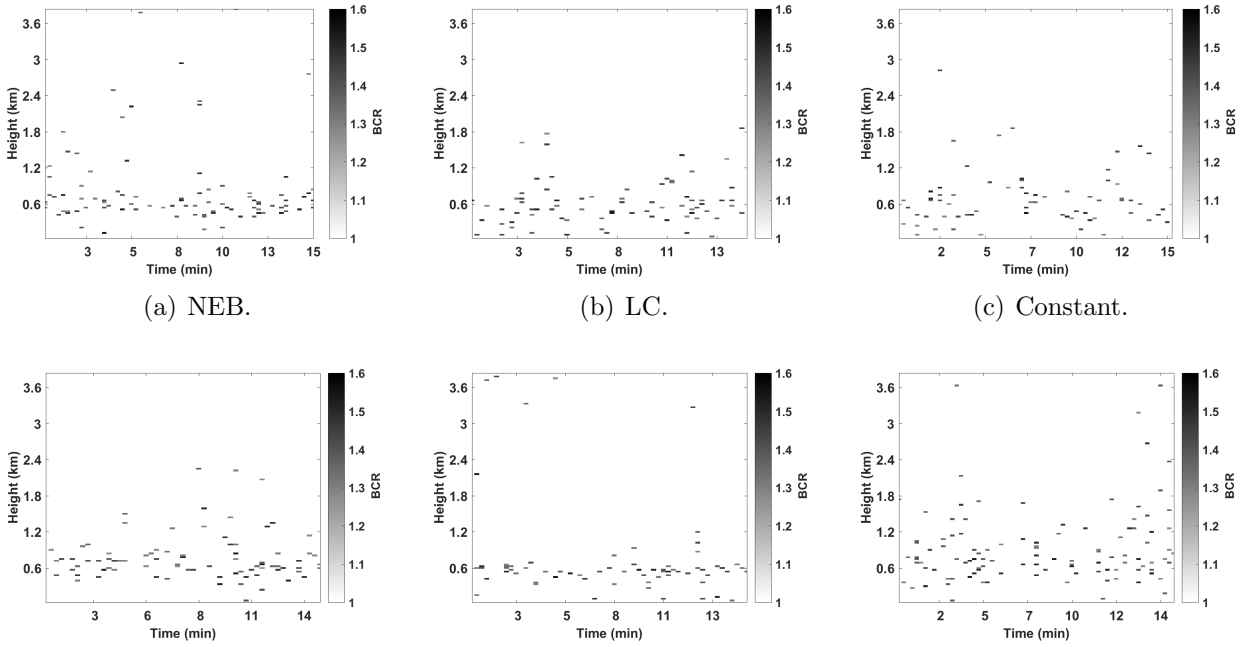

(a) NEB. (b) LC. (c) Constant.

(d) Dragras. (e) Koch. (f) Rogers.

Figure 3.31: Color ratios of expected particular matters of interest (Soot).

To generate a concentration field over the search area, first we calculated the normalized frequencies of detection (vertically, over height) at the six sites as shown in Figure 3.32 Then, we calculated the average values at the four sites, the average values are $0.0132, 0.0085, 0.0109, 0.0102, 0.0093, 0.0131$, respectively. A concentration field over the search area was generated by interpolating these average values, as shown in Figure 3.33, using 200 m x 200 m grid cells..

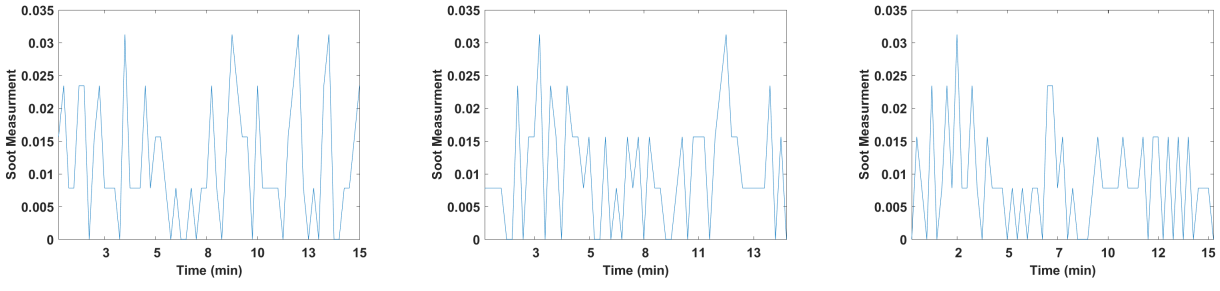

(a) NEB. (b) LC. (c) Constant.

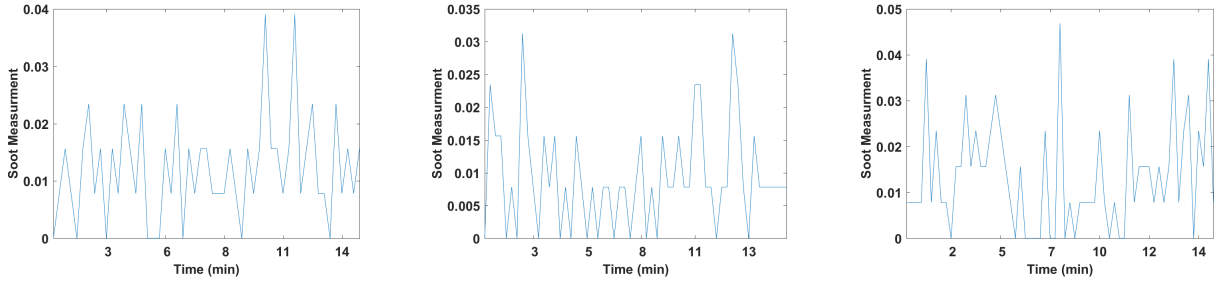

(d) Dragras. (e) Koch. (f) Rogers.

Figure 3.32: BCR Normalized frequency measurements of soot.

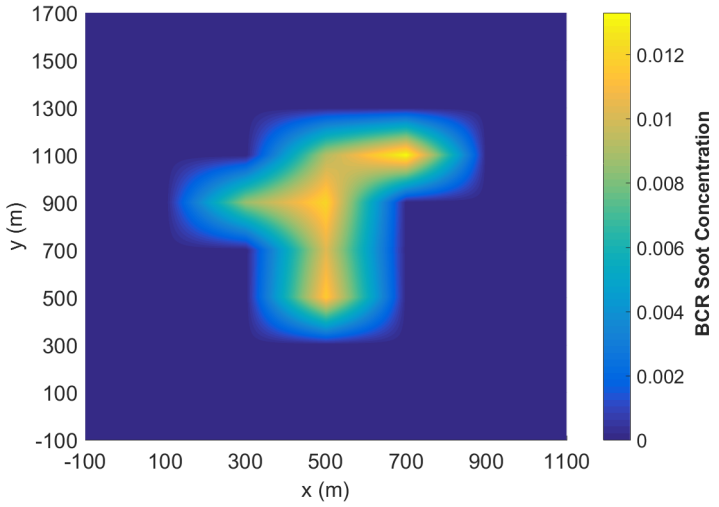

Figure 3.33: Interpolated BCR soot concentration.

3.6.2.3 Estimation Results

Simulation results for estimating the soot source location using the Bayesian source localization strategy are shown in Figure 3.34, with a threshold concentration of 0.008 for BCR measurements and 0.01 for LR measurements. The threshold values were chosen to be the minimum average normalized frequency at the six locations.

Figure 3.34 shows the results for estimating soot location, following a predefined search pattern, visiting a sequence of sample points. Initially, sample points are selected by simply "mowing the lawn" in the cross-wind direction within a bounded search area, the mean wind is from the north. The search pattern for the simulations described here begins at the bottom left. If the concentration does not exceed the threshold values simultaneously, continues to the next grid cell in the lawn mower pattern. If the concentration exceeds the threshold values, the measured concentration is used to update the posterior probability for all cells in the grid and the then directed to the grid cell with the highest probability of containing the source. The map is updated after each detection and the estimated source location is defined as the point at which posterior probability is maximum. The cross points represent detections, black small circles represent non-detections, the bigger red circles mark the measurements locations, diamond marker is the center of the grid cell estimated to contain the source. The open squares represent the intersections locations (i.e., Hampton Blvd with W49th St, and Hampton Blvd with Bolling Ave, shown in Figure 3.35).

Figure 3.36 shows the prior, likelihood, and posterior probability distribution at the final detection point. The posterior probability is highest in the region around the estimated source location.

The simulation results show that the source of the soot over the grid of study is located on Hampton Blvd, near the point of intersection of Hampton Blvd and Bolling Ave, the estimated source location is indicated by the diamond marker in Figure 3.34, which demonstrates that air quality is correlated with traffic flows and congestion caused by signalized

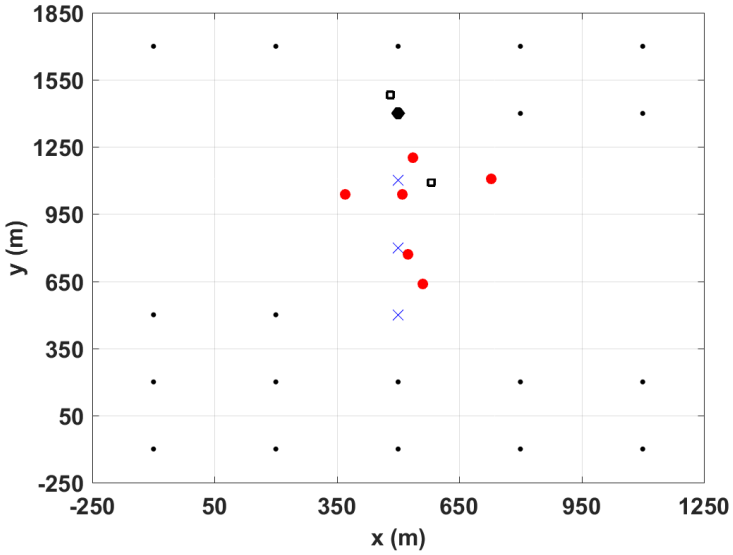

Figure 3.34: Estimation results.

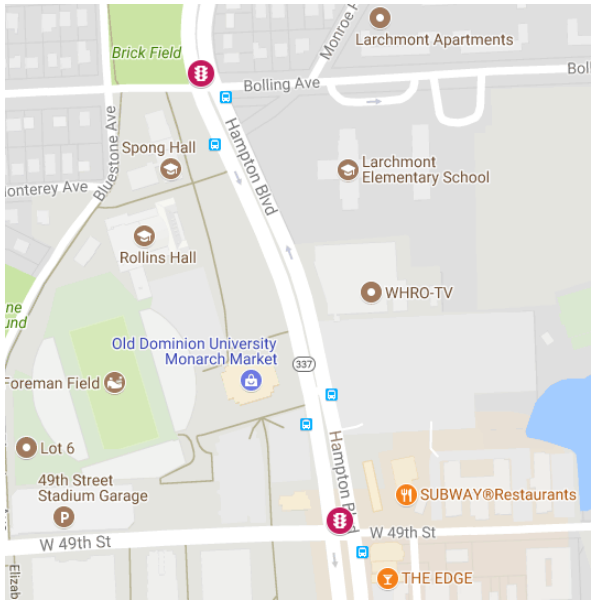

Figure 3.35: Intersections Locations, Google maps.

intersections.

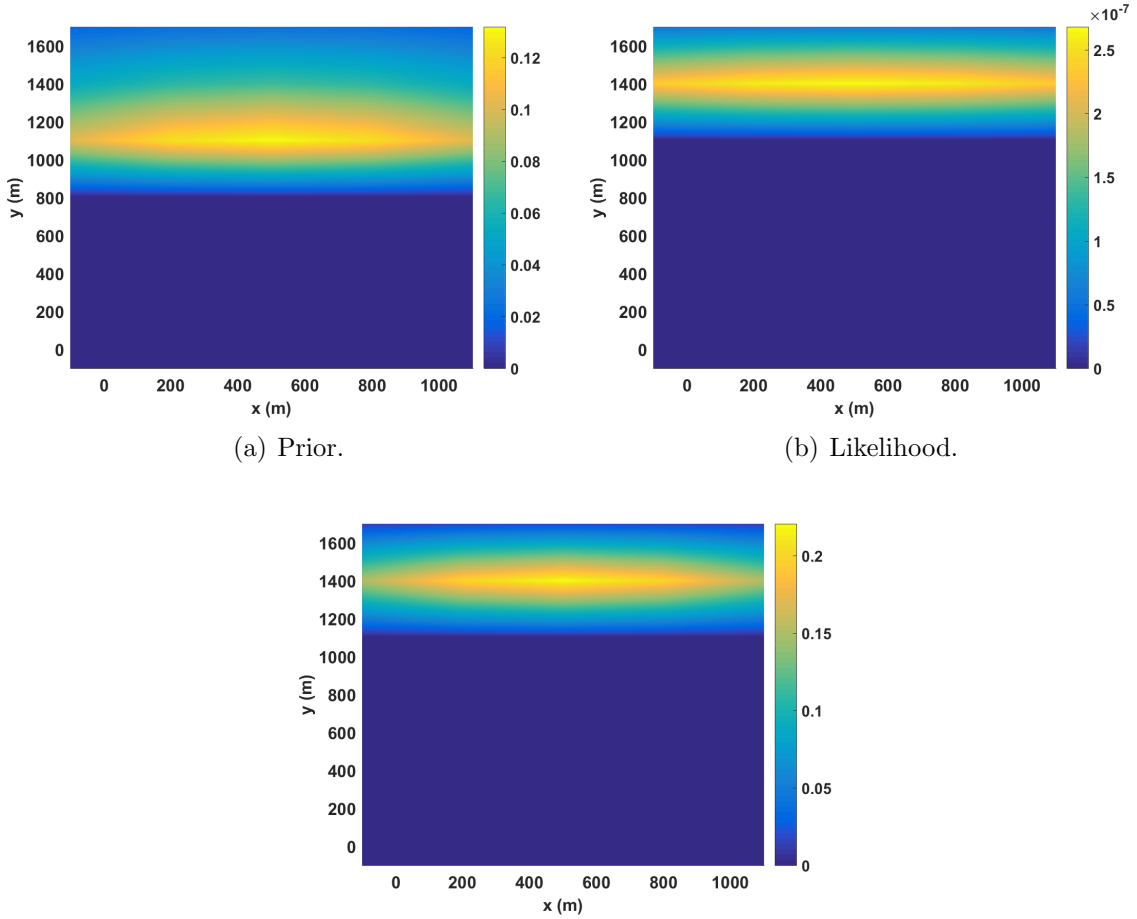

(a) Prior.

(b) Likelihood.

(c) Posterior.

Figure 3.36: Final Probability distribution.

3.7 Summary

To investigate the spatial relationship between air quality and traffic flow patterns, simulation studies were conducted to demonstrate relative strengths and weaknesses of source localization strategies, these simulations were preliminary steps toward the planned experiment. In simulations, the problem of localizing the source of a contaminant being released into the atmosphere was formulated and addressed using three estimation algorithms. The plume, which served as the basis for comparison, was generated using the turbulent atmospheric flow simulation TurbSim to propagate a contaminant plume employing an atmospheric dispersion

model proposed in the literature. The location of the plumes source was estimated using three algorithms: a recursive Bayesian estimation algorithm, a gradient descent algorithm, and an extended Kalman filter algorithm.

Three simulations were presented using BE. In this approach, the source strength and the wind statistics are not needed. The localization accuracy is determined in part by the cell size within the underlying occupancy grid. Larger cells result in lower accuracy but quicker convergence, illustrating the trade-off between search efficiency and estimation accuracy. The estimation results using the GD algorithm are affected by the choice of the initial parameters and the step size. The GD algorithm is capable of finding a local optimum solution, but it is not guaranteed to find the best possible solution in the search space (the global optimum). The results of estimating the model parameters using the curve-fitting method are dependent on the initial parameters. In addition, the convergence rate is dependent on the step size; in some cases, the estimate may diverge. Fitting the model sensor response curve to the measured response curve is difficult when slight differences are observed in the sensor responses at different locations. The gradient descent approach does not modify the UAS's motion based on the parameter estimates; the UASs motion is completely prescribed in advance. Thus, the method may fail if it starts in a region where the sensor data are too noisy or too weak. The estimation results using the EKF algorithm are affected by the choice of the initial states and the initial covariance matrix. The EKF algorithm is computationally efficient; however, it is difficult to tune and only reliable for systems that are almost linear. If the initial estimate of the state is wrong, or if the process is modeled inaccurately, the EKF algorithm may diverge. Estimates of the contaminant source location using the GD algorithm or the EKF are affected by the choice of the initial conditions and by the contaminant plume dispersion model. Plume effluent in a turbulent wind spreads in a random manner, meandering to create patches of high and low concentrations. Hence, a sophisticated dispersion plume model may be required to accurately estimate the contaminant source location using these methods. Alternatively, the BE algorithm requires minimal modeling assumptions, and simulation results suggest that

the BE algorithm is an effective strategy for estimating the source location.

To investigate the spatial relationship between air quality and traffic flow patterns, an experimental investigation based on real flow conditions was conducted to identify the source location (correlated with traffic flow) of an airborne contaminant (soot, i.e., attributed to traffic), using a Bayesian estimation algorithm. In the experiment LiDAR was employed to collect data of aerosol profiling in the atmosphere at several sites at ODU campus. Lidar and color ratios are retrieved from the data as aerosol's optical parameters. The results show that the primary source of harmful soot aerosol that is emitted by vehicles is at intersections due to congestion, which demonstrates that air quality is correlated with traffic flows and congestion caused by signalized intersections. Accordingly, to enhance the air quality and alleviate congestion, an advanced traffic signal controller has become increasingly necessary in a world with growing pressure on financial and physical resources.

Chapter 4

Proposed Traffic Signal Controller

This chapter presents the developed traffic signal timing optimization approach, to alleviate congestion at the intersection, using a Nash Bargaining game-theoretic framework. The Nash bargaining solution is applied to obtain the optimal control strategy on an isolated intersection, considering a variable phasing sequence and free cycle length. The system is implemented and evaluated in the INTEGRATION microscopic traffic assignment and simulation software. The proposed algorithm is compared to an optimum fixed-time plan (FP) controller and an actuated (ACT) controller to evaluate the performance of the proposed Nash bargaining approach at different traffic demand levels.

This chapter is organized as follows. Section 4.1 presents the framework of the developed controller. Section 4.2 describes the testbed intersection used in the simulation study, the traffic flow volume used in the simulation, the phasing scheme design used in the experiments, the simulation setup, and presents the experimental results at different traffic volume situations. Section 4.3 summarizes the work.

4.1 Traffic Signal Controller using game-theoretic framework

Game theory studies the interactive cooperation between intelligent rational decision makers, and has been widely used in economic, military, and communication. Game theory has also been applied to model traveler route choice behavior [20], control connected vehicle movements [21], and in route guidance [22]. Bargaining theory is related to cooperative games through the concept of Nash bargaining (NB). A bargaining situation is defined as a situation in which multiple players with specific objectives cooperate and benefit by reaching a mutually agreeable agreement. The bargaining process is the procedure that bargainers follow to reach an agreement (outcome), and the bargaining outcome is the result of the bargaining process. [23], [24]. The NB solution has been applied in a number of applications, including multimedia resource management [25], allocating multi-user channels to networks [26], a wireless cooperative relaying network [27], investment, wages and employment [28], [29], and for downlink beamforming in an interference channel [30].

Section 4.1.1 describes the NB solution for two players, and Section 4.1.2 describes how the NB approach is extended for multi-players.

4.1.1 NB Solution for Two Players Considering a Cooperative Game

A bargaining situation is defined as a situation in which multiple players with specific objectives cooperate and benefit by reaching a mutually agreeable outcome (agreement). In bargaining theory, there are two concepts: the bargaining process and the bargaining outcome. The bargaining process is the procedure that bargainers follow to reach an agreement (outcome) [95],[96]. Nash adopted an axiomatic approach that abstracts the bargaining process and considers only the bargaining outcome [23], [24]. The bargaining problem consists

of three basic elements: players, strategies, and utilities (rewards). Bargaining between two players is illustrated in the bi-matrix shown in Table 4.1. Each player, namely P_1 and P_2, has a set of possible actions A_1 and A_2, whose outcome preferences are given by the utility functions u and v, respectively, as they take relevant actions.

Table 4.1: Two players matrix game

		P_2	
		A_1	A_2
P_1	A_1	u_1, v_1	u_2, v_2
	A_2	u_3, v_3	u_4, v_4

The space (S) shown in Figure 4.1, is the set of all possible utilities that the two players can achieve; the vertices of the area are the utilities where each player chooses their pure strategy. The disagreement or the threat point $d = (d_1, d_2)$ corresponds to the minimum utilities that the players want to achieve. The disagreement point is a benchmark, and its selection affects the bargaining solution. Each player attempts to choose their disagreement point in order to maximize their bargaining position. Subsequently, a bargaining problem is

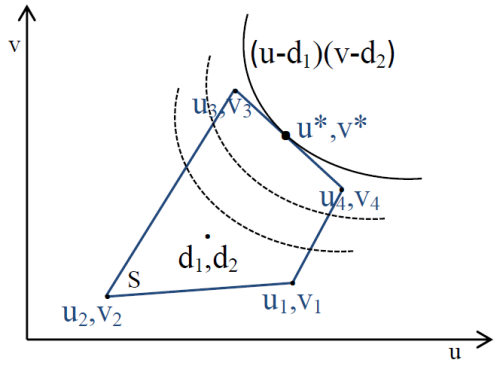

Figure 4.1: Utility region.

defined as the pair (S,d) where $S \in \mathbb{R}^2$ and $d \in S$ such that S is a convex and compact set, and there exists some $s \in S$ such that $s > d$. Nash stated the following four axioms that identify properties that the bargaining solution must satisfy:

- Pareto efficiency: at the bargaining outcome, no player can improve without decreasing

the other player's utility, i.e., no point $(u, v) \in S$ exists such that $u > u^*$ and $v \geq v^*$or $u \geq u^*$and $v > v^*$.

- Symmetry: the bargaining solution would not discriminate among the players if these players were indistinguishable, i.e., if $d_1 = d_2$ and S is symmetric around $u = v$, then $u^* = v^*$.

- Invariance to equivalent utility representation: the bargaining outcome varies linearly if the utilities are scaled using an affine transformation.

- Independence of irrelevant alternatives: if the solution of the bargaining problem lies in a subset $S'$of S, then the outcome does not change if bargaining is performed on S' instead of S.

Nash's theorem states that there exist a unique solution satisfying the four axioms, and this solution is the pair of utilities (u^*, v^*) that solves the following optimization problem:

$$\underset{u,v}{max}\ (u - d_1)(v - d_2), \tag{4.1}$$

$$s.t.(u, v) \in S, (u, v) \geq (d_1, d_2)$$

The NB solution (u^*, v^*) of this optimization problem can be calculated as the point in the bargaining set that maximizes the product of the players utility gains relative to a fixed disagreement point.

For two players the NB solution is shown below. The equation of the straight line (shown in Fig. 4.1) that has the optimal solution is defined as,

$$v = au + v_3 - au_3, \text{where}\ \ a = \frac{v_4 - v_3}{u_4 - u_3}$$

and the objective function is $J = (u - d_1)(v - d_2)$. The point that maximizes the objective function can be found by setting $\frac{\partial J}{\partial u} = 0, \frac{\partial J}{\partial v} = 0$ and solving for u^* and v^*, the optimal

solution is,

$$u^* = \frac{-(v_3 - au_3 - d_2 - ad_1)}{2a}, v^* = \frac{(v_3 - au_3 + ad_1 + d_2)}{2}$$

To show the existence and uniqueness of a solution that solves (4.1) and satisfies the four axioms, we proceed in two steps. In the first step, we show that the Nash bargaining solution (i.e., the solution to (4.1)) satisfies the four axioms. In the second step we show that if a bargaining solution satisfies the four axioms it is an NB solution. Noting that, the optimization problem (4.1) admits a unique optimal solution since: (i) S is a convex set, and (ii) the objective function is continuous and strictly quasi-concave and thus has a unique maximum.

Step 1: shows that the NB solution satisfies the four axioms.

1- Pareto efficiency (PE): this follows directly from the fact that the objective function is increasing in u and v, then the solution is indeed, Pareto optimal.

2- Symmetry (SYM): assume that $d_1 = d_2$ and let $\bar{u}^* = (u^*, v^*)$. Clearly (v^*, u^*) maximizes the objective function, and by uniqueness of the optimal solution $\bar{u}^* = (v^*, u^*) = (u^*, v^*)$, thus, the Nash bargaining solution satisfies the symmetry axiom.

3- Invariance to equivalent utility representation (IEUR): the bargaining outcome varies linearly if the utilities are scaled using an affine transformation. (S,d) $\Rightarrow$ (S',d'), with

$u_i' = \alpha_i u_i + \beta_i$, $d_i' = \alpha_i d_i + \beta_i$.

then the bargaining outcome $u^{*\prime} = \alpha_i u^* + \beta_i$.

$$(u' - d_1')(v' - d_2') = (\alpha_1 u + \beta_1 - \alpha_1 d_1 - \beta_1)(\alpha_2 v + \beta_2 - \alpha_2 d_2 - \beta_2)$$

$$= (\alpha_1 u - \alpha_1 d_1)(\alpha_2 v - \alpha_2 d_2) = \alpha_1 \alpha_2 (u - d_1)(v - d_2)$$

Now, (u^*, v^*) maximizes $(u - d_1)(v - d_2)$ over S if and only if

$$(u^* - d_1)(v^* - d_2) \geq (u - d_1)(v - d_2) \forall (u, v) \ \in S$$

if and only if

$$\alpha_1\alpha_2(u^* - d_1)(v^* - d_2) \geq \alpha_1\alpha_2(u - d_1)(v - d_2)$$

if and only if

$$(u^{*\prime} - d_1')(v^{*\prime} - d_2') \geq (u' - d_1')(v' - d_2') \forall (u', v') \in S'$$

where, $u_i^{*\prime} = \alpha_i u_i^* + \beta_i$. Then, $(\alpha_1 u^* + \beta_1, \alpha_2 v^* + \beta_2)$ maximizes $(u' - d_1')(v' - d_2')$ over S'.

4- Independence of irrelevant alternatives (IRA): let $S' \subseteq S$, from Equation (4.1), it is clear that the objective function value at the NB solution $f^*(S, d)$ is greater than or equal to the one at $f^*(S', d)$. If $f^*(S, d) \in S'$. then the objective function values must be equal; thus, $f^*(S, d)$ is optimal for S'. By the uniqueness of the solution, $f^*(S, d) = f^*(S', d)$.

Step 2: shows that if a bargaining solution satisfies the four axioms it is a NB solution. Consider a bargaining solution $f(S, d)$ satisfying the four axioms, and let us prove that this solution is indeed the NB solution $f^*(S, d)$. We need to show that $f(S, d) = f^*(S, d)$.

a) Let $f^*(S, d) = z$, and let S' be the image of S under an affine transformation that maps z to $(\frac{1}{2}, \frac{1}{2})$ and d to the origin, i.e.,

$$S' = \{\alpha_i s_i + \beta_i | s_i \in S\},$$

$$\alpha_i z_i + \beta_i = 0.5, \alpha_i d_i + \beta_i = 0 \forall i = 1, 2$$

since both f and f^* satisfy the IERU axiom, hence,

$$f_i(S', 0) = \alpha_i f_i(S, d) + \beta_i$$

$$f_i^*(S', 0) = \alpha_i f_i^*(S, d) + \beta_i = 0.5$$

Hence, $f(S, \mathrm{d}) = f^*(S, \mathrm{d}) \iff f(S', 0) = f^*(S', 0)$. Since $f^*(S', 0) = (0.5, 0.5)$ it remains to show that $f(S', 0) = (0.5, 0.5)$.

b) For this purpose, we show that there exists no $s \in S'$ such that $s_1 + s_2 > 1$. Assume that point s exists, and let

$$(t_1, t_2) = [(1-\lambda)\frac{1}{2} + \lambda s_1; (1-\lambda)\frac{1}{2} + \lambda s_2]$$

$$= (1-\lambda)(\frac{1}{2}, \frac{1}{2}) + \lambda(s_1, s_2), \quad \lambda \in (0, 1)$$

since S' is convex, then $(t_1, t_2) \in S'$. Now

$$t_1.t_2 = [(1-\lambda)\frac{1}{2} + \lambda s_1].[(1-\lambda)\frac{1}{2} + \lambda s_2]$$

$$= (1-\lambda)^2\frac{1}{4} + \frac{(1-\lambda)\lambda}{2}[s_1 + s_2] + \lambda^2 s_1 s_2 > \frac{1}{4}$$

If we choose λ sufficiently small such that $t_1.t_2 > \frac{1}{4}$, which contradicts the fact that $t_1.t_2 \leq \frac{1}{2}.\frac{1}{2}$ (since $f(S', 0) = (0.5, 0.5)$), and shows that $\forall s \in S'$ we have $s_1 + s_2 \leq 1$.

c) since S' is bounded, we can find a rectangular T, that is symmetric around a 45° line and contains $S'(S' \subseteq T)$, where $(\frac{1}{2}, \frac{1}{2})$ lies on the boundary of T. Consequently, by axioms PE and SYM, we have $f(T, 0) = (\frac{1}{2}, \frac{1}{2})$, and by axiom IRA, since $S' \subseteq T$, we have $f(S', 0) = f(T, 0) = (\frac{1}{2}, \frac{1}{2})$. Hence, the bargaining process provides a unique solution that satisfies a set of axioms conveyed by Nash.

4.1.2 Traffic Signal NB Solution for Multi-players

This section describes the game model and the NB solution for multi-players (N), and shows how the model is adapted (from Section 4.1.1) and applied to control a multi-phase signalized intersection. First, we use the standard NEMA phasing for a four-legged intersection [97], assuming we have four players (N = 4), to represent the intersection phases as shown in

Figure 4.2, with protected, leading main street left-turn phases.

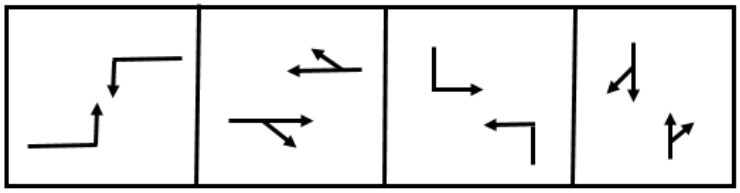

Figure 4.2: Phasing scheme.

In the game model, the four phases represent the players P_1, P_2, P_3, and P_4 of a four player cooperation game. For each player (phase), there are two possible actions: maintain (A_1) or change (A_2). These actions represent the state of the traffic signal [98]. Specifically, maintain indicates that the state of the signal will not change (i.e., if it is green, it will remain green; if it is red, it will remain red.). Change means the state of the signal will change (i.e., if it is green, it will switch to yellow and then red; if it is red, it will become green.) in the simulated time interval. The combinations of phases offer four possibilities, where only one player holds the green indication and all others hold red indications.

In the simulation, the INTEGRATION traffic simulation software monitors the vehicle speeds and the vehicle flow approaching the intersection and continuously updates them for each lane connected to the signalized intersection. If the vehicle (v) speed (s_v^t) is less than a certain threshold speed (s^{Th}) at time (t), the vehicle is assigned to the queue, and the current queue length associated with the corresponding lane (l) is updated. Once the vehicle's speed exceeds (s^{Th}), the queue length is updated (i.e., shortened by the number of vehicles leaving the queue) and formulated mathematically as

$$q_l^t = \sum_{v \in v_l^t} q_v^t \tag{4.2}$$

$$q_v^t = \begin{cases} 1 & \text{if } s_v^{t-1} > s^{Th} \ \& \ s_v^t \leq s^{Th} \\ \text{-1} & \text{if } s_v^{t-1} \leq s^{Th} \ \& \ s_v^t > s^{Th} \\ 0 & \begin{cases} \text{if } s_v^{t-1} \leq s^{Th} \ \& \ s_v^t \leq s^{Th} \\ \text{if } s_v^{t-1} > s^{Th} \ \& \ s_v^t > s^{Th} \end{cases} \end{cases} \tag{4.3}$$

q_l^t is the number of queued vehicles in lane l at time t.

The utilities (rewards) for each player (phase) in the game can be defined as the estimated sum of the queue lengths in each phase after applying a specific action. The estimated queue length after applying a specific action is calculated according to the following equation:

$$Q_P(t + \Delta t) = \sum_{l \in P} q_l^t + Q_{inl}\Delta t - Q_{outl}\Delta t \tag{4.4}$$

Where Δt is the updating time interval, q_l^t is the current queue length at time t, $Q_P(t+\Delta t)$ is the estimated queue length after Δt for phase P, Q_{inl} is the arrival flow rate (veh/h/lane), and Q_{outl} is the departure flow rate (veh/h/lane).

The block diagram of applying the NB controller is shown in Figure 4.3, where the predefined threat points values present an input to the controller. In addition, the flow ratios Q_{inl} and Q_{outl} can be measured by traffic loop detectors. Q_{outl} detectors are generally located at the downstream end of the links, whereas Q_{inl} detectors are located at distances from the downstream end of the links equal to threat points over jam densities.

The objective is to minimize and equalize the queue lengths across the different phases [99], [100]. We use minus queue length as the utility of each strategy. The NB solution is extended to four players (N=4) with a four-dimensional utility space and disagreement points. The solution for the NB over the four phase combinations has the following formula:

$$\underset{(\mathrm{u}_1,\ldots,\mathrm{u}_4)}{max} \prod_{i=1}^{\mathrm{N}} (\mathrm{u_i} - \mathrm{d_i}) \tag{4.5}$$

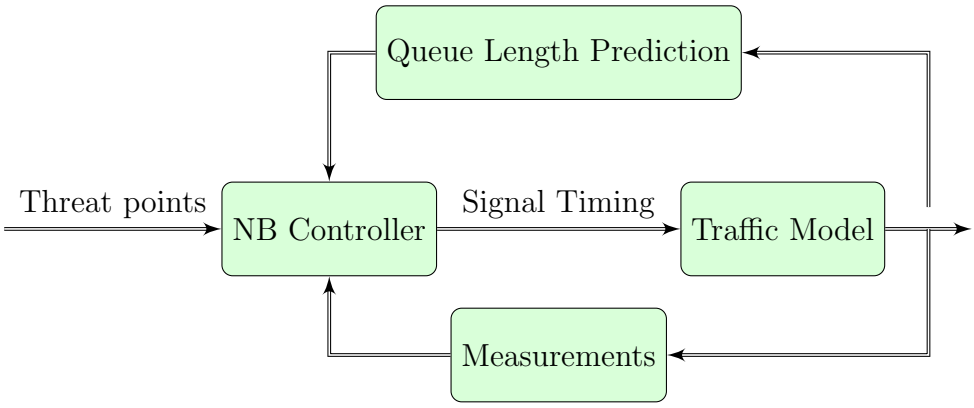

Figure 4.3: NB controller block diagram.

$$s.t.(\mathrm{u}_1, ..., \mathrm{u}_4) \in S, (\mathrm{u}_1, ..., \mathrm{u}_4) \geq (\mathrm{d}_1, ..., \mathrm{d}_4)$$

The NB solution can be calculated as the vector that maximizes the product of the player's utility gains relative to a fixed disagreement point.

4.1.3 Convexity of the Utility Space

This section shows that the utility space is convex for under-saturated traffic conditions, i.e. $\mathrm{u_i} \geq \mathrm{d_i}$ is convex. Fig. 4.4 shows the cumulative number of vehicles (N) that pass an observer by time (t). Consider a traffic signal that operates on a cycle length equal to C seconds, an effective red indication of R seconds, an effective green indication of G seconds, a maximum service rate during the effective green time of μ (veh/sec), a constant vehicle arrival rate of λ, the number of served vehicles in one cycle ($n' = \lambda C$), and number of delayed vehicles (n) [7]. The shaded area in Figure 4.4 represents the total delay during a cycle, denoted by w. From the geometry in the figure it is clear that:

$$R = (\frac{n}{\lambda}) - (\frac{n}{\mu})$$

Since the shaded area is:

$$w = \frac{n\ R}{2}$$

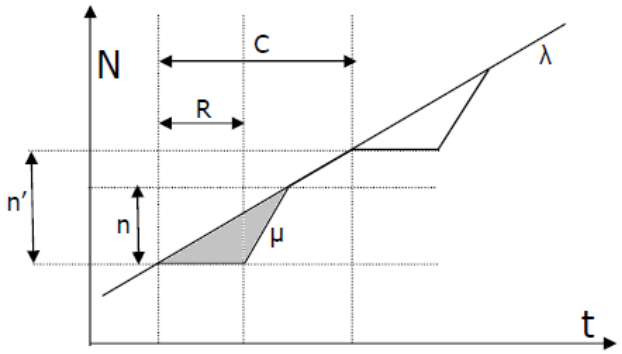

Figure 4.4: Traffic signal delay for under-saturated traffic conditions.

and

$$n = \frac{R}{(\frac{1}{\lambda} - \frac{1}{\mu})}$$

Then,

$$w = \frac{1}{2}\frac{\lambda\mu R^2}{\mu - \lambda}$$

The long run average delay per car is:

$$\bar{w} = \frac{w}{n'} = \frac{1}{2}\frac{\mu R^2}{(\mu - \lambda)C}$$

The queue length (reward for the NB) for a two-phase traffic signal with four approaches is developed below, where G_1, G_2 are in seconds and represent the effective green times for the two phases, L is the lost time, μ is the approach saturation flow rate (service), λ is the approach arrival rate, $R_1 = L + G_2$, $R_2 = L + G_1$, and $L = C - G_1 - G_2$.

The total delay per unit time is

$$y = \sum_{i=1,2,3,4} \lambda_i \bar{w}_i, \quad i \text{ is the approach number}$$

i.e.,

$$y = \frac{1}{2}[\frac{\lambda_1\mu_1 R_1^2}{(\mu_1 - \lambda_1)C} + \frac{\lambda_2\mu_2 R_1^2}{(\mu_2 - \lambda_2)C} + \frac{\lambda_3\mu_3 R_2^2}{(\mu_3 - \lambda_3)C} + \frac{\lambda_4\mu_4 R_2^2}{(\mu_4 - \lambda_4)C}]$$

which has units of veh-secs/secs; i.e.,'vehicles'. substituting by R_1, R_2, C, the sum of the average virtual queues (units of vehicles) on the four approaches is:

$$y = \frac{1}{2}[\frac{\lambda_1\mu_1(L+G_2)^2}{(\mu_1-\lambda_1)} + \frac{\lambda_2\mu_2(L+G_2)^2}{(\mu_2-\lambda_2)} + \frac{\lambda_3\mu_3(L+G_1)^2}{(\mu_3-\lambda_3)}$$

$$+\frac{\lambda_4\mu_4(L+G_1)^2}{(\mu_4-\lambda_4)}]\frac{1}{(L+G_1+G_2)}$$

Consequently, we need to show that the queue length function (y) is a convex function, Let

$$Z_1 = L+G_2, \quad Z_2 = L+G_1, \quad Z = L+G_1+G_2$$

Then,

$$y = \frac{1}{2}[\frac{\lambda_1\mu_1 Z_1^2}{(\mu_1-\lambda_1)} + \frac{\lambda_2\mu_2 Z_1^2}{(\mu_2-\lambda_2)} + \frac{\lambda_3\mu_3 Z_2^2}{(\mu_3-\lambda_3)} + \frac{\lambda_4\mu_4 Z_2^2}{(\mu_4-\lambda_4)}]\frac{1}{Z}$$

Let,

$$a = [\frac{\lambda_1\mu_1}{(\mu_1-\lambda_1)}], \quad b = [\frac{\lambda_2\mu_2}{(\mu_2-\lambda_2)}],$$

$$c = [\frac{\lambda_3\mu_3}{(\mu_3-\lambda_3)}], \quad d = [\frac{\lambda_4\mu_4}{(\mu_4-\lambda_4)}]$$

where, a, b, c, d are positive constants. Then,

$$y = aZ_1^2Z^{-1} + bZ_1^2Z^{-1} + cZ_2^2Z^{-1} + dZ_2^2Z^{-1} \tag{4.6}$$

Z^2 is a positive increasing convex function, Z^{-1} is a positive decreasing convex function. Consequently, Z^2Z^{-1} is a convex function given that it is the product of two positive convex functions with one of the functions increasing and the other decreasing. $aZ_1^2Z^{-1}$, $bZ_1^2Z^{-1}$, $cZ_2^2Z^{-1}$, and $dZ_2^2Z^{-1}$ are convex functions (a convex function multiplied by a positive constant remains convex). The sums of convex functions is convex, and as Z is a linear function of G_1, G_2, that implies that y is a convex function in G_1 and G_2.

To show that the utility space is convex, i.e. u $\geq$ d is convex, we define the reward (u) to be

the negative queue length (y), i.e., (u $= -$y), and we substitute (d) with a negative number (i.e., the number of vehicles that could be accumulated in specific lanes (d')), (d $= -d'$). Then (u $\geq$ d) is equivalent to ($-y \geq -d'$) or ($y \leq d'$), where d' is a constant positive number. The inequality ($y(G_1, G_2) \leq$ constant) defines a convex set since y is a convex function, which completes this step.

For over-saturated traffic conditions queues do not clear at the end of the green intervals (i.e. $\lambda_i C > \mu_i G$) shown in Figure 4.5, where T is the duration of observation period. To account

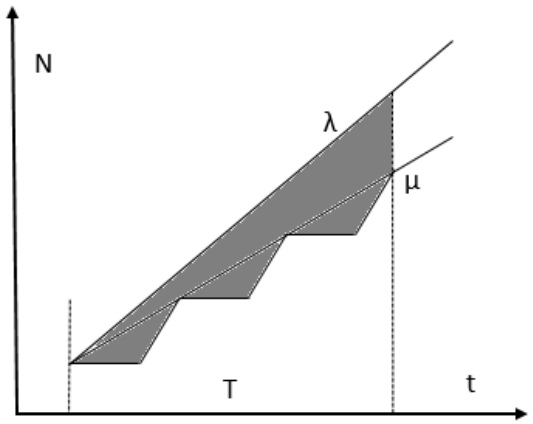

Figure 4.5: Traffic signal delay for an over-saturated traffic conditions.

for the number of vehicles that could not be served during green periods (the area of the large triangle in Figure 4.5 represents the over-saturation delay), additional terms (y_2) for the four approaches have to be added to equation (4.6). The average queue length (y_2) is:

$$y_2 = \frac{T}{2}[(\lambda_1 - \mu_1\frac{G1}{C}) + (\lambda_2 - \mu_2\frac{G1}{C})$$

$$+(\lambda_3 - \mu_3\frac{G2}{C}) + (\lambda_4 - \mu_4\frac{G2}{C})]$$

i.e.,

$$y_2 = \frac{T}{2}[(\lambda_1 - \mu_1\frac{Z_2 - L}{Z}) + (\lambda_2 - \mu_2\frac{Z_2 - L}{Z})$$

$$+(\lambda_3 - \mu_3\frac{Z_1 - L}{Z}) + (\lambda_4 - \mu_4\frac{Z_1 - L}{Z})]$$

Z_i is a positive increasing convex function, Z^{-1} is a positive decreasing convex function, and μ_i is a positive constant. Consequently, $\mu_i(Z_i - L)Z^{-1}$ is a convex function. However, $-\mu_i(Z_i - L)Z^{-1}$ is a concave function. Therefore, for over-saturated traffic conditions the total queue length is not a convex function. Consequently, for over-saturated conditions the NB approach does not guarantee convergence to the optimum solution.

The proposed controller was implemented on an isolated intersection to evaluate its performance, as described in the rest of this chapter. The structure of implementing the proposed controller is shown in Figure 4.6.

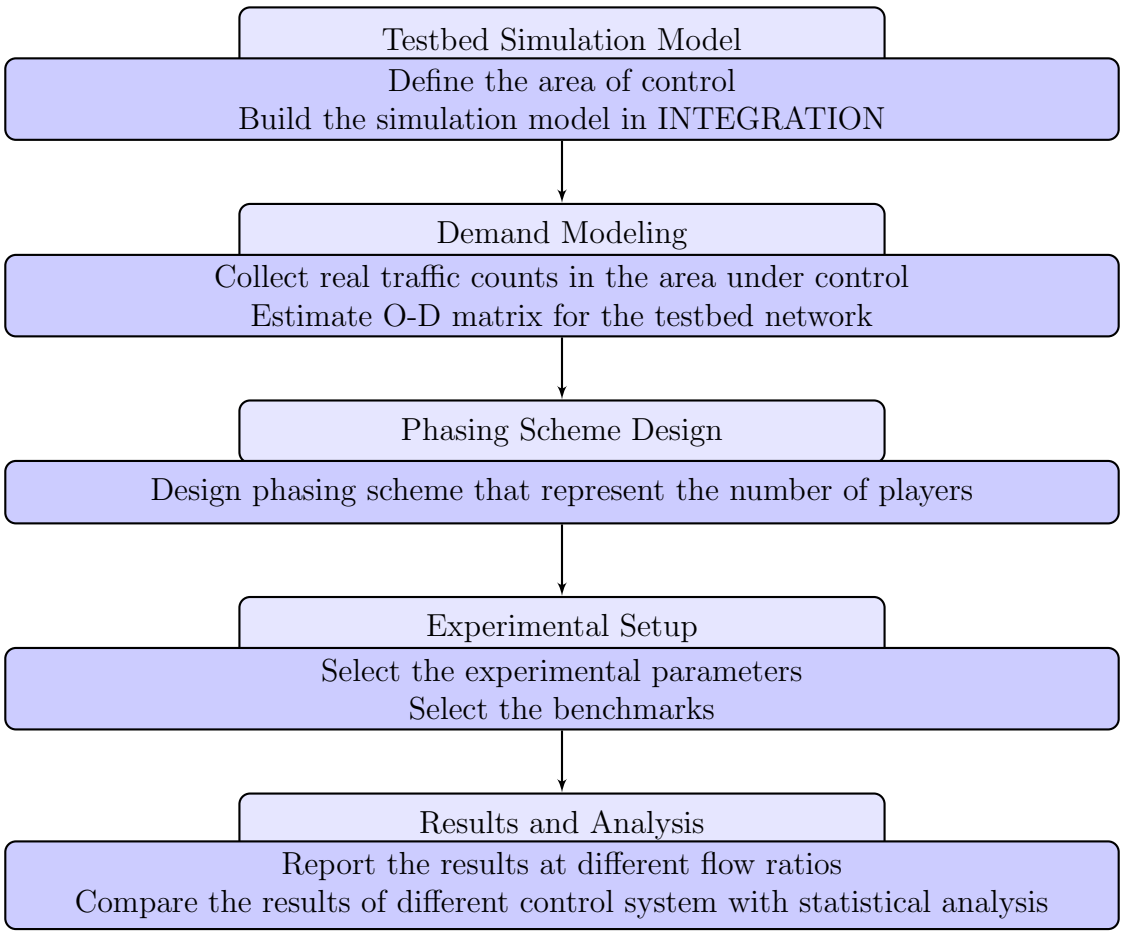

Figure 4.6: Roadmap for implementing the developed NB controller

4.2 Experimental Results: Isolated Intersection

4.2.1 Testbed Intersection

The experiments were tested using NB controller on an intersection with four approaches comprised of three lanes each located in the heart of downtown Toronto's financial district (intersection of Front and Bay streets) [101] as shown in Figure 4.7.

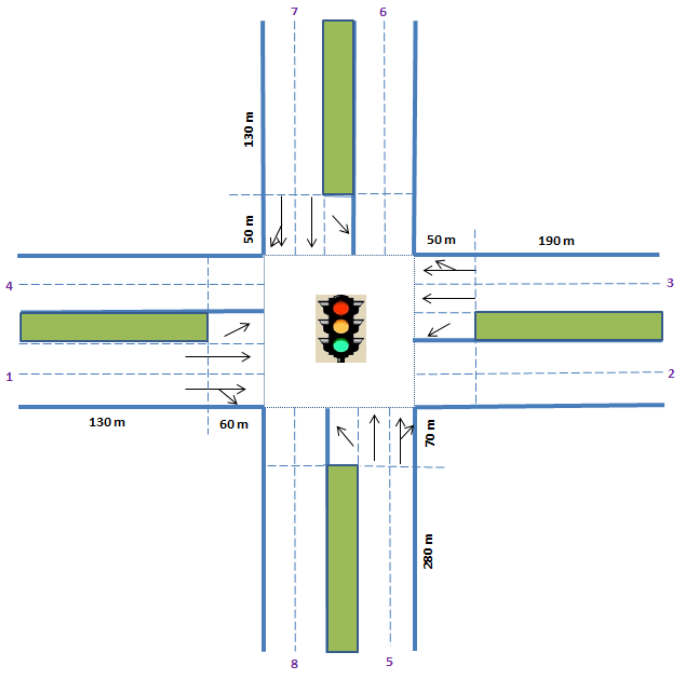

Figure 4.7: Testbed Intersection.

4.2.2 Demand Modeling

The traffic demand origin-destination (O-D) matrix provided in Table 4.2 [102], represents the highest total demand approaching the intersection during the afternoon rush hour (PM Peak) for the year 2005. The O-D matrix forms an input to INTEGRATION.

Table 4.2: Origin Destination Demand Matrix

Zone #	2	4	6	8	Total
1	1223	-	134	121	1478
3	-	844	86	278	1208
5	88	71	721	-	880
7	188	100	-	806	1094
Total	1499	1015	941	1205	4660

4.2.3 Phasing Scheme

The standard NEMA phasing for a four-legged intersection [97] represents the intersection phases as shown in Figure 4.8, with protected, leading main street left-turn phases. The four phases represent the four players (N = 4) in the game [103].

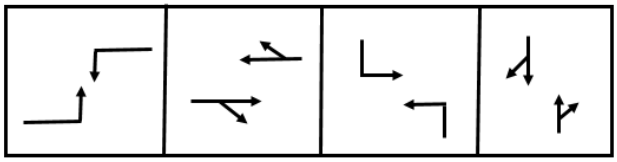

Figure 4.8: Phasing scheme.

4.2.4 Experimental Setup

This section describes the traffic simulation model used in the simulation (Section 4.2.4.1), the measures of effectiveness used to evaluate the performance of the system (Section 4.2.4.2), and the simulation parameters (Section 4.2.4.3).

4.2.4.1 Traffic Simulation Models

IINTEGRATION software was used to model the intersection [33]. It is a microscopic traffic simulation model that traces individual vehicle movements every deci-second. Driver characteristics such as reaction times, acceleration and deceleration rates, desired speeds,

and lane-changing behavior are examples of stochastic variables that are incorporated in INTEGRATION [104].

4.2.4.2 Measures of Effectiveness (MOEs)

The following measures of effectiveness were used to evaluate the performance of the system:

- Average Total Delay (s/veh): the sum of delay each deci-second for all vehicles for the entire simulation horizon divided by the number of vehicles.
- Average Stopped Delay (s/veh): the sum of instances where vehicle speed is less than or equal 3.6km/h (pedestrian speed) divided by the number of vehicles.
- Average Queue Length (veh): the sum of vehicles in queue each second divided by the simulation duration.
- Average Travel Time (s): the summation of all trip times divided by the number of vehicles.
- Average Vehicle Speed (km/h): the sum of instantaneous vehicle speeds divided by the number of vehicles.
- Average Throughput (veh/h): the total number of vehicles exiting the intersection divided by the simulation duration.
- Average Fuel (L): the total volume of fuel consumed by vehicles divided by the number of vehicles.
- Average CO2 (grams): the total amount of CO2 produced divided by the total number of vehicles.
- Last Vehicle Arrival Time(s): the arrival time of last vehicle to its destination.

4.2.4.3 Simulation Parameters

The fixed time signal plan was optimized using the Webster method [7], with yellow time of 3s, and all red time of 2s. The optimized effective green time for the four phases shown in Figure 4.8 were, 19s, 47s, 14s, 32s, respectively. The actuated control was implemented with minimum green time of 10s, maximum green time of 78s, and green extension time of 5s. The simulations were conducted using the following parameter values; speed at capacity = 60 (km/h), free flow speed = 80 (km/h), jam density = 160 (veh/km/lane), saturation flow rate = 1900 (veh/h/lane), and threshold speed s^{Th}= 4.5 (km/h).

4.2.5 Experimental Results

An optimum FP and an ACT controllers were simulated to serve as benchmarks to evaluate the performance of the NB approach. Vehicles were allowed to enter the links in the first hour, and the simulation ran for an extra half hour to guarantee that all vehicles exited the network. Three scenarios were simulated: one for the original O-D demand shown in Table 4.2, the second for a lower demand (L-D), i.e., (−25%) of the original demand, and the third for higher demand (H-D), i.e., (+25%) of the original demand.

4.2.5.1 Original Demand (O-D)

The simulation results shown below were obtained using three signal control systems: FP, ACT, and NB. The MOEs are shown in Table 4.3 to quantify the effect of each control system on the performance of the signalized intersection.

Five cases were conducted at different threat points (d), and at different updating intervals for NB (Δt) in order to study their effect on the performance of the NB algorithm. First, the performance of the intersection using the three control systems (FP, AC, NB) was

Table 4.3: Overall Intersection Performance Measure For Different Control Systems

MOE \ System	Fixed Plan	Actuated	Nash Bargaining				
			Case 1	Case 2	Case 3	Case 4	Case 5
Average Total Delay (s/veh)	74.268	76.270	32.176	29.390	26.906	43.312	48.148
Average Stopped Delay (s/veh)	46.878	48.77	15.837	13.619	9.553	11.158	25.010
Average Queue Length (veh)	8.294	8.559	2.781	2.484	1.891	2.955	4.623
Average Travel time (s)	116.141	137.566	53.366	50.577	48.080	74.280	69.879
Average Vehicle Speed (km/h)	21.455	20.617	38.965	38.302	39.954	31.514	31.501
Average Throughput (veh/h)	529.545	529.545	554.762	563.710	563.710	554.762	554.762
Average Fuel (L)	0.1197	0.1212	0.1028	0.1017	0.1037	0.1167	0.1097
Average CO2 (grams)	255.80	258.89	213.708	211.290	213.324	240.083	231.400
Last Vehicle Arrival time (s)	3852.3	3906.1	3701.1	3664.3	3672.3	3676.4	3693.2

investigated, at the following parameters values:

$$Case\ 1 \Rightarrow \mathrm{d} = (-17, -34, -19, -38),\ \Delta \mathrm{t} = 15\mathrm{s}$$

The threat point was chosen based on the number of cars that left turn pocket lanes could accommodate to prevent spill back into the through lane, where this number is duplicated for the right and the through movements.

The simulation results shown in Table 4.3 show that the NB approach outperforms the optimum FP and ACT controller. Since the traffic flow is high on all approaches, no considerable difference is reported between the FP and the ACT controllers. The NB approach exhibits significant savings in the average total delay, average stopped delay, average queue length, and average travel time. The NB shows an increase in the average vehicle speed and in the throughput. Subsequently, the performance of the intersection using the proposed NB approach was investigated using different threat points values and at the same updating interval, using the following parameters values

$$Case\ 2 \Rightarrow \mathrm{d} = (-17, -55, -19, -51),\ \Delta \mathrm{t} = 15\mathrm{s}$$

In this case, the threat point was chosen based on the number of cars that each phase can accommodate based on the lane lengths, shown in Figure 4.7, where the right turn and through lanes can accommodate more cars than the left turn lanes. The results shown in Table 4.3 show that MOEs in *case* 2 outperform the results in *case* 1.

Finally, three more simulations were conducted using the proposed NB algorithm to investigate the effect of the choice of the updating time interval on the algorithm performance using the same threat point values.

$$Case\ 3 \Rightarrow \mathrm{d} = (-17, -55, -19, -51), \Delta\mathrm{t} = 10\mathrm{s}$$

$$Case\ 4 \Rightarrow \mathrm{d} = (-17, -55, -19, -51), \Delta\mathrm{t} = 5\mathrm{s}$$

$$Case\ 5 \Rightarrow \mathrm{d} = (-17, -55, -19, -51), \Delta\mathrm{t} = 20\mathrm{s}$$

The results shown in Table 4.3 show that *case* 3 outperforms the results of the other cases, as well as the FP approach and the ACT approach.

Figure 4.9 shows the average queue length and the standard deviation across all movements for each control system, (FP, ACT, and NB). The NB algorithm shows significant reduction in the queue length.

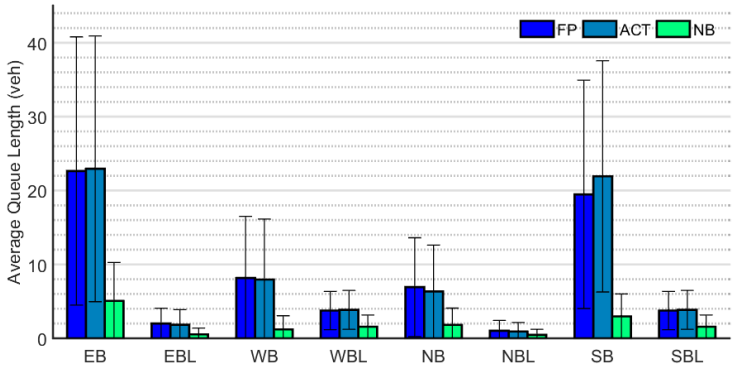

Figure 4.9: Average queue length.

Figure 4.10 shows the average values and the standard deviations of the MOEs across all

movements over the entire simulation time for each control system, (FP, ACT, and NB). The NB algorithm outperforms both FP and ACT for all movements with significant reduction in both the average values and the standard deviations for the total delay, stopped delay, arrival time, fuel consumption, and CO_2 emission. In addition the NB algorithm shows an increase in the average vehicle speed.

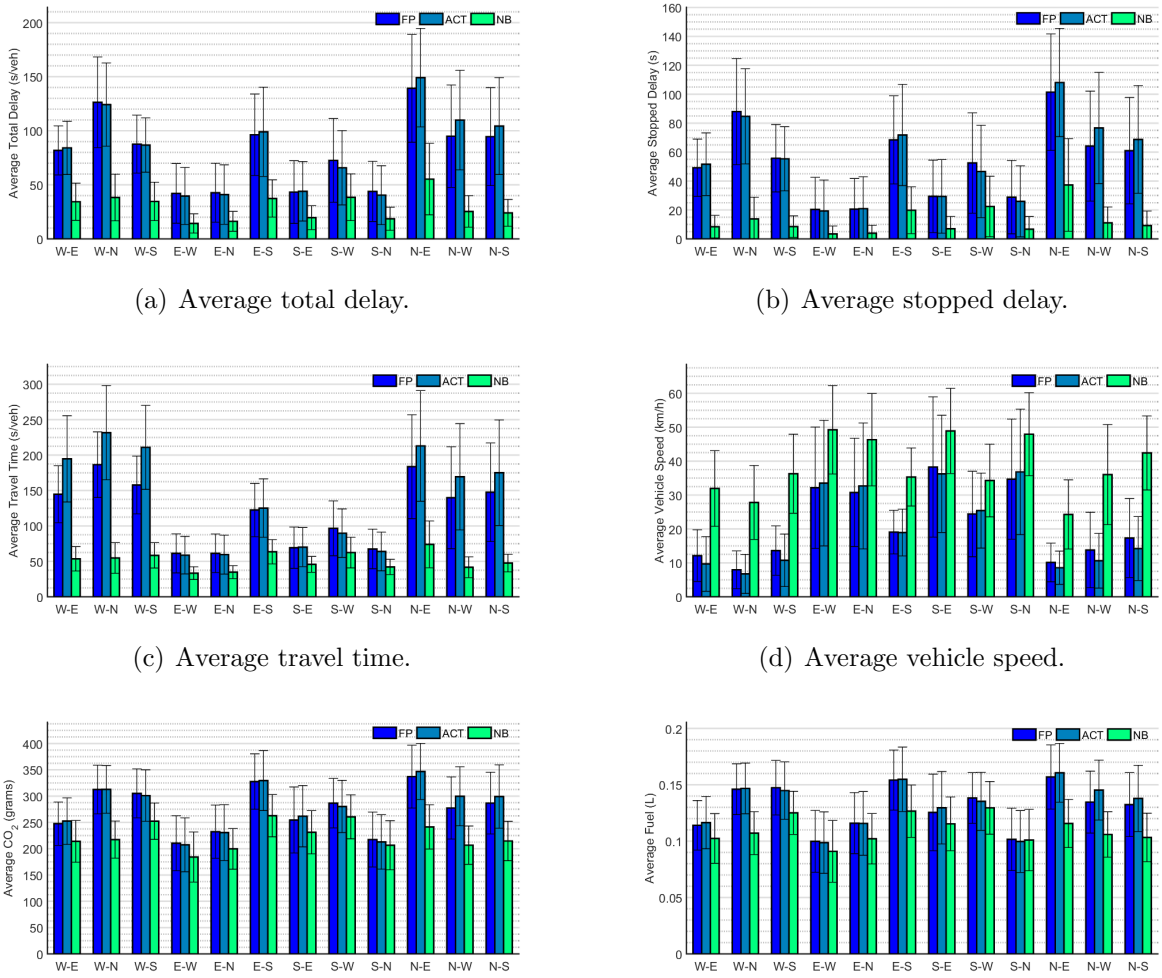

(a) Average total delay.

(b) Average stopped delay.

(c) Average travel time.

(d) Average vehicle speed.

(e) Average CO_2.

(f) Average fuel.

Figure 4.10: Measure of effectiveness.

The simulation results showed that, the NB control approach exhibited major improvements in both the average values and the standard deviations of all MOEs for different movements, which indicates that the system efficiency is improved.

4.2.5.2 Lower And Higher Demand

To better evaluate the performance of the NB approach, two other simulations were conducted, one at lower demand (L-D), and the other at higher demand (H-D).

Table 4.4 shows the results of using the three control approaches at the O-D, L-D, and H-D levels using the following NB algorithm parameters

$$\mathrm{d} = (-17, -55, -19, -51),\ \Delta\mathrm{t} = 10\mathrm{s}$$

Table 4.4: Intersection Performance Measure For Different Control Systems at Different Demand Profiles

Demand	L-D			O-D			H-D		
System / **MOE (Avg)**	FP	ACT	NB	FP	ACT	NB	FP	ACT	NB
Total Delay (s/veh)	41.473	42.913	17.854	74.268	76.270	26.906	101.783	102.938	59.994
Improvement %	56.9503	58.3949		63.7717	64.7227		41.0570	41.7183	
Stopped Delay (s/veh)	27.157	28.222	6.357	46.878	48.77	9.553	62.730	63.679	17.970
Improvement %	76.5917	77.4750		79.6216	80.4121		71.3534	71.803	
Queue Length (veh)	3.5340	3.7087	0.8827	8.2944	8.5593	1.8907	11.4293	11.4806	4.7811
Improvement %	75.0226	76.1992		77.2051	77.9106		58.1680	58.3550	
Travel time (s)	62.602	64.035	38.961	116.141	137.566	48.080	463.612	462.311	228.149
Improvement %	37.7640	39.1567		58.6020	65.0495		50.7888	50.6503	
Vehicle Speed (km/h)	35.759	34.987	47.442	21.455	20.617	39.954	9.600	9.435	21.435
Improvement %	32.6715	35.5989		86.223	93.7915		123.2812	127.186	
Throughput (veh/h)	415.95	415.95	422.66	529.54	529.54	563.71	526.44	532.86	598.56
Improvement %	1.6129	1.6129		6.4516	6.4516		13.6986	12.3287	
Fuel (L)	0.100	0.1017	0.0974	0.1197	0.1212	0.1037	0.1328	0.1337	0.1209
Improvement %	2.6000	4.2281		13.3668	14.4389		8.9608	9.5737	
CO2 (grams)	211.225	214.675	198.15	255.80	258.89	213.32	286.741	288.878	254.40
Improvement %	6.1858	7.6935		16.6052	17.6005		11.2764	11.9327	
Last Vehicle Arrival (s)	3705.2	3706.0	3652.2	3852.3	3906.1	3672.3	4884.8	4876.4	4284.2
Improvement %	1.4304	1.4517		4.6725	5.9855		12.2953	12.1442	

In addition, Table 4.4 shows the percent improvement in MOEs using the proposed NB

control approach over using either the FP or the ACT approach. The analysis of the results in Table 4.4 leads to the following findings: the proposed NB approach outperforms the FP and ACT approaches in terms of average stopped delay, average queue length, average travel time, average vehicle speed, average throughput, average fuel consumed, average CO_2 emitted, and time in which the last vehicle clears the network for different demand levels.

To further investigate the achieved improvements using the NB approach, simulations were conducted at different flow ratios (Y). The flow ratio can be formulated mathematically as

$$y_i = \frac{v_i}{s_i}, \quad Y = \sum y_{c,j} \tag{4.7}$$

where, y_i is the approach flow ratio for lane group i, v_i is the traffic volume, s_i is the saturation flow rate, $y_{c,j}$ is the critical flow ratio for all lane groups that discharge during phase j, and Y is the sum of all critical follow ratios for all phases.

Figure 4.11 shows the average queue length, the average total delay, and the average CO_2 at different flow ratios; Y ratios vary from 0.1 to 1.2. These results show that significant improvements are achieved using the NB approach at different traffic volumes.

Figure 4.12 shows the average queue length at two different flow ratios (Y) (i.e., 0.1 and 1.2). Considerable reductions in the queue lengths were found for all movements.

In summary, the simulation results showed that the NB control approach exhibited major improvements in the MOEs for all movements when compared to FP and ACT algorithms, which improves the system efficiency.

4.3 Summary

In this chapter the developed Nash bargaining (NB) controller was applied to an isolated intersection. The INTEGRATION microscopic traffic assignment and simulation software was used to evaluate the performance of the controller relative to an optimum fixed-time

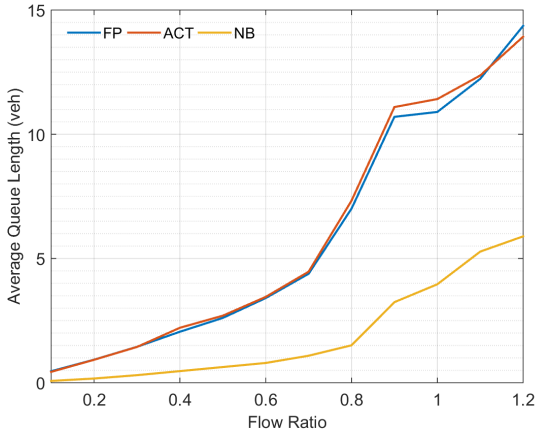

(a) Average queue length.

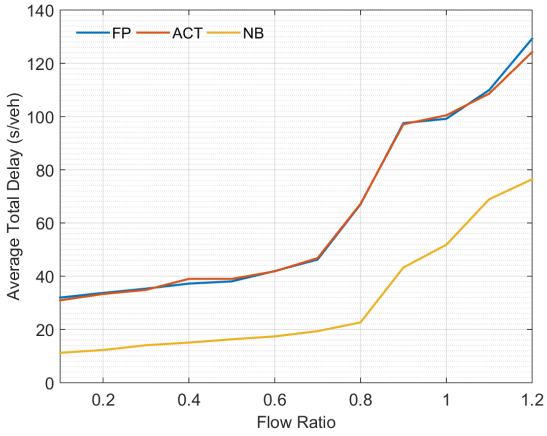

(b) Average total delay.

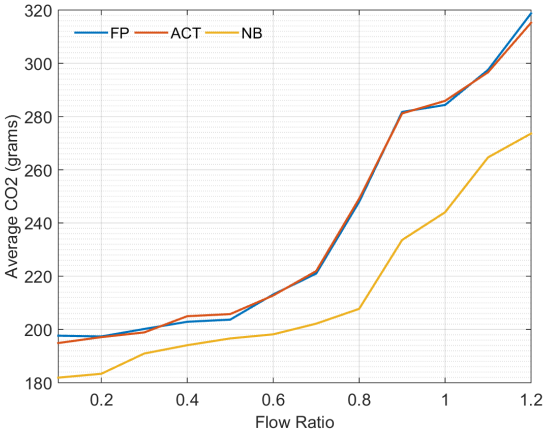

(c) Average CO_2.

Figure 4.11: Measure of effectiveness vs. flow ratio.

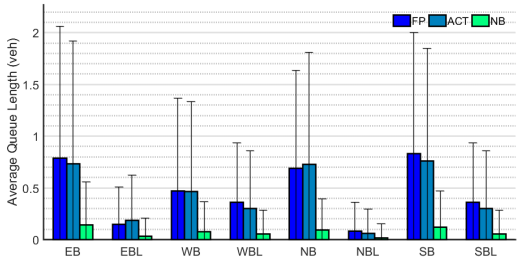

(a) Average queue length at 0.1 flow ratio.

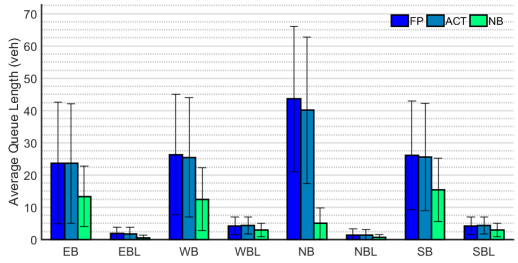

(b) Average queue length at 1.2 flow ratio.

Figure 4.12: Average queue length vs. flow ratio.

plan and an actuated controller on a major intersection in downtown Toronto using observed traffic data. Five NB controller scenarios were simulated considering different update time intervals and different threat point values to study the effect of these parameters on the controller's performance. The experimental results using the NB controller show that, using relatively short updating time interval, it is possible to minimize delay and maximize traffic flow efficiency. To evaluate the benefits of using the proposed approach, three scenarios were simulated using the three control approaches for different traffic demand levels. The results show significant reductions in the average total delay ranging from 41% to 64%, a reduction in the average queue length ranging from 58% to 77%, a reduction in the emission levels ranging from 6% to 17%, a reduction in the average travel time ranging from 37% to 65%, and a reduction in the network clearance time ranging from 1% to 12%. To further investigate the achieved improvements using the NB approach, simulations were conducted at different flow ratios.

The simulation results demonstrate a significant potential for the NB controller over FP and ACT controllers. Moreover, the results show that major improvements are achievable using the NB controller regardless of the traffic demand level. The next chapter (Chapter 5) entails extending the work to test the NB controller on an arterial network of multiple intersections.

Chapter 5

Experimental Results: Arterial Network

This chapter presents how the de-centralized controller (NB) could be applied on a network of multi-intersections. In addition, it presents the experimental results of applying a de-centralized controller (NB), considering a flexible phasing sequence and free cycle length on an arterial network. Traffic signal timing optimization is achieved using a NB game-theoretic framework, where each phase is modeled as a player in a game in which the players cooperate to reach a mutual agreement. The system is implemented and evaluated in the INTEGRATION microscopic traffic assignment and simulation software. The developed controller is compared to the operation of an optimum fixed-time coordinated plan, a centralized adaptive phase split controller, a decentralized phase split and cycle length controller, and a fully coordinated adaptive phase split, cycle length, and offset optimization controller to evaluate the performance of the proposed decentralized controller. Analysis of variance (ANOVA), Tukey, and pairwise comparison tests were conducted, to examine the statistically significant difference of the proposed controller.

The chapter is organized as follows. Section 5.1 describes how to apply the NB controller on multi-intersections. Section 5.2 describes the arterial testbed network used in the simu-

lation, the traffic flow volume used in the simulation, the phasing scheme design used in the experiments, the simulation setup, and the experimental results. Section 5.3 presents the statistical analysis of the results. Section 5.4 summarizes the work.

5.1 De-Centralized NB controller for Multi-intersections

This section presents the de-centralized mechanism of the NB controller on multi-intersections, for the purpose of illustration, we will explain the NB controller behavior on three intersections shown in Table 5.1. Assume we have three intersections ($I_1, I_2,\ I_3$), each intersection has three phases ($Ph_1, Ph_2,\ Ph_3$), where each phase is considered as a player in the game. Hence, each intersection has three players, i.e., I_1 has three players ($P_1, P_2,\ P_3$), I_2 has three players ($P_4, P_5,\ P_6$), and I_3 has three players ($P_7, P_8,\ P_9$). Every intersection has three possible actions (A), where one phase has a green (G) period and the others are red (R) as illustrated in Table 5.1.

Table 5.1: Multi-players matrix game

Intersection	First Intersection (I_1)			Second Intersection (I_2)			Third Intersection (I_3)		
Player / **Action**	Ph1(P_1)	Ph2(P_2)	Ph3(P_3)	Ph1(P_4)	Ph2(P_5)	Ph3(P_6)	Ph1(P_7)	Ph2(P_8)	Ph3(P_9)
First	G	R	R	G	R	R	G	R	R
	A_{11}			**A_{21}**			A_{31}		
Second	R	G	R	R	G	R	R	G	R
	A_{12}			A_{22}			A_{32}		
Third	R	R	G	R	R	G	R	R	G
	A_{13}			A_{23}			**A_{33}**		

Therefore, for the network of three intersections illustrated in Table 5.1, there are 27 possible scenarios (actions permutations) as shown in Table 5.2. In order to maximize the overall network performance, we are looking for the best scenario in Table 5.2.

Table 5.2: All possible Network Actions (Permutations)

Scenario #	Network Action
1	A_{11} A_{21} A_{31}
2	A_{11} A_{21} A_{32}
3	A_{11} A_{21} A_{33}
4	A_{11} A_{22} A_{31}
5	A_{11} A_{22} A_{32}
6	A_{11} A_{22} A_{33}
7	A_{11} A_{23} A_{31}
8	A_{11} A_{23} A_{32}
9	A_{11} A_{23} A_{33}
10	A_{12} A_{21} A_{31}
11	A_{12} A_{21} A_{32}
12	$\mathbf{A_{12}}$ $\mathbf{A_{21}}$ $\mathbf{A_{33}}$
13	A_{12} A_{22} A_{31}
14	A_{12} A_{22} A_{32}
15	A_{12} A_{22} A_{33}
16	A_{12} A_{23} A_{31}
17	A_{12} A_{23} A_{32}
18	A_{12} A_{23} A_{33}
19	A_{13} A_{21} A_{31}
20	A_{13} A_{21} A_{32}
21	A_{13} A_{21} A_{33}
22	A_{13} A_{22} A_{31}
23	A_{13} A_{22} A_{32}
24	A_{13} A_{22} A_{33}
25	A_{13} A_{23} A_{31}
26	A_{13} A_{23} A_{32}
27	A_{13} A_{23} A_{33}

Referring to Table 5.1, and assume that the first intersection (I_1) has an action ($\mathbf{A_{12}}$) that will maximize its own performance, and intersection (I_2) has an action ($\mathbf{A_{21}}$) that will maximize its own performance, and intersection (I_3) has an action ($\mathbf{A_{33}}$) that will maximize its own performance. Consequently, noting worthy, searching in Table 5.2 for the best combination yields scenario 12. Therefore, to achieve the maximum network performance it is sufficient to search for the actions that will maximize intersections performance individually, also it could be described using the NB optimization problem shown in the following equations.

$$\max_{(u_1,\ldots,u_9)} \prod_{i=1}^{9} (u_i - d_i) \tag{5.1}$$

$$= \max_{(u_1,\ldots,u_9)} [\underbrace{\prod_{i=1}^{3} (u_i - d_i)}_{I_1} \quad \underbrace{\prod_{i=4}^{6} (u_i - d_i)}_{I_2} \quad \underbrace{\prod_{i=7}^{9} (u_i - d_i)}_{I_3}]$$

$$= \underbrace{\max_{(u_1,\ldots,u_3)} \prod_{i=1}^{3} (u_i - d_i)}_{I_1} \quad \underbrace{\max_{(u_4,\ldots,u_6)} \prod_{i=4}^{6} (u_i - d_i)}_{I_2} \quad \underbrace{\max_{(u_7,\ldots,u_9)} \prod_{i=7}^{9} (u_i - d_i)}_{I_3}$$

Worth noting, no intersection has to scarify its own performance to achieve network optimization. Therefore, the NB controller is decentralized, which enables controlling a large urban traffic network and avoids the issue of a single point failure in the centralized systems, and avoid the problems inherent with complex centralized communication. The decentralized behavior of the NB controller will increase both the scalability and robustness of the system, where for other controllers the complexity of the system increases exponentially with the number of intersections when the network is expanded.

5.2 Experimental results: Arterial Network

5.2.1 Testbed Arterial Network

The proposed controller was simulated on an arterial network located in the heart of downtown of Blacksburg, shown in Figure 5.1.

5.2.2 Demand Modeling

The origin-destination (O-D) demand matrices were generated using the QueensOD software [105], based on counts collected during the afternoon peak period ($4-6$ PM), at 15 minute

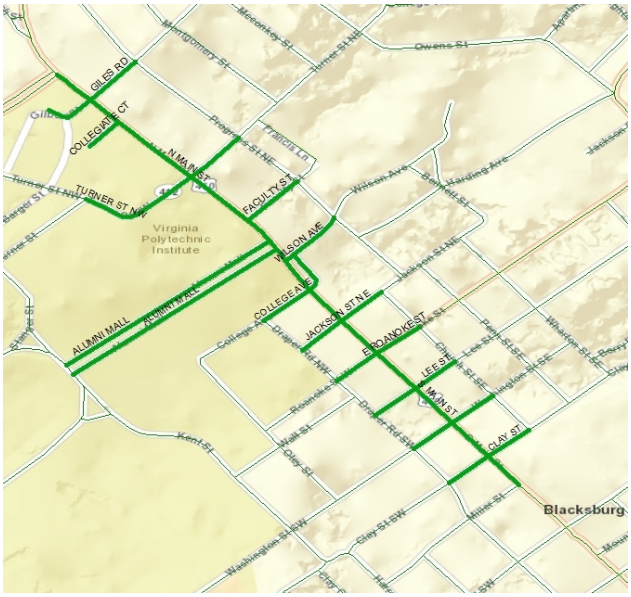

(a) Google image.

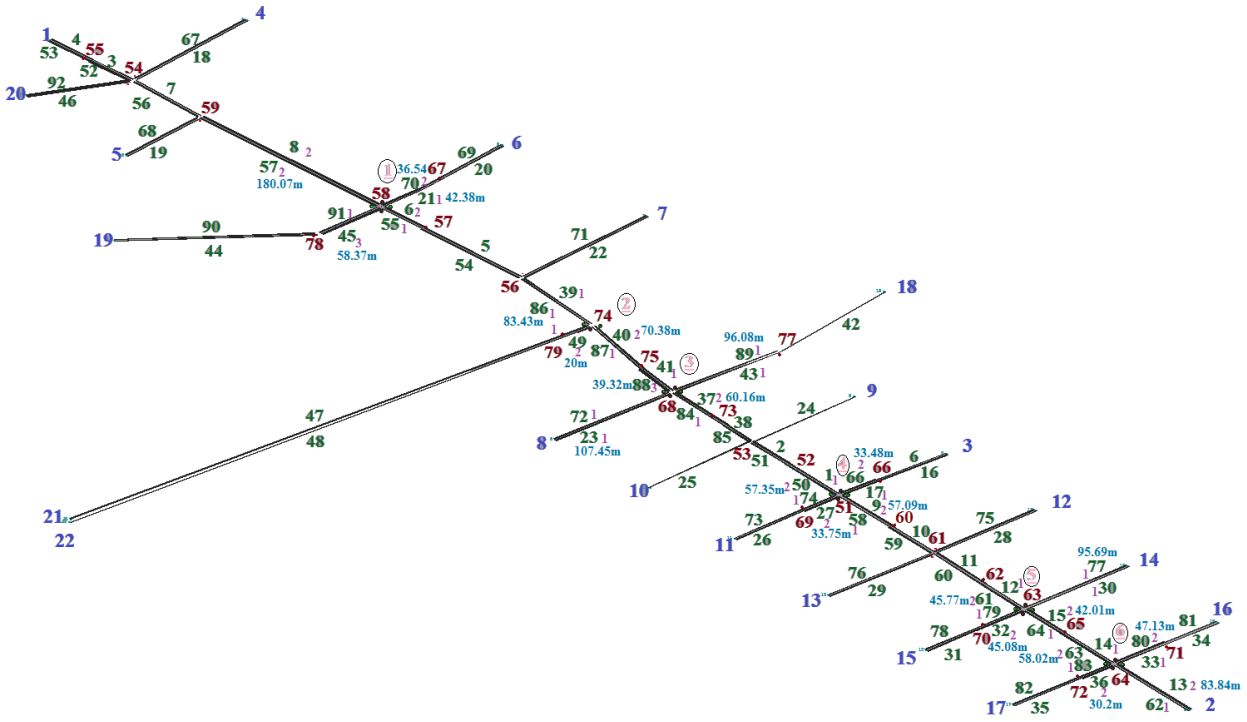

(b) INTEGRATION model.

Figure 5.1: Blacksburg testbed arterial network.

intervals, for the year 2012,[106].

5.2.3 Phasing Scheme

Three-phase signalized intersection scheme (Figure 5.2) was used to represent the intersection phases that is applied in the downtown of Blacksburg network, with protected leading main street left-turn phases. The three phases represent the three players (N = 3) in the game.

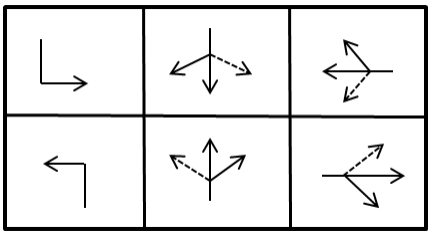

Figure 5.2: Phasing scheme.

In the game model, the three phases represent the players P_1, P_2, and P_3 of a three players cooperation game. For each player (phase), there are two possible actions: maintain (A_1) or change (A_2). These actions represent the state of the traffic signal. The NB solution for three players with a three-dimensional utility space and disagreement points has the following formula:

$$\underset{(u_1,u_2,u_3)}{max} \prod_{i=1}^{3} (u_i - d_i) \tag{5.2}$$

$$s.t.(u_1, u_2, u_3) \in S, (u_1, u_2, u_3) \geq (d_1, d_2, d_3)$$

The NB solution can be calculated as the vector that maximizes the product of the players utility gains relative to a fixed disagreement points. Refer to Section 4.1.2 for more details about the NB controller.

5.2.4 Experimental Setup

This section describes the benchmarks used to evaluate the performance of the developed controller (Section 5.2.4.1), and the simulation parameters (Section 5.2.4.2).

5.2.4.1 Benchmarks

The performance of the NB controller is compared to the operation of an optimum fixed-time coordinated plan (FP), a centralized adaptive phase split controller (PS), a decentralized phase split and cycle length controller (PSC) [10], and a fully coordinated adaptive phase split-cycle length and offset optimization controller (PSCO) [31],[32], to evaluate the performance of the proposed decentralized controller.

5.2.4.2 Simulation Parameters

The simulations were conducted using the following parameters values; free-flow speed (40 km/h) based on the roadway speed limit, speed-at-capacity (29 km/h), jam density (160 veh/km/lane), saturation flow rate (1800 veh/h/lane), threshold speed (s^{Th}=4.5 km/h). These values are based on field measurements and typical values for arterial roadways. In the simulation vehicles were allowed to enter the links in the first two hour, and the simulation ran for an extra 15 minutes to guarantee that all vehicles exited the network. The FP was simulated using the observed signals times in the field. PS was optimized every 120s. PSC and PSCO was optimized every 120s, considering a minimum cycle length of 30s and a maximum cycle length of 120s. In the simulation vehicles were allowed to enter the links in the first two hour, and the simulation ran for an extra 15 minutes to guarantee that all vehicles exited the network.

5.2.5 Experimental Results

The simulation results shown below represent the average of 30 simulation runs at random seeds. The performance of the arterial network using the NB approach was conducted, such that the threat points were chosen based on the number of vehicles that each phase can accommodate based on the link lengths and number of lanes considering an updating time interval of 10s.

Figure 5.3 shows the average values and the standard deviations of the MOEs across all movements over the entire simulation time for each control system, (FP, PS, PSC, PSCO, and NB). The NB approach outperforms other control approaches for all movements with significant reduction in both the average values and the standard deviations for the total delay, stopped delay, travel time, fuel consumption, and CO_2 emission.

In addition, Table 5.3 shows the percent improvement in MOEs using the proposed NB approach over other approaches, for 30 simulations with random seeds. Analysis of the results in Table 5.3 demonstrates the following: the proposed NB approach outperforms other approaches in terms of average total delay, average travel time, average fuel consumed, average CO_2 emitted, and the clearance time of the last vehicle.

Figure 5.4 shows the average queue length for the six intersections, across all movements. The NB control system outperforms other control systems (FP, PS, PSC, PSCO) for all movements. The simulation results showed that, the NB control approach exhibited major improvements in the average values and the standard deviations of all MOEs for different movements, which indicates that the system efficiency is improved.

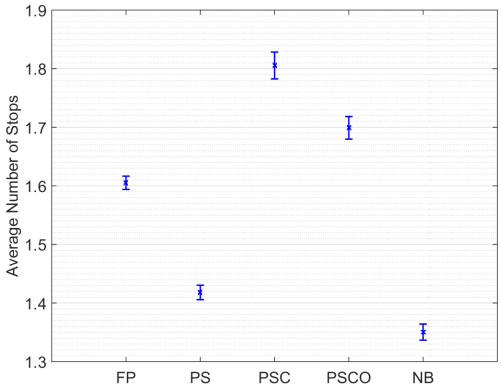

(a) Average number of stops.

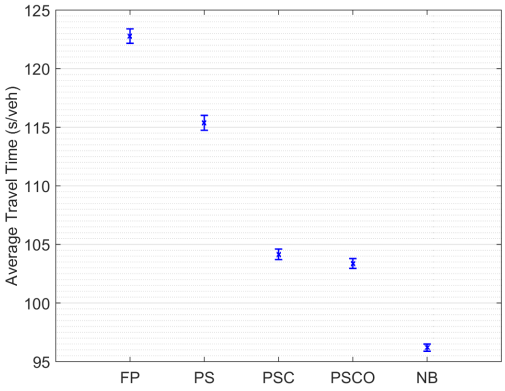

(b) Average travel time.

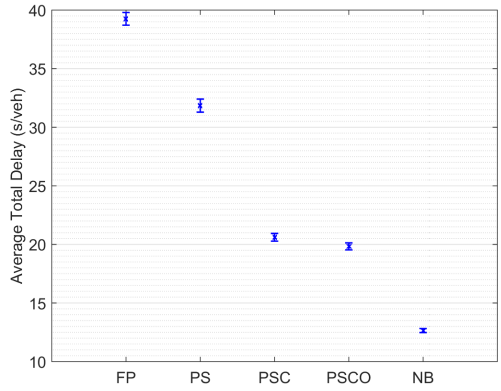

(c) Average total delay.

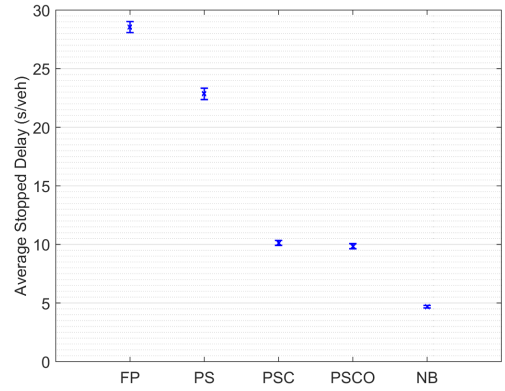

(d) Average stopped delay.

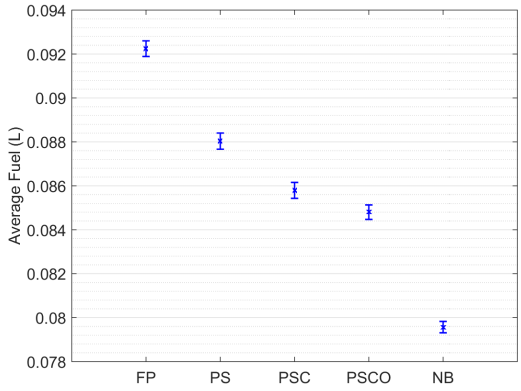

(e) Average fuel.

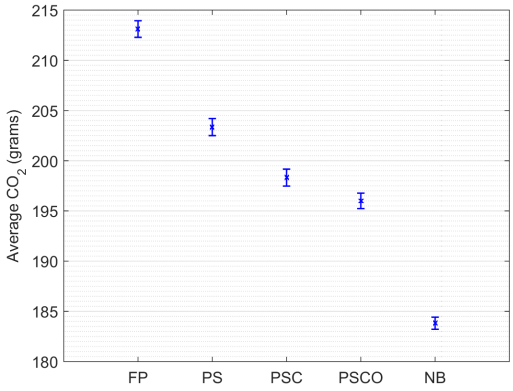

(f) Average CO_2.

Figure 5.3: Average MOEs of 30 simulations at random seeds.

Table 5.3: Average MOEs and the percent improvement using NB controller over other controllers

MOE \ System	FP	PS	PSC	PSCO	NB
Average Total Delay (s/veh)	39.255	31.847	20.609	19.833	12.649
Improvement %	67.777	60.282	38.624	36.223	
Average Stopped Delay (s/veh)	28.549	22.849	10.127	9.849	4.686
Improvement %	83.585	79.490	53.723	52.418	
Average Travel time (s)	122.780	115.376	104.155	103.373	96.188
Improvement %	21.658	16.630	7.649	6.950	
Average Number of Stops	1.605	1.418	1.805	1.699	1.350
Improvement %	15.879	4.776	25.205	20.522	
Average Fuel (L)	0.092	0.088	0.086	0.085	0.080
Improvement %	13.740	9.617	7.256	6.170	
Average CO2 (grams)	213.114	203.352	198.322	196.003	183.820
Improvement %	13.746	9.605	7.312	6.216	
Last Vehicle Arrival time (s)	7380.9	7328.0	7316.8	7338.9	7311.9
Improvement %	0.935	0.220	0.067	0.368	

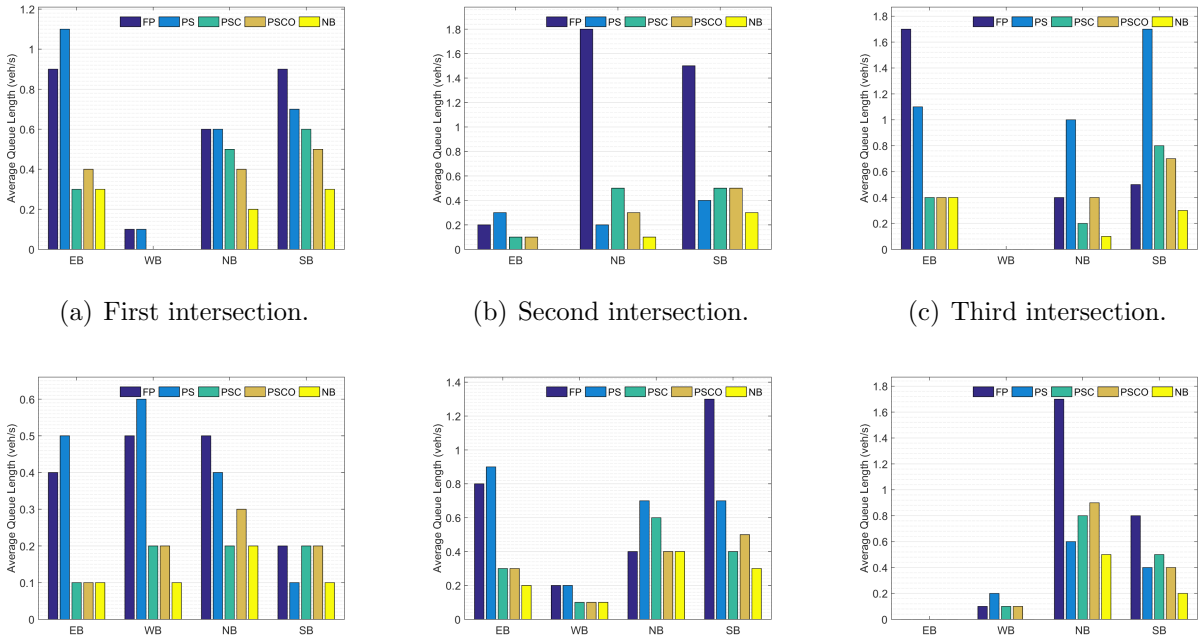

(a) First intersection. (b) Second intersection. (c) Third intersection.

(d) Fourth intersection. (e) Fifth intersection. (f) Sixth intersection.

Figure 5.4: Average queue length of the intersections.

5.3 Statistical Analysis

To study the statistical significance of these findings, we applied an Analysis of Variance (ANOVA) test to the data. ANOVA is a statistical test used to identify significant differences between the means of three or more independent groups. We applied the test on all MOEs, however, we only show the results for the average total delay.

Figure 5.5 shows that the assumptions of the ANOVA test are validated, i.e., normality and equal variance. The distribution of the studentized residuals follow a normal distribution, and have equal variances.

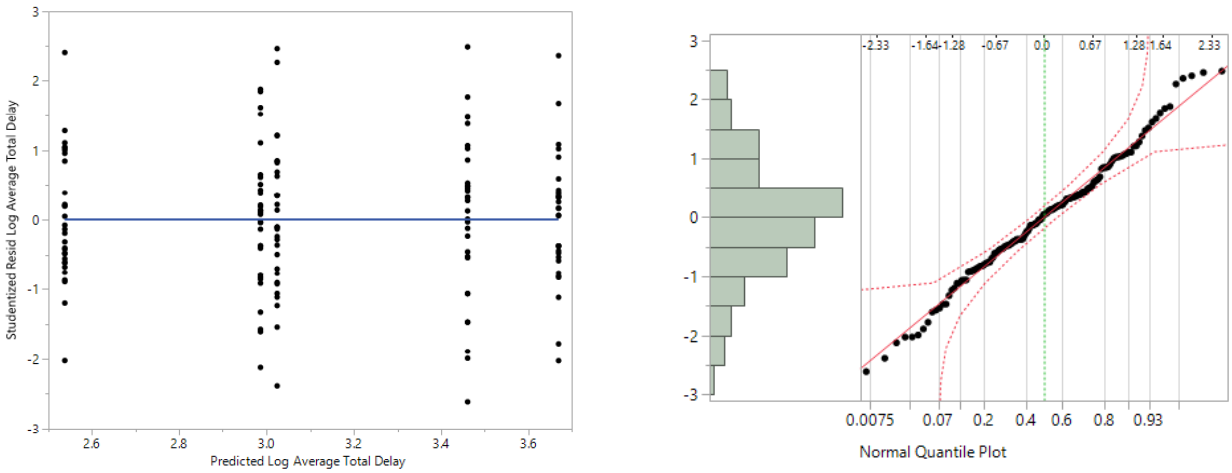

(a) Variance. (b) Normality.

Figure 5.5: Assumptions of ANOVA test.

Table 5.4 shows that the null hypothesis for ANOVA, i.e., the mean is the same for all approaches, is rejected, and at least on approach has statistically significant different mean.

Table 5.4: Analysis of Variance

Source	DF	Sum of Squares	Mean Square	F Ratio	Prob>F
Algorithm	4	23.492544	5.87314	25124.81	<0.0001
Error	145	0.033895	0.00023		
C. Total	149	23.526439			

In addition, we applied the Tukey test to determine which approaches are similar. Table 5.5 shows the results of the Tukey test, where levels not connected by the same letter are significantly different.

Table 5.5: Tukey Test

Level						Least Square Mean
FP	A					3.6699004
PS		B				3.4607800
PSC			C			3.0255877
PSCO				D		2.9872279
NB					E	2.5374774

Moreover, pairwise comparison test was conducted to compare approaches in pairs to identify the approaches with similar measures of effectiveness (MOEs). The results shown in Table 5.6 conclude that, NB control approach exhibited major improvements over other approaches, and is statistically significant.

Table 5.6: Pair Wise Comparison

Level	-Level	Difference	Std Err Dif	Lower CL	Upper CL	P-Value
FP	NB	1.132423	0.0039476	1.121518	1.143328	<0.0001
PS	NB	0.923303	0.0039476	0.912398	0.934208	<0.0001
FP	PSCO	0.682672	0.0039476	0.671767	0.693577	<0.0001
FP	PSC	0.644313	0.0039476	0.633408	0.655218	<0.0001
PSC	NB	0.488110	0.0039476	0.477205	0.499015	<0.0001
PS	PSCO	0.473552	0.0039476	0.462647	0.484457	<0.0001
PSCO	NB	0.449750	0.0039476	0.438845	0.460655	<0.0001
PS	PSC	0.435192	0.0039476	0.424287	0.446097	<0.0001
FP	PS	0.209120	0.0039476	0.198215	0.220025	<0.0001
PSC	PSCO	0.038360	0.0039476	0.027455	0.049265	<0.0001

5.4 Summary

In this chapter the developed NB de-centralized cycle-free traffic signal controller was applied on an arterial network. The INTEGRATION microscopic traffic assignment and sim-

ulation software was used to evaluate the performance of the proposed controller relative to an optimum fixed-time coordinated plan, a centralized adaptive phase split controller, a decentralized phase split and cycle length optimization controller, and a fully-coordinated adaptive phase split, cycle length and offset optimization controller, on an arterial network in downtown Blacksburg, VA. A total of 30 random seed simulations were conducted for the five control approaches. The experimental results using the NB controller show that, with a flexible phasing sequence and free cycle length control strategy, it is possible to minimize delay and maximize traffic flow efficiency. The results show significant reductions in the average queue length, in the average total delay ranging from 36% to 67%, a reduction in the emission levels ranging from 6% to 13%, a reduction in the average travel time ranging from 7% to 21%, and a reduction in the network clearance time. Analysis of variance tests, Tukey tests, and pairwise comparison tests were conducted, to validate the benefits of using the proposed approach (NB), and the results show that NB controller produces major improvements over that other approaches. The results demonstrate a significant potential for the proposed controller over other state-of-the-art centralized and de-centralized control approaches. The next chapter (Chapter 6) entails extending the work to test the NB controller on large scale networks.

Chapter 6

Experimental Results: Large Scale Networks

This chapter describes the application and testing of the proposed decentralized cycle-free NB controller on large-scale networks. The system was implemented and evaluated in the INTEGRATION microscopic traffic assignment and simulation software. The developed controller was compared to the operation of a decentralized phase split and cycle length controller, and a fully coordinated adaptive phase split, cycle length, and offset optimization controller to evaluate its performance.

The chapter is organized as follows. Section 6.1 presents the experimental setup and results of large scale studies in the town of Blacksburg, Virginia, consisting of 38 signalized intersections. Section 6.2 describes the experimental setup and the experimental results of large scale studies on a downtown network in Los Angles, California, consisting of 457 signalized intersections. Section 6.3 summarizes the work.

6.1 Blacksburg Town Experiments

6.1.1 Blacksburg Experimental Setup

These experiments were large scale studies carried out in the town of Blacksburg (BB), Virginia, shown in Figure 6.1. The simulations were conducted using the morning peak hour $(7-8$ a.m.) traffic demand. The town of Blacksburg has 38 signalized intersections, 549 stop signs, 30 yield signs, and 1844 links.

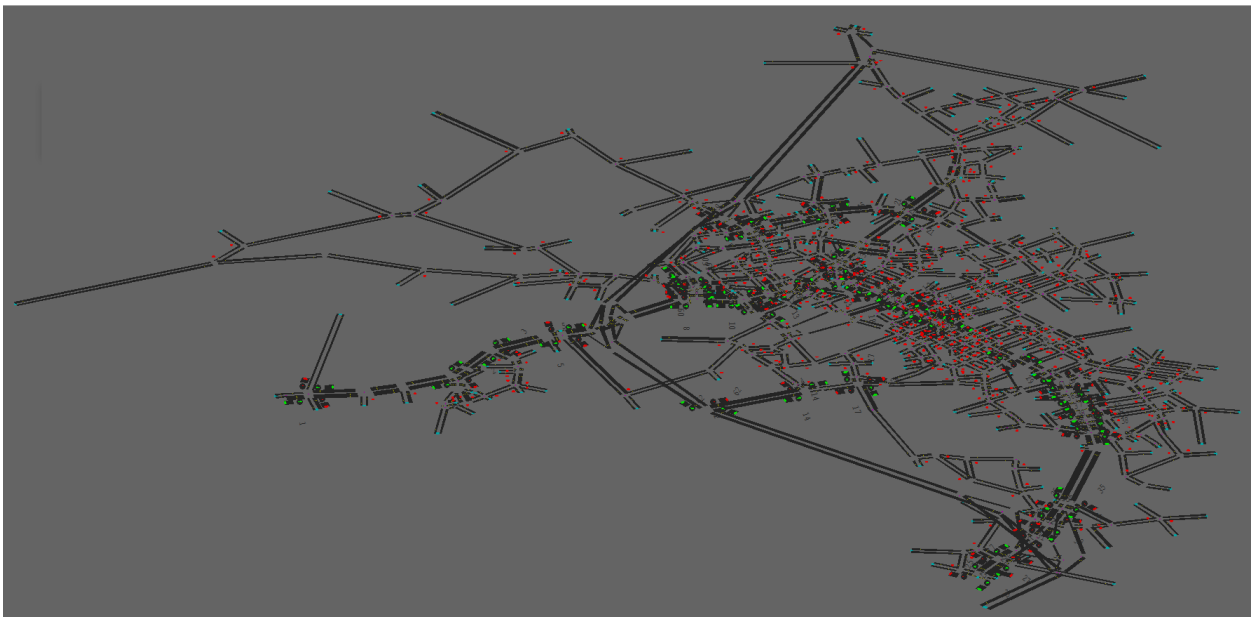

Figure 6.1: Blacksburg network.

The origin-destination (O-D) demand matrices were generated using the QueensOD software [105] and consisted of $23,260$ trips. The phasing scheme varied between 2 to 4 phases, reflecting the intersection phases implemented in the town. The minimum free-flow speed on the network was 30 (km/h), and the maximum free-flow speed on the network was 105 (km/h). The minimum link length on the network was 50 m, and the maximum link length on the network was 2932 m. The jam density on the network was equal to 160 (veh/km/lane). The performance of the NB controller was compared to the operation of PSC and PSCO con-

trollers to serve as a reference for the evaluation of the proposed decentralized controller's performance. The average of each of the following measures of effectiveness (MOEs) was calculated to assess the NB controller's performance: total delay, travel time, stopped delay, queue length, fuel consumption, and emission levels. In the simulations, vehicles could enter the links for an hour, and the simulation ran for an extra time past that hour to guarantee that all vehicles departed the network. The INTEGRATION microscopic traffic simulation software was used to model the network, shown in Figure 6.1. Three experiments were conducted on the BB network, as discussed in the following sections.

6.1.2 BB Experimental Results: 1

In this experiment the performance of the NB controller was compared to PSC and PSCO controllers. The threat point (d) values per lane for the NB controller were assigned based on the link's lengths (L), the link's free-flow speeds (U_f), and the updating time intervals (Δt), using the following formula; d=min[N(L/2), N($U_f \times \Delta t$)], where N(L/2) represents the number of vehicles that could be accumulated up to the half length of the link, and N($U_f \times \Delta t$) represents the number of vehicles that could be accumulated up to the distance of ($U_f \times \Delta t$). Using the distance of $U_f \times \Delta t$ allowed detected vehicles to pass the intersection without stopping if there was no queue in front of them, where L/2 was used instead of L to get a better estimate of the queue length for each movement, where drivers usually moved to the appropriate lanes as they got closer to the signalized intersection, and to avoid being fully queued (i.e., players will accept a fully occupied (queued) link).

The average MOEs values over the entire simulation time for PSC, PSCO and NB controllers are shown in Table 6.1. In addition, Table 6.1 shows the percent improvement in MOEs using the proposed NB controller over PSC and PSCO controllers.

Simulation results indicated significant reduction in the average total delay of 16.5%, a reduction in the average stopped delay of 40.3%, and a reduction in the average travel time of 5.25%, over the PSC controller. In addition, the results indicated significant reduction in

Table 6.1: Average MOEs and (%) improvement using NB over PSC and PSCO controllers

MOE \ System	PSC	PSCO	NB
Average Total Delay (s/veh)	96.234	100.197	80.323
Improvement %	16.534	19.823	
Average Stopped Delay (s/veh)	20.285	25.649	12.1074
Improvement %	40.314	52.7962	
Average Travel time (s)	306.254	310.225	290.175
Improvement %	5.250	6.463	
Average Number of Stops	4.662	4.5899	4.281
Improvement %	8.18	6.734	
Average Fuel (L)	0.4142	0.4129	0.40
Improvement %	3.38	3.07	
Average CO2 (grams)	913.833	912.495	883.127
Improvement %	3.36	3.22	

the average total delay of 19.8%, a reduction in the average stopped delay of 52.7%, and a reduction in the average travel time of 6.5%, over the PSCO controller. These results show that the proposed NB controller outperforms both the PSC and PSCO controller.

6.1.3 BB Experimental Results: 2

This section presents a potential solution to better estimate the queue length considering the driver's behavior of lane changing close to the intersections. A suggested phasing scheme, shown in Figure 6.2(b), where all vehicles on the link discharge during a single phase, might provide a better estimate of the queue length per phase over the currently implemented phase scheme shown in Figure 6.2(a), where each link discharges in two phases.

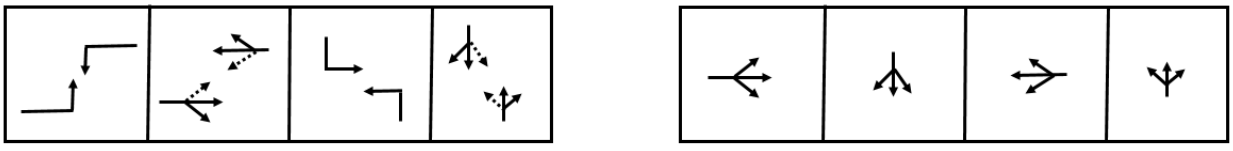

(a) Implemented phasing scheme.

(b) Suggested phasing scheme.

Figure 6.2: Four phasing scheme.

Two simulations were conducted using the NB controller to evaluate the effectiveness of the two phasing scheme on the MOEs, where the threat point per lane was assigned using the following formula: d=min[N(L/2), N($U_f \times \Delta t$)]. The simulation results of using the two schemes (Figure 6.2(b), 6.2(a)) are shown in Table 6.2.

Table 6.2: MOEs using two different phasing schemes

MOE \ System	NB (Imp. Scheme)	NB (Sug. Scheme)	Imp. (%)
Average Total Delay (s/veh)	80.323	94.712	-17.913
Average Stopped Delay (s/veh)	12.107	24.381	-101.374
Average Travel Time (s)	290.175	302.425	-4.222
Average Number of Stops	4.281	4.417	-3.177
Average Fuel (L)	0.40	0.41	-2.274
Average CO_2 (grams)	883.127	902.277	-2.168

The simulation results show that the suggested phasing scheme does not improve the network performance.

6.1.4 BB Experimental Results: 3

The minimum free-flow speed on the network was 30 (km/h), and the maximum free-flow speed on the network was 105 (km/h), with updating time intervals of 10 s. Assigning the detectors locations to be the min(L/2, $U_f \times \Delta t$), the detectors could be located for long links between 84 m (i.e., 13 veh/lane) to 292 m (i.e., 47 veh/lane). Employing the free-flow speed to determine the disagreement point (d=min[N(L/2), N($U_f \times \Delta t$)]) is a good choice for low traffic demand, as vehicles are not to stop at the intersection); however, for high traffic demand, long links can accommodate long queue, which causes delays for the vehicles on that link.

Hence, reducing the number of vehicles that can accumulate in a lane might enhance the network's performance. To examine the effectiveness of changing the maximum number of vehicles that could be accumulated per lane on the MOEs, a sensitivity analysis was con-

ducted, as shown in Figure 6.3, with d=min[N(L/2), NV], where NV presents the maximum number of vehicles that can accumulate in a lane; this number ranges between 6 to 32 vehicles.

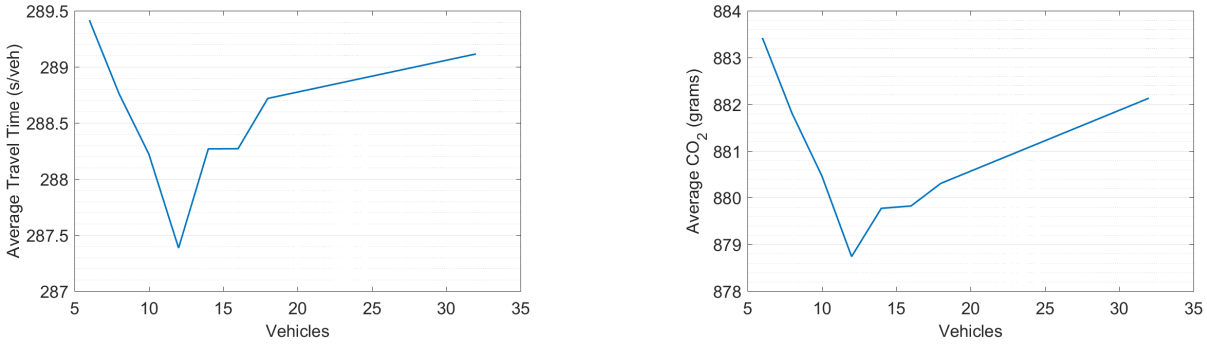

(a) Average travel time.

(b) Average CO_2.

Figure 6.3: Sensitivity analysis.

Analysis of the results in Figure 6.3 demonstrates that better performance using the NB controller could be achieved if the threat points are assigned as a minimum of 12 veh/lane and the number of vehicles that could be accumulated is L/2, (d=min[N(L/2), 12]).

Table 6.3 shows the average MOEs values over the entire simulation time and the percent improvement in MOEs using the proposed NB controller over PSC and PSCO controllers.

Simulation results indicate significant reduction in the average total delay of 19.38%, a reduction in the average stopped delay of 51.18%, a reduction in the average travel time of 6.162%, a reduction in the average number of stops of 8.39%, a reduction in the average fuel consumption of 3.89%, and a reduction in the emission levels of 3.84%, over the PSC controller. The results show that the proposed NB approach outperforms both the PSC and PSCO controllers.

To further investigate the achieved improvements using the NB controller, it was taken into consideration that the network has 459 stop signs and 30 yield signs, which might conceal the full degree of improvement achieved using the NB controller on the signalized intersection. Accordingly, we investigated the percent improvement in MOEs using the NB controller

Table 6.3: Average MOEs and (%) improvement using NB over PSC & PSCO controllers

MOE \ System	PSC	PSCO	NB
Average Total Delay (s/veh)	96.234	100.197	77.577
Improvement %	19.3871	22.575	
Average Stopped Delay (s/veh)	20.285	25.649	9.903
Improvement %	51.182	61.391	
Average Travel Time (s)	306.254	310.225	287.384
Improvement %	6.162	7.362	
Average Number of Stops	4.662	4.5899	4.271
Improvement %	8.393	6.95	
Average Fuel (L)	0.4142	0.4129	0.3981
Improvement %	3.887	3.584	
Average CO2 (grams)	913.833	912.495	878.739
Improvement %	3.84	3.7	

over the PSC controller over only the links that were directly associated with intersections. Table 6.4 shows the percent improvement in MOEs using the NB controller over the PSC controller on the 38 intersections.

Table 6.4 demonstrates an improvement in the travel time on the intersections between 6% to 52%, an improvement in the queue length on the intersections between 8% to 60%, and an improvement in the number of stops on the intersections between 8% to 80%. In addition, Table 6.4 demonstrates an overall reduction in the average travel time of 23.63%, in the average queued vehicles of 37.66%, in the average number of stops of 23.58%, in the average fuel consumption of 10.44%, in the average CO_2 emitted of 9.84%, and in the average No_x emitted of 5.4% over the PSC controller. These results reveal that the NB controller performs significantly better than the PSC controller.

Table 6.4: Intersections (%) improvement of MOEs using NB over PSC controller

MOEs / Int. #	Travel Time	Queue	Num. of Stops	CO_2	Fuel	No_x
1	6.153	22.015	24.311	2.645	2.566	0.161
2	16.409	26.801	21.184	7.706	7.710	5.859
3	8.485	18.233	32.777	6.034	6.450	9.040
4	31.114	52.874	39.564	8.166	6.595	8.756
5	22.230	53.875	52.914	9.355	8.962	3.309
6	23.176	34.435	14.240	11.594	10.716	4.751
7	8.967	15.881	17.832	3.889	3.597	2.271
8	24.057	41.868	16.114	13.753	13.480	9.162
9	40.709	56.267	29.850	25.253	24.654	13.842
10	13.395	26.346	41.436	8.634	8.653	9.772
11	17.628	26.340	11.802	9.014	8.353	1.352
12	7.642	7.968	32.650	3.481	3.373	3.476
13	19.414	37.909	20.915	8.991	8.745	3.758
14	28.503	35.499	25.359	7.854	6.617	8.147
15	23.870	39.630	34.584	12.553	12.272	6.166
16	27.552	59.095	41.876	15.109	14.785	8.836
17	42.001	60.000	56.974	16.896	14.827	12.842
18	26.258	49.883	32.723	14.491	13.414	5.703
19	19.676	36.533	21.104	4.963	4.253	4.976
20	52.237	76.083	63.088	32.966	31.762	20.159
21	34.822	50.159	46.265	21.568	21.385	18.268
22	38.267	59.396	37.466	27.628	27.284	26.528
23	17.193	30.863	16.272	7.595	6.922	5.258
24	34.669	43.997	11.269	14.632	13.342	3.239
25	23.480	44.588	57.381	5.760	4.502	0.085
26	18.029	26.028	30.503	4.017	2.478	0.750
27	28.129	36.340	8.565	16.769	16.194	14.480
28	14.530	35.046	11.902	9.459	9.846	11.611
29	13.131	19.115	9.603	5.347	4.985	1.142
30	23.632	47.382	23.224	19.330	19.409	24.772
31	32.761	55.701	80.381	18.004	17.273	19.333
32	34.761	53.070	35.456	26.641	27.045	29.311
33	35.984	48.472	15.256	20.348	19.563	11.668
34	16.679	32.676	30.335	11.273	11.151	11.757
35	18.012	28.950	21.575	18.241	18.672	26.116
36	22.588	46.509	34.331	7.676	7.028	2.465
37	29.307	46.502	31.486	7.399	6.678	1.081
38	14.317	14.552	8.061	4.669	4.168	1.143
Overall (%)	23.633	37.666	23.586	10.444	9.842	5.390

6.2 Downtown Los Angles Experiments

6.2.1 Los Angles Experimental Setup

These experiments were large scale studies of a network in downtown Los Angles (LA), California, including the most congested downtown area, as shown in Figure 6.4. Simulations were conducted during the morning peak hour ($7-8$ a.m.) [107]. The downtown LA network has 457 signalized intersections, 285 stop signs, 23 yield signs, and 3556 links. The origin-destination (O-D) demand matrices were generated using the QueensOD software [105] with 143957 trips. The phasing scheme varied from 2 to 6 phases, reflecting the intersections phases implemented in downtown LA. The minimum free-flow speed on the network was 15 (km/h), and the maximum free-flow speed on the network was 120 (km/h). The minimum link length on the network was 50 m, and the maximum link length on the network was 4400 m. The jam density on the network was equal to 180 (veh/km/lane).

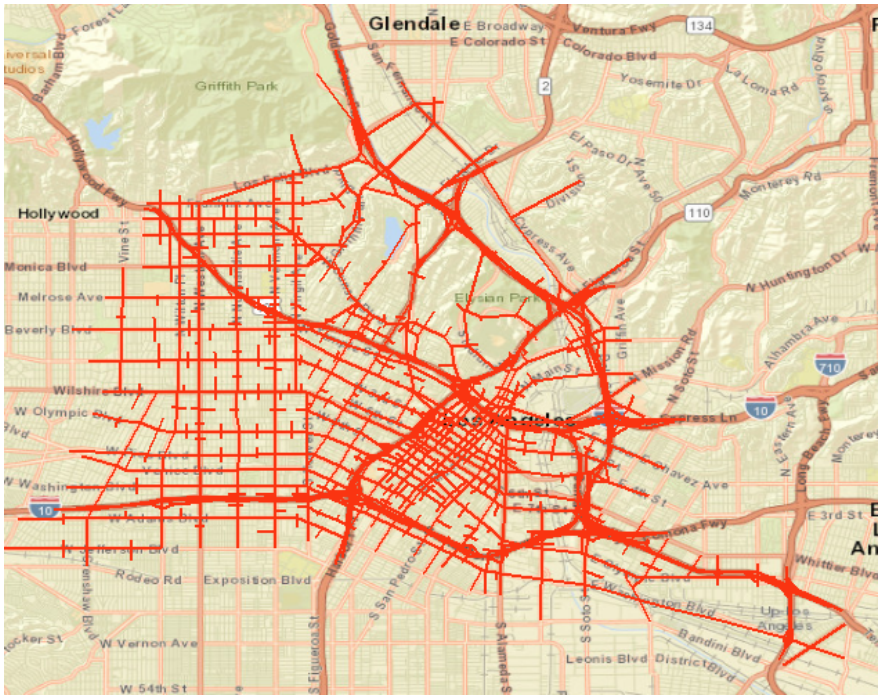

Figure 6.4: Downtown Los Angles, Google maps.

The NB controller was compared to the PSC controller to evaluate their relative performance. The average of each of the following measures of effectiveness (MOEs) was calculated to assess the performance of the NB controller: total delay, travel time, stopped delay, queue length, fuel consumption, and emission levels. In the simulations, vehicles could enter the links for an hour, with extra time at the end of the simulation to guarantee that all vehicles departed the network. The INTEGRATION microscopic traffic simulation software was used to model the network, as shown in Figure 6.5.

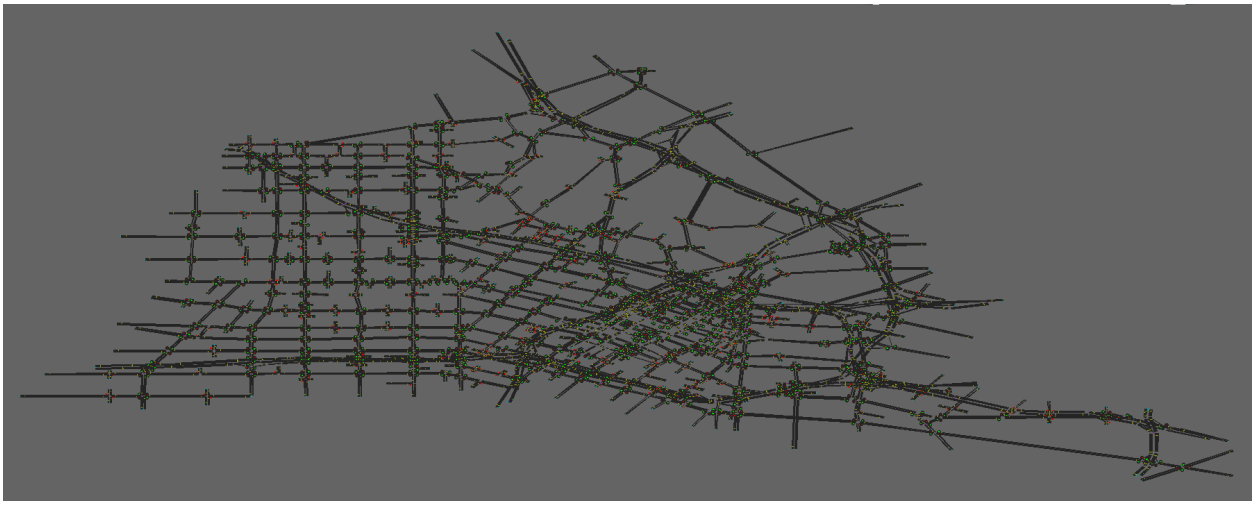

Figure 6.5: INTEGRATION, Los Angles network.

6.2.2 LA Experimental Results: 1

In this experiment, the performance of the NB controller was compared to that of the PSC controller using the full demand in the morning peak hour. The threat point per lane for the NB controller was assigned as the minimum of 12 veh/lane and the number of vehicles that could be accumulated on L/2 (i.e., d=min[N(L/2), 12]) based on the sensitivity analysis shown in Figure 6.6.

The average MOEs values over the entire simulation time for PSC and NB controllers are shown in Table 6.5. In addition, Table 6.5 shows the percent improvement in MOEs using the proposed NB controller over the PSC controller. Simulation results indicated significant

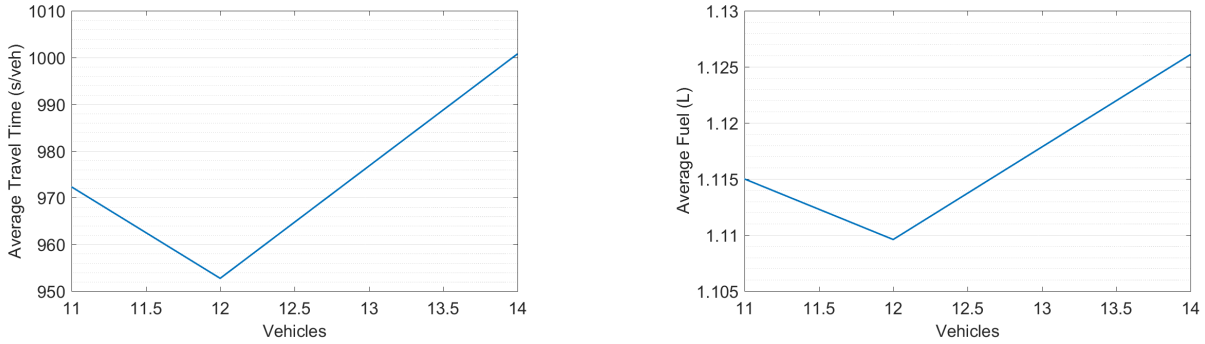

(a) Average Travel Time.

(b) Average Fuel Consumption.

Figure 6.6: LA Sensitivity Analysis.

reduction in the average total delay of 14.55%, a reduction in the average stopped delay of 25.18%, a reduction in the average travel time of 7.89%, a reduction in the average number of stops of 12.4%, a reduction in the average fuel consumption of 4.0%, and a reduction in the emission levels of 4.25%, for the NB over the PSC controller. Analysis of the results demonstrates that the proposed NB controller approach outperforms the PSC controller.

Table 6.5: Average MOEs and the (%) improvement using NB controller over PSC controller (100% Demand)

System / **MOE**	PSC	NB	NB Imp. (%)
Average Total Delay (s/veh)	557.463	476.346	14.55
Average Stopped Delay (s/veh)	256.766	192.116	25.178
Average Travel Time (s)	1034.27	952.732	7.89
Average Number of Stops	7.406	6.487	12.4
Average Fuel (L)	1.155	1.109	4.0
Average CO_2 (grams)	2482.13	2376.59	4.25

To further investigate the achieved improvements using the NB controller, it was taken into consideration that the network has 285 stop signs, 23 yield signs, which might conceal the full degree of improvement achieved using the NB controller on the signalized intersection. Accordingly, we investigated the percent improvement in MOEs using the NB controller over the PSC controller over only the links that were directly associated with intersections. Table 6.6.

Table 6.6 demonstrates a reduction in the average travel time of 35.16%, a reduction in the average queued vehicles of 54.67%, a reduction in the average number of stops of 44.03%, a reduction in the average fuel consumption of 9.97%, a reduction in the CO_2 emitted of 9.92%, and a reduction in the NOX emitted of 11.78% over the PSC controller. These results reveal that the NB controller has significantly better performance potential than PSC controller.

Table 6.6: Average (%) improvements of MOEs using NB controller over PSC controller (100% Demand), over the links that are directly associated with intersections

MOEs / Int. #	Travel time	Queue	Num. of Stops	CO_2	Fuel	Nox
Overall 457 Int. (%)	35.156	54.669	44.031	9.966	9.919	11.774

6.2.3 LA Experimental Results: 2

To further investigate performance potential using the NB controller, a simulation was conducted at lower traffic conditions (i.e., 10% of the peak demand).

Table 6.7 shows a reduction in the average total delay of 36.79%, a reduction in the average stopped delay of 90.26%, a reduction in the average travel time of 7.1%, a reduction in the average number of stops of 34.66%, a reduction in the average fuel consumption of 4.8%, and a reduction in the emission levels of 4.79%, over PSC controller.

Table 6.7: Average MOEs and the (%) improvement using NB over PSC controller (0.1% Demand)

System / MOE	PSC	NB	NB Imp. (%)
Average Total Delay (s/veh)	84.938	53.689	36.79
Average Stopped Delay (s/veh)	19.971	1.9451	90.261
Average Travel Time (s)	450.114	418.177	7.1
Average Number of Stops	4.475	2.924	34.66
Average Fuel (L)	0.846	0.805	4.8
Average CO_2 (grams)	1830.27	1742.53	4.79

Once more, To further investigate the achieved improvements using the NB controller, it was

taken into consideration that the network has 285 stop signs, 23 yield signs, which might conceal the full degree of improvement achieved using the NB controller on the signalized intersection. Accordingly, we investigated the percent improvement in MOEs using the NB controller over the PSC controller over only the links that were directly associated with intersections at a lower demand, as shown in Table 6.8.

Table 6.8 demonstrates a reduction in the average travel time of 19.19%, a reduction in the average queued vehicles of 49.84%, a reduction in the average number of stops of 53.71%, a reduction in the average fuel consumption of 54.16%, a reduction in the average CO_2 emitted of 16.09%, and a reduction in the average NOX emitted of 25.94% over PSC controller. These results reveal that the NB controller performed significantly better than the PSC controller as the traffic demand decreased.

Table 6.8: Average (%) improvements of MOEs using NB over PSC controller (0.1% Demand) over the links directly associated with intersections

MOEs / Int. #	Travel time	Queue	Num. of Stops	CO_2	Fuel	NO_x
Overall 457 Int. (%)	19.186	49.844	53.708	54.158	16.085	25.939

The results show that the NB controller yielded significant improvements in the average values of all MOEs, indicating improved system efficiency.

6.3 Summary

In this chapter the developed NB de-centralized, cycle-free, flexible phasing traffic signal controller was applied and evaluated on large scale networks. The INTEGRATION microscopic traffic assignment and simulation software was used to evaluate the performance of the proposed controller relative to a decentralized phase split and cycle length optimization controller, and a fully-coordinated adaptive phase split, cycle length and offset optimization controller, in the town of Blacksburg, Virginia, and in downtown Los Angles, California.

Several simulations were conducted on the Blacksburg network using different threat point values and phasing schemes to determine their effect on the controller's performance. The results show significant reductions on the network in the average total delay of 19.3% and 22.6%, a reduction in the stopped delay of 51% and 61%, a reduction in the average travel time of 6.1% and 7.3%, and a reduction in the emission levels of 3.8% and 3.7%, over PSC and PSCO controllers, respectively. In addition, the results show significant reductions on the intersections links in the average travel time of 23.6%, a reduction in the average queue length of 37.6%, a reduction in the average number of stops of 23.6%, a reduction in the Co_2 emitted of 10.4%, a reduction in the fuel consumption of 9.8%, and a reduction in NO_X emitted of 5.4%.

In addition, the NB controller's performance was tested in downtown Los Angles, California, and compared to the performance of a PSC controller. The results show significant reductions on the network in the average total delay of 14.5%, a reduction in the stopped delay of 25.1%, a reduction in the average travel time of 8%, a reduction in the average number of stops of 12.4% and a reduction in the Co_2 emitted of 4.25%, over the PSC controller. Moreover, the results show significant reductions at the intersections links in the average travel time of 35.1%, a reduction in the average queue length of 54.7%, a reduction in the average number of stops of 44%, a reduction in the Co_2 emitted of 10%, a reduction in the fuel consumption of 10%, and a reduction in NO_X emitted of 11.7%. Furthermore, simulations conducted at lower traffic flow conditions showed significant reductions on the network in the average total delay of 36.7%, a reduction in the stopped delay of 90.2%, and a reduction in the average number of stops of 35% over thePSC controller. As these results indicate, the NB controller can generate major performance improvements at lower demands.

The results demonstrate significant potential benefits of using the proposed controller over other state-of-the-art centralized and de-centralized controllers on large scale networks.

Chapter 7

Summary, Conclusions, and Future Research

This chapter summarizes the main findings of the research presented in this dissertation and discusses recommendations for future work.

7.1 Summary & Conclusions

Traffic growth constrained by available capacity in urban areas affects traveler mobility, air quality, and public health. Reducing traffic congestion can improve these conditions while simultaneously decreasing transportation-related energy use. The first objective in the dissertation is to investigate the spatial relationship between air quality and traffic flow patterns. To achieve this objective a source localization strategy to identify the source location (correlated with traffic flow) of an airborne contaminant (soot) in a turbulent wind field was developed. Simulation studies were conducted to demonstrate relative strengths and weaknesses of source localization strategies, these simulations were preliminary steps toward the planned experiment. Consequently, an experimental investigation based on real

flow conditions was conducted to estimate the source location of the aerosol (soot), that can be attributed to traffic. In the experiment a light detection and ranging (LiDAR) system was deployed to measure aerosol vertical profiles. The results showed that the primary source of harmful soot aerosol that is emitted by vehicles is at intersections and is due to congestion.

Therefore, to enhance the air quality, optimizing the utilization of the available infrastructure using advanced traffic signal controllers is necessary to mitigate traffic congestion and emissions in a world with growing pressure on financial and physical resources. The second objective in this dissertation is to mitigate traffic congestion at signalized intersections. Hence, we developed a novel de-centralized traffic signal optimization controller, considering a flexible phasing sequence and free cycle length, using a Nash bargaining (NB) game-theoretic framework. This section summarizes the main findings of the research presented in this dissertation.

Chapter 1 described the problem, the research objective, the methodology, the contribution, and the dissertation roadmap. It also highlighted the major limitations of existing approaches.

Chapter 2 presented the necessary background, definitions, an overview, and synthesis of the literature of state-of-the-practice and state-of-the-art traffic signal controllers. In addition, it summarized the major challenges and limitations in the literature.

Chapter 3 described the formulation of the source localization problem, and presented the results for estimating the aerosol location in simulations and using in-field measurements, to investigate the spatial relationship between air quality and traffic flow patterns.

First, the problem was formulated and addressed in a simulation environment. Simulation studies were conducted to demonstrate relative strengths and weaknesses of source localization strategies; these simulations were preliminary steps toward the field experiment. The plume, which served as the basis for comparison, was generated using the turbulent atmospheric flow simulation TurbSim to propagate a contaminant plume employing an atmospheric dispersion model proposed in the literature. The location of the plumes source

was estimated using three algorithms: a recursive Bayesian estimation algorithm, a gradient descent algorithm, and an extended Kalman filter algorithm. The simulation results showed that the Bayesian estimation algorithm requires minimal modeling assumptions, and moreover that the source strength and the wind statistics were not needed. In contrast, the estimation results using the gradient descent algorithm or the extended Kalman filter are affected by the choice of the initial conditions and by the contaminant plume dispersion model. Simulation results suggested that the Bayesian estimation algorithm is an effective strategy for estimating the source location.

Second, an experimental investigation in real conditions was conducted to identify the possible source location (correlated with traffic flow) of an airborne contaminant (soot, which was attributed to traffic), using a Bayesian estimation algorithm in the vicinity of the ODU campus. In the experiments, LiDAR was employed to collect data of aerosol profiling in the atmosphere at several sites at the ODU campus. The results showed that the primary source of harmful soot aerosol emitted by vehicles is at intersections and is due to congestion, which demonstrates that air quality is correlated with traffic flows and congestion caused by signalized intersections.

Accordingly, to enhance the air quality and alleviate congestion, optimizing the performance of available infrastructure via advanced traffic signal controllers has become increasingly appealing. Traffic signal controllers attempt to optimize various traffic variables (e.g., delay, queue length, and energy and emission levels) by optimizing signal control variables, including the cycle length, the phasing scheme and sequence, the phase split, and the offset.

Chapter 4 presented a novel de-centralized traffic signal controller, achieved using a Nash bargaining (NB) game-theoretic framework, and using a cycle-free and flexible phasing sequence, to adjust to changes in traffic conditions. The NB algorithm is used to optimize the signal timings at each signalized intersection by modeling each phase as a player in a game, where players cooperate to reach a mutually agreeable outcome. Decentralized systems are scalable and easy to expand by inserting new controllers into the system. Additionally, de-

centralized systems are often inexpensive to establish and operate, as there is no essential need for a reliable and direct communication network between a central computer and the local controllers in the field.

The INTEGRATION microscopic traffic assignment and simulation software was used to evaluate the performance of the algorithm relative to an optimum fixed-time plan (FP) and an actuated (ACT) controller on a major intersection in downtown Toronto, considering different traffic demand levels, and using observed traffic data. Several simulations were conducted using NB controller with different update time intervals and different threat point values to study the effect of these parameters on the controller's performance. The experimental results using the NB controller showed that, using relatively short updating time interval, it is possible to minimize delay and maximize traffic flow efficiency. To evaluate the benefits of using the proposed controller, three scenarios were simulated using the three controllers at different traffic demand levels.

The results showed significant reductions in the average total delay ranging from 41% to 64%, a reduction in the average queue length ranging from 58% to 77%, a reduction in the emission levels ranging from 6% to 17%, a reduction in the average travel time ranging from 37% to 65%, and a reduction in the network clearance time ranging from 1% to 12%. To further investigate the achieved improvements using the NB approach, simulations were conducted at different flow ratios.

The simulation results demonstrated a significant potential for the NB controller over FP and ACT controllers. Moreover, the results show that major improvements are achievable using the NB controller regardless of the traffic demand level.

Chapter 5 described the de-centralized mechanism of the NB controller and how it could be applied on a network of multi-intersections. In addition, it demonstrated the experimental setup and the simulation results of applying the proposed control approach on an arterial network in downtown Blacksburg, VA composed of six intersections.

The INTEGRATION microscopic traffic assignment and simulation software was used to

evaluate the performance of the proposed controller relative to an optimum fixed-time coordinated plan (FP), a centralized adaptive phase split controller (PS), a decentralized phase split and cycle length optimization controller (PSC), and a fully-coordinated adaptive phase split, cycle length and offset optimization controller(PSCO).

A total of 30 random seed simulations were conducted for the five controllers. The results showed significant reductions in the average queue length, in the average total delay ranging from 36% to 67%, a reduction in the emission levels ranging from 6% to 13%, a reduction in the average travel time ranging from 7% to 21%, and a reduction in the network clearance time. Analysis of variance tests, Tukey tests, and pairwise comparison tests were conducted to validate the benefits of using the proposed controller (NB), and the results showed that the NB controller produces statistically significant major improvements over other state-of-the-art centralized and de-centralized control approaches.

Chapter 6 presented how the developed NB de-centralized cycle-free with flexible phasing traffic signal controller was applied and evaluated on large scale networks. The INTEGRATION microscopic traffic assignment and simulation software was used to evaluate the performance of the proposed controller relative to a decentralized phase split and cycle length optimization controller, and a fully-coordinated adaptive phase split, cycle length and offset optimization controller, in the town of Blacksburg, Virginia, and in downtown Los Angles, California.

Several simulations were conducted on the Blacksburg network using different threat point values and phasing schemes to determine their effect on the controller's performance. The results showed significant reductions on the network in the average total delay of 19.3% and 22.6%, a reduction in the stopped delay of 51% and 61%, a reduction in the average travel time of 6.1% and 7.3%, and a reduction in the emission levels of 3.8% and 3.7%, over the PSC and PSCO controllers, respectively. In addition, the results showed significant reductions at the intersections links in the average travel time of 23.6%, a reduction in the average queue length of 37.6%, a reduction in the average number of stops of 23.6%, a reduction in the Co_2

emitted of 10.4%, a reduction in fuel consumption of 9.8%, and a reduction in NO_X emitted of 5.4%.

In addition, the NB controller's performance was tested on the downtown Los Angles, California network and compared to the performance of a PSC controller. The results showed significant reductions on the network in the average total delay of 14.5%, a reduction in the stopped delay of 25.1%, a reduction in the average travel time of 8%, a reduction in the average number of stops of 12.4% and a reduction in the Co_2 emitted of 4.25%, over the PSC controller.

Moreover, the results showed significant reductions on the intersections links in the average travel time of 35.1%, a reduction in the average queue length of 54.7%, a reduction in the average number of stops of 44%, a reduction in the Co_2 emitted of 10%, a reduction in the fuel consumption of 10%, and a reduction in NO_X emitted of 11.7%. Furthermore, simulations were conducted at lower traffic flow and showed significant reductions on the network in the average total delay of 36.7%, a reduction in the stopped delay of 90.2%, a reduction in the average number of stops of 35%, over the PSC controller, indicating that the NB controller can generate major performance improvements at lower demands.

The results showed significant potential benefits of using the proposed controller over other state-of-the-art centralized and de-centralized controllers on large scale networks.

This dissertation presented a source localization strategy to identify the possible source location (correlated with traffic flow) of an airborne contaminant (i.e., attributed to traffic). In addition, it presented a novel traffic signal controller that is able to adapt signal plans based on the observed traffic state without using historical data. The developed control system is de-centralized, which will increase both its scalability and robustness. The proposed controller was evaluated on traffic scenarios that represent those found in the real-world, which ensures that the controller is applicable to real situations. The proposed controller is capable of alleviating congestion as well as reducing emissions and enhancing air quality.

7.2 Recommendations For Future Research

As with any piece of work, further efforts are needed. Subsequent work is recommended in the following areas:

In this research, transit vehicles were treated as regular cars. However, future work could consider person delay as opposed to vehicle delay in the optimization logic. In other words, to give priority to high occupancy vehicles, as they carry more travelers.

The performance of the developed controller is affected by the estimated and predicted queue lengths at the different intersection approaches. To better estimate the queue length a vehicle-to-infrastructure (V2I) communication system could be employed to enhance the operation of the proposed controller, where vehicles can share their direction of travel and thus queues can be estimated more accurately.

The performance of the proposed controller versus other controllers could be investigated for non-recurring traffic congestion conditions (e.g., incidents, special events, or inclement weather conditions).

The proposed de-centralized controller could be compared to a network fundamental diagram (NFD) based traffic signal controller.

The proposed controller could be integrated with a traffic router to develop a fully-integrated traffic controller.

Bibliography

[1] H. Ishida, T. Nakamoto, and T. Moriizumi. Remote sensing of gas/odor source location and concentration distribution using mobile system. *Sensors and Actuators*, 49:52–57, October 1998.

[2] Cebr. The future economic and environmental costs of gridlock in 2030. Technical report, Center for Economics and Business Research, July 2014.

[3] R. Rozas, J. Morales, and D. Vega. Artificial smell detection for robotic navigation. In *The 5th International Conference on Advanced Robotics*, volume 2, pages 1730–1733, Pisa, Italy, June 1991.

[4] A. Lilienthal, D. Reimann, and A. Zell. Gas source tracing with a mobile robot using an adapted moth strategy. In *Proceedings of Autonomous Mobile Systems*, pages 150–160, 2003.

[5] S. Pang and J. A. Farrell. Chemical plume source localization. *IEEE Transactions on Systems, Man, and Cybernetics, Part B: Cybernetics*, 36:1083–1119, October 2006.

[6] Y. Dai, D. Zhao, and Z. Zhang. Computational intelligence in urban traffic signal control: A survey. *IEEE Transactions on Systems, Man, and Cybernetics*, 42(4):485–494, July 2012.

[7] C. Daganzo. *Fundamentals of Transportation and Traffic Operations*. Emerald Group, 1997.

[8] A. M. Turky, M. S. Ahmad, M. Yusoff, and B. T. Hammad. Using genetic algorithm for traffic light control system with a pedestrian crossing. In *4th International Conference, RSKT*, Gold Coast, Australia, July 2009.

[9] X. Yang. Comparison among computer packages in providing timing plans for iowa arterial in lawrence, kansas. *Journal of Transportation Engineering*, 127:311–318, 2001.

[10] R. P. Roess, E. S. Prassas, and W. R. McShane. *Traffic Engineering - Fourth Edition*. Pearson Prentice Hall, 2010.

[11] L. J. French and M. S. French. Benefits of signal timing optimization and its to corridor operations. Technical report, French Engineering, LLC, August 2006.

[12] P. B. Hunt, D. I. Robertson, R. D. Bretherton, and R. I. Winton. Scoot-a traffic responsive method of coordinating signals. Technical report, Transport and Road Research Laboratory, 1981.

[13] A. G. Sims and K. W. Dobinson. Scat-the sydney co-ordinated adaptive traffic systemphilosophy and benefits. *International Symposium on Traffic Control Systems*, 1979.

[14] K. L. Head, P. B. Mirchandani, and D. Sheppard. Hierarchical framework for real-time traffic contro. *Transportation Research Record*, 1360:82–88, 1992.

[15] N. H. Gartner. Opac: A demand-responsive strategy for traffic signal control. *Transportation Research Record: Journal of the Transportation Research Board*, 906:75–81, 1983.

[16] M. R. Evans. Balancing safety and capacity in an adaptive signal control system - phase 1. Technical report, OFederal Highway Administration, October 2010.

[17] B. J. Jonkman and L. Kilcher. Turbsim user's guide. Technical Report Version 1.06.00, A national laboratory of the U.S. Department of Energy, office of energy efficiency and renewable energy, September 2012.

[18] J. A. Farrell, J. Murlis, X. Long, W. Li, and R. T. Carde. Filament-based atmospheric dispersion model to achieve short time-scale structure of odor plumes. *Environmental Fluid Mechanics*, 2:143–169, June 2002.

[19] S. Tantawy, B. Abdulhai, and H. Abdelgawad. Multiagent reinforcement learning for integrated network of adaptive traffic signal controllers. In *IEEE transactions on intelligent transportation systems*, 2013.

[20] J. Chen. Game-theoretic formulations of interaction between dynamic traffic control and dynamic traffic assignment. *Transportation Research Record*, 1617:179–188, 1998.

[21] M. Elhenawy, A. A. Elbery, A. A. Hassan, and H. A. Rakha. An intersection game-theory-based traffic control algorithm in a connected vehicle environment. In *IEEE 18th International Conference on Intelligent Transportation Systems*, pages 343–347, Washington, DC, USA, 2015.

[22] L. Jun. Study on game-theory-based integration model for traffic control and route guidance. In *Tian Jin University.*, 2003.

[23] Z. Han, D. Niyato, W. Saad, T. Basar, and A. Hjorungnes. *Game Theory in Wireless and Communication Networks: Theory, Models, and Applications.* Cambridge University Press, New York, 2012.

[24] G. Lai, C. Li, K. Sycara, and J. Giampapa. Literature review on multi-attribute negotiations. Technical report, Carnegie Mellon University, Robotics Institute, December 2004.

[25] H. Park and M. van. Bargaining strategies for networked multimedia resource management. *IEEE Transactions on Signal Process*, 55:496–3511, 2007.

[26] Z. Han and K. J. R. Liu. Fair multiuser channel allocation for ofdma networks using nash bargaining solutions and coalitions. *Communications, IEEE Transactions*, 53:1366–1376, August 2005.

[27] Z. Zhang, H. Hwa Chen, M. Guizani, and P. Qiu. A cooperation strategy based on nash bargaining solution in cooperative relay networks. *Vehicular Technology, IEEE Transactions*, 57:2570–2577, July 2008.

[28] P. A. Grout. Investment and wages in the absence of binding contracts: A nash bargaining approach. *Econometrica: Journal of the Econometric Society*, pages 449–460, 1984.

[29] I. M. McDonald and R. M. Solow. Wage bargaining and employment. *The American Economic Review*, pages 896–908, 1981.

[30] E. Larsson and E. Jorswieck. Competition versus cooperation on the miso interference channel. *IEEE Journal on Selected Areas in Communications*, 26:1059–1069, 2008.

[31] M. Van Aerde and H. A. Rakha. Realtran: An off-line emulator for estimating the impacts of scoot. *Transportation Research Record*, (1494):124–128, 1995.

[32] H. A. Rakha, M. Van Aerde, and E.R. Experiments in incremental real-time optimization of phase, cycle, and offset times using an on-line adaptation of transyt-7f. In *Engineering Foundation Conference on Traffic Management: Issues and Techniques*, Palm Coast, Florida, April 1991.

[33] M. Van Aerde and Hesham A. Rakha. Integration release 2.40 for windows: User's guide-volume ii: Advanced model features. Technical report, June 2013.

[34] H. A. Rakha. *A Simulation Approach for Modeling Real-Time Traffic Signal Controls*. Department of Civil Engineering, Queen's University, 1993.

[35] L. J. French and M. S. French. Benefits of signal timing optimization and its to corridor operations. Technical Report FHWAPA-2006-007-040214-P1, The Pennsylvania Department of Transportation Bureau of Planning and Research, August 2006.

[36] R.D. Henry. Signal timing on a shoestring. Technical Report FHWA-HOP-07-006, Office of Travel Management Federal Highway Administration, March 2005.

[37] Y. Shoham, R. Powers, and T. Grenager. Multi-agent reinforcement learning: A critical survey. Technical report, Computer Science Department, Stanford University, California, US, 2003.

[38] and J. Marchand M. D. Armstrong, J. R. Rhodes, A. MacNab, P. V. Godfrey, and S. Cass. Improved operation of urban transportation systems, volume 1: Traffic signal control strategies a state-of-the-art. Technical report, Ministry of Transport, Canada.

[39] J. MacGowan and I. J. Fullerton. Development and testing of advanced control strategies in the urban traffic control system. *Public Roads*, 43:97105., 1979.

[40] A. Gosavi. Simulation-based optimization: Parametric optimization techniques and reinforcement learning. In *Springer, Netherlands*, pages 1151–1158, 2003.

[41] M. Selinger and l. Schmidt. Adaptive traffic control systems in the united states. Technical report, HDR Engineering, Septamber 2009.

[42] B. Abdulhai, H. Porwal, and W. Recker. Short-term freeway traffic flow prediction using genetically optimized time-delay-based neural networks. In *Transportation Research Board*, Washington D.C., USA, 1999.

[43] D. M. Mukhopadhyay, A. Farkhod M. O. Balitanas, S. H. Jeon, and D. Bhattacharyya. Genetic algorithm:a tutorial review. *International Journal of Grid and Distributed Computing*, 2:25– 32, 2009.

[44] H. Ceylan and M. G. H. Bell. Traffic signal timing optimization based on genetic algorithm approach, including driver's routing. In *Transportation Research Part B*, volume 38, page 329342, 2004.

[45] J. Sanchez, M. Galan, and E. Rubio. Applying a traffic lights evolutionary optimization technique to a real case. *IEEE Transactions on Evolutionary Computation*, 12:25–40, 2008.

[46] H.G. Beyer and H.P. Schwefel. Evolution strategies - a comprehensive introduction. *Natural Computing*, 1:3–25, 2002.

[47] Y.K. Chin, K.C. Yong, N. Bolong, S.S. Yang, and K.T.K. Teo. Multiple intersections traffic signal timing optimization with genetic algorithm. In *IEEE International Conference on Control System, Computing and Engineering*, 2011.

[48] A. Vogel, C. Goerick, and W. V. Seelen. Evolutionary algorithms for optimizing traffic signal operation. In *European Symposium on Intelligent Techniques*, 2000.

[49] Z. Liu. A survey of intelligence methods in urban traffic signal control. *International Journal of Computer Science and Network Security*, 7:105–112, 2007.

[50] H. Ceylan and M. Bell. Traffic signal timing optimisation based on genetic algorithm approach, including drivers' routing. In *Transportation Research Part B Methodology*, May 2004.

[51] L.A. Zadeh. Fuzzy logic: computing with words. *IEEE Transactions on Fuzzy Systems*, 4, 1996.

[52] C. P. Pappis and E. H. Mamdani. A fuzzy logic controller for a traffic junction systems. *IEEE Transactions on Man and Cybernetics*, 7:707–717, 1977.

[53] S. Chiu and S. Chand. Self-organizing traffic control via fuzzy logic. In *32nd IEEE Conference In Decision and Control*, pages 1897–1902, 1993.

[54] E. Bingham. Neurofuzzy traffic signal control. In *Helsinki University of Technology*, 1998.

[55] J.C. Spall and D.C. Chin. A model-free approach to optimal signal light timing for system-wide traffic control. In IEEE, editor, *33rd IEEE Conference on Decision and Control*, number 1868-1875, 1994.

[56] D. Srinivasan, M. C. Choy, and R. L. Cheu. Neural networks for real-time traffic signal control. *IEEE Transactions on Intelligent Transportation Systems*, 7, September 2006.

[57] R. S. Sutton and A. G. Barto. *Reinforcement Learning: An Introduction*. The MIT Press Cambridge, Massachusetts London, England, 2012.

[58] M.A. Wiering, J. Vreeken, J. Van Veenen, and A. Koopman. Simulation and optimization of traffic in a city. *Intelligent Vehicles Symposium*, pages 453–458, 2004.

[59] M.A. Wiering. Multi-agent reinforcement learning for traffic light control. In *Seventeenth International Conference on Machine Learning*, pages 1151–1158, 2000.

[60] B. Abdulhai, R. Pringle, and G. J. Karakoulas. Reinforcement learning for true adaptive traffic signal control. *Journal of Transportation Engineering*, 129:278285, 2003.

[61] A. Salkham, R. Cunningham, A. Garg, and V. Cahill. A collaborative reinforcement learning approach to urban traffic control optimization. In *International Conference on Web Intelligence and Intelligent Agent Technology*, 2008.

[62] M. K. Ekbatani, A. Kouvelas, I. Papamichail, and M. Papageorgiou. Exploiting the fundamental diagram of urban networks for feedback-based gating. *Transportation Research Part B*, page 13931403, 2012.

[63] M. K. Ekbatani, M.s Papageorgiou, and V. L. Knoop. Controller design for gating traffic control in presence of time-delay in urban road networks. *Transportation Research Part C*, pages 308–322, 2015.

[64] K. K. Yit, P. Rajendran, and L. K. Wee. Proportional-derivative linear quadratic regulator controller design for improved longitudinal motion control of unmanned aerial vehicles. *International Journal of Micro Air Vehicles*, pages 41–50, 2016.

[65] N. Hashimoto, U.Ozguner, and N. Sawant. Evaluation of control in a convoy scenario lqr-based sequential state feedback controller. In *IEEE Intelligent Vehicles Symposium*, Baden-Baden, Germany, June 2011.

[66] K. Aboudolas, M. Papageorgiou, and E. Kosmatopoulos. Control and optimization methods for traffic signal control in large-scale congested urban road networks. In *American Control Conference*, New York City, USA, July 2007.

[67] J.P. Crimaldi and J.R. Koseff. Structure of turbulent plumes from a momentum less source in a smooth bed. *Environmental Fluid Mechanics*, 6:573–592, October 2006.

[68] L. Marques, U. Nunes, and A.T. Almeida. Particle swarm-based olfactory guided search. *Autonomous Robots*, 20:277–287, June 2006.

[69] R. Rozas, J.Morales, and D. Vega. Artificial smell detection for robotic navigation. In *5th International Conference on Advanced Robotics*, pages 1730–1733, 1991.

[70] Chemical source location and the robomole project. In *Australasian Conference on Robotics and Automation*, pages 1–6, R. Russell, 2003.

[71] R. Bachmayer and N. Leonard. Vehicle networks for gradient descent in a sampled environment. In *IEEE Conference on Decision and Control*, pages 1–6, 2002.

[72] Q. Zhang, G. Sobelman, and T. He. Gradient-based target localization in robotic sensor networks. In *Pervasive and Mobile Computing*, volume 5, pages 37–48, February 2009.

[73] A. T. Hayes, A. Martinoli, and R.M. Goodman. Distributed odor source localization. *IEEE sensors*, 2:260–271, June 2002.

[74] G. Ferri, E. Caselli, V. Mattoli, A. Mondini, B. Mazzolai, and P. Dario. A biologically-inspired algorithm implemented on a new highly flexible multi-agent platform for gas source localization. In *The First IEEE/RAS-EMBS International Conference on Biomedical Robotics and Biomechatronics*, pages 573–578, February 2006.

[75] X. Cui, T. Hardin, R. K. Ragade, and A. S. Elmaghraby. A swarm-based fuzzy logic control mobile sensor network for hazardous contaminants localization. In *IEEE International Conference on Mobile Ad-hoc and Sensor Systems*, pages 194–203, Octuber 2004.

[76] J. A. Farrell, S. Pang, and W. Li. Plume mapping via hidden Markov methods. *IEEE Transactions on Systems, Man, and Cybernetics, Part B: Cybernetics*, 33:850–863, 2003.

[77] J. Li, Q. Meng, Y. Wang, and M. Zeng. Odor source localization using a mobile robot in outdoor airflow environments with a particle filter algorithm. *Autonomous Robots*, 30:281–292, April 2011.

[78] M. Skliar and W. F.Ramirez. Air-quality monitoring and detection of air contamination in an enclosed environment. *Journal of spacecraft and rockets*, 34, August 1997.

[79] E. Dehghan Niri, A. Farhidzadeh, and S. Salamone. Nonlinear kalman filtering for acoustic emission source localization in anisotropic panels. *Ultrasonics*, 54:486501, February 2014.

[80] H. Sun, P. Yang, H. Sun, and L. Zu. Outliers based double-kalman filter for sound source localization. In *2011 International Conference on Control, Automation and Systems Engineering (CASE)*, pages 1–4, July 2011.

[81] J. M. Stockie. The mathematics of atmospheric dispersion modeling. *Society for industrial and applied mathematics*, 53:349–372, May 2011.

[82] J. T. Foley and T. G. Gutowski. Turbsim: Reliability-based wind turbine simulator. In *IEEE International Symposium on Electronics and the Environment*, pages 1–5, San Francisco, CA, May 2008.

[83] R. Fadaeinedjad, G. Moschopoulos, and M. Moallem. A new wind power plant simulation method to study power quality. In *Canadian Conference on Electrical and Computer Engineering*, pages 1433–1436, Vancouver, BC, April 2007.

[84] H. Abdelghaffar, C. A. Woolsey, , and H. A. Ali. Source localization for a turbulent plume model using bayesian occupancy grid mapping. In *AIAA Guidance, Navigation, and Control Conference*, Kissimmee, Florida, January 2015.

[85] Ferria et al. Mapping multiple gas/odor sources in an uncontrolled indoor environment using a bayesian occupancy grid mapping based method. *Robotics and Autonomous Systems*, 59:998–1000, November 2011.

[86] S. Thrun. Learning occupancy grid maps with forward sensor models. *Autonomous Robots*, 15:111–127, 2003.

[87] H. M. Abdelghaffar, C. A. Woolsey, and H. A. Rakha. Comparison of three approaches to atmospheric source localization. In *Journal of Aerospace Information Systems*, volume 14, pages 40–52, 2017.

[88] S. J. Julier and J. K. Uhlmann. Unscented filtering and nonlinear estimation. *Proceeding of the IEEE*, 92(3), March 2004.

[89] A.H. Yousef, K. Iftekharuddin, and M. Karim. Towards aerosols lidar scattering plots clustering and analysis. *SPIE Defense, Security, and Sensing, International Society for Optics and Photonics*, 2013.

[90] Leeuw and G.J.K.a.G. Inversion of lidar signals with the slope method. *Applied Optics*, pages 3249–3256, 1993.

[91] M. I. Elbakary, K. M. Iftekharuddin, R. D. Young, and K. Afrifa. Aerosol detection methods in lidar-based atmospheric profiling. In *SPIE*, volume 9970, pages 1–11, 2016.

[92] M. I. Elbakary, H. M. Abdelghaffar, K. Afrifa, H. A. Rakha, M. Cetin, and K. M. Iftekharuddin. Aerosol detection using lidar-based atmospheric profiling. *SPIE Optics & Photonics*, 2017.

[93] S.P. Burton and et al. Aerosol classification using airborne high spectral resolution lidar measurements methodology and examples. *Atmos. Meas. Tech.*, pages 73–98, 2012.

[94] F. G. Fernald. Analysis of atmospheric lidar observations: some comments. *Applied Optics*, pages 652–653, 1984.

[95] M. J. Osborne and A. Rubinstein. *A Course in Game Theory*. Massachusetts Institute of Technology, 2011.

[96] H. M. Abdelghaffar, H. Yang, and H. A. Rakha. Isolated traffic signal control using a game theoretic framework. In *IEEE 19th International Conference on Intelligent Transportation Systems (ITSC)*, pages 1496–1501, Nov 2016.

[97] P. Holm, D. Tomich, J. Sloboden, and C. Lowrance. Traffic analysis toolbox: Guidelines for applying corsim microsimulation modeling software. Technical report, Office of Operations Federal Highway Administration, January 2007.

[98] H. M. Abdelghaffar, H. Yang, and H. A. Rakha. Isolated traffic signal control using nash bargaining optimization. *Global Journal of Researches in Engineering: B Automotive Engineering*, 16:27–36, 2016.

[99] E. Camponogara and W. Kraus. Distributed learning agents in urban traffic control. In *11th Portuguese Conference on Artificial Intelligence*, 2003.

[100] D. Oliveira and A. Bazzan. Reinforcement learning-based control of traffic lights in non-stationary environments. In *Fourth European Workshop on Multi-Agent Systems*, 2006.

[101] S. EI-Tantawy and B. Abdulhai. An agent-based learning towards decentralized and coordinated traffic signal control. In *Annual Conference on Intelligent Transportation Systems*, Madeira Island, Portugal, September 2010.

[102] S. El-Tantawy, B. Abdulhai, and H. Abdelgawad. Design of reinforcement learning parameters for seamless application of adaptive traffic signal control. *Intelligent Transportation Systems: Technology, Planning, and Operations*, 18:227–245, July 2014.

[103] H. M. Abdelghaffar, H. Yang, and H. A. Rakha. A novel game theoretic de-centralized traffic signal controller: Model development and testing. In 97*th Transportation Research Board Annual Meeting*, Washington DC, January 2018.

[104] J. Sangster and H. Rakha. Enhancing and calibrating the rakha- pasumarthy-adjerid car-following model using naturalistic driving data. *Transportation Science and Technology*, 3:229–248, 2014.

[105] M. Van Aerde and Hesham A. Rakha. Queensod rel. 2.10 - user's guide: Estimating origin - destination traffic demands from link flow counts. Technical report, March 2010.

[106] H. M. Abdelghaffar, H. Yang, and H. A. Rakha. Developing a de-centralized cycle-free nash bargaining arterial traffic signal controller. In 5^{th} *IEEE International Conference on Models and Technologies for Intelligent Transportation Systems*, pages 544 – 549, June 2017.

[107] J. Du, H. A. Rakha, A. Elbery, and M. Klenk. Microscopic simulation and calibration of a large-scale metropolitan network: Issues and proposed solutions. In *97th Annual Meeting of Transportation Research Board*, Washington DC, USA, January 2018.